

THESIS FOR THE DEGREE OF DOCTOR OF PHILOSOPHY

Molecular orientation in cellulose fibers and composites

Tensor spectroscopies and their analogues

Leo Svenningsson



Department of Chemistry and Chemical Engineering
CHALMERS UNIVERSITY OF TECHNOLOGY
Göteborg, Sweden 2020

Molecular orientation in cellulose fibers and composites
Tensor spectroscopies and their analogues
LEO SVENNINGSSON
ISBN: 978-91-7905-241-6

© LEO SVENNINGSSON, 2020.

Doktorsavhandlingar vid Chalmers tekniska högskola.

Ny serie nr 4708
ISSN: 0346-718X

Department of Chemistry and Chemical Engineering
Chalmers University of Technology
SE-412 96 Göteborg, Sweden
Telephone + 46 (0) 761189261

Thesis cover illustration by Isabell Sarstedt

Typeset by the author using L^AT_EX.

Printed by Chalmers Reproservice
Göteborg, Sweden 2020

Molecular orientation in cellulose fibers and composites

Tensor spectroscopies and their analogues

Leo Svenningsson

Department of Chemistry and Chemical Engineering
Chalmers University of Technology

Abstract

The scope of this thesis is to quantitatively investigate the molecular orientation distribution of regenerated cellulose fibers and composites. The molecular orientation is known to affect macroscopic properties such as tensile strength of the fiber. In addition, the quality of a carbon fiber is, to a great extent, determined by the molecular orientation of the precursor. A plethora of techniques are paramount for materials characterization and a handful of these are suited for determination of molecular orientation. Since different methods have various experimental limitations, methodological awareness is crucial in the strive for quantitative data and in particular when cellulose fibers and other polymers are chemically modified, or a part of a composite. This work concerns three methods in order to investigate molecular orientation: rotor synchronized magic angle spinning solid-state nuclear magnetic resonance spectroscopy (ROSMAS), polarized Raman spectroscopy, and X-ray scattering. The latter is already a proven method for analyzing molecular orientation and was therefore used as a reference for the two first methods, which have never previously been applied on cellulose fibers. ROSMAS was used to investigate the chemical shift anisotropy, which relates to molecular orientation, on a bundle of Lyocell fibers. Polarized Raman spectroscopy was used to analyze the molecular orientation distribution from the Raman vibrational tensor on a single fiber. A new method was developed for polarized Raman spectroscopy by assuming a wrapped Lorentzian orientation distribution function, as measured from X-ray scattering patterns. The results from both ROSMAS and polarized Raman spectroscopy were in agreement with X-ray scattering on a highly oriented cellulose fiber bundle and on a single regenerated cellulose fiber, respectively, indicating that these methods are quantitative. The ROSMAS and X-ray methodologies were applied to a stretched fiber consisting of a regenerated cellulose-lignin composite intended as a carbon fiber precursor. Finally, ROSMAS was also used for determination of the complete chemical shift anisotropy in the molecular reference frame on regio-regular poly(3-hexylthiophene) fibers, in addition to elucidation of backbone and side chain orientation.

In the grand perspective, resources have to be used efficiently to minimize environmental impact. Therefore, this work explores man-made environmentally benign cellulose alternatives to cotton and other polymers. These processes refine cellulose from plant life, typically trees, which can grow without pesticide on non-arable land.

Keywords: regenerated cellulose, fibers, composite, carbon fibers, lignin, molecular orientation, solid-state NMR, Raman spectroscopy, X-ray scattering.

Acknowledgments

Special thanks to my supervisor **Lars Nordstierna** for your guidance and mentorship. I will always remember this time. My co-supervisors Alex and Diana for teaching me how to operate solid-state NMR. There is so much to learn and I'm grateful having your support. To Tobias and Erik for an amazing NMR collaboration, I am truly grateful to have worked with you. To Anna, Yuan-Chi and Ezio for helping me with everything there is to know about Raman spectroscopy. I would have never been able to understand how to use this method if it were not for you. To Jenny, I hope we get to collaborate again. I think we only scratched the surface on our study. Jonna and Anna it has been truly insightful to work with you on our projects. To Massi, I think our collaboration produced something clever for our article. To my office mate, Chris, for taking the time to proofread my thesis. To Prof. Spiess and Prof. Veeman, who helped me to the remnants of the ROSMAS technique. To Elisabeth who encouraged me to study research, your trust has meant a lot to me. To all my friends and colleagues at Applied Chemistry, SIKT and everywhere else. I have had a great time with you over the years.

This work has been financed by "Södra Skogsägarna Foundation for Research, Development and Education", "Stiftelsen Nils och Dorthi Troëdssons forskningsfond", and Chalmers University of Technology.

Leo Svenningsson
Göteborg, January 2020

List of Publications

This thesis is based on the following appended papers:

- Paper 1.** Leo Svenningsson, Tobias Sparrman, Erik Bialik, Diana Bernin and Lars Nordstierna. *Molecular orientation distribution of regenerated cellulose fibers investigated with rotor synchronized solid state NMR spectroscopy*, Cellulose, 2019, 26, 4681-4692, 10.1007/s10570-019-02430-z.
- Paper 2.** Leo Svenningsson, Yuan-Chih Lin, Maths Karlsson, Anna Martinelli and Lars Nordstierna. *Molecular Orientation Distribution of Regenerated Cellulose Fibers Investigated with Polarized Raman Spectroscopy*, Macromolecules, 2019, 52, 3918-3924, 10.1021/acs.macromol.9b00520.
- Paper 3.** Tobias Sparrman, Leo Svenningsson, Karin Sahlin-Sjövold, Lars Nordstierna, Gunnar Westman and Diana Bernin. *A revised solid-state NMR method to assess the crystallinity of cellulose*, Cellulose, 2019, 26, 8993–9003, 10.1007/s10570-019-02718-0.
- Paper 4.** Leo Svenningsson, Jenny Bengtsson, Kerstin Jedvert, Werner Schlemmer, Hans Theliander and Lars Nordstierna. *Disassociated molecular orientation distributions of a composite cellulose-lignin carbon fiber precursor*, Submitted
- Paper 5.** Leo Svenningsson, Emmy Järsvall, Jonna Hynynen, Christian Müller and Lars Nordstierna. *NMR chemical shift anisotropy reveals backbone and side chain orientation in meltspun poly(3-hexylthiophene) fibers*, Manuscript

Author's Contributions

- I Main author. Method development, preliminary experiments, supporting experiments and all computations excluding DFT.
- II Main author. Method development, all computations and most of the experiments.
- III Co-author. Parallel experiments, supporting experiments (X-ray scattering crystallinity measurements).
- IV Main author. ROSMAS and WAXS experiments and analysis.
- V Main author. Computational development, ROSMAS and WAXS analysis.

Related Work

The following publication is not included in the thesis:

Massimiliano Mauri, Leo Svenningsson, Thomas Hjertberg, Lars Nordstierna, Oscar Prieto and Christian Müller. *Orange is the new white: rapid curing of an ethylene-glycidyl methacrylate copolymer with a Ti-bisphenolate type catalyst*, Polymer Chemistry, 2018, 9, 1710-1718, 10.1039/C7PY01840A.

List of Acronyms

ODF	–	Orientation Distribution Function
PAS	–	Principal Axis System
MF	–	Molecular Frame
DF	–	Director Frame
RF	–	Rotor Frame
wL	–	wrapped Lorentian
NMR	–	Nuclear Magnetic Resonance
FID	–	Free Induction Decay
CSA	–	Chemical Shielding/Shift Anisotropy
MAS	–	Magic Angle Spinning
ROSMAS	–	ROtor-Synchronized Magic Angle Spinning
WAXS	–	Wide Angle X-ray Scattering
PET	–	Poly(Ethylene Terephthalate)
PAN	–	PolyAcryloNitrile
MCC	–	Micro Crystalline Cellulose
CNC	–	Cellulose NanoCrystals
P3HT	–	Poly(3-HexylThiophene)

Sammanfattning

Alla träd och växter består till stor del av cellulosa. Detta gör att de är starka mot naturens krafter och träd kan växa högt utan att falla ner. Cellulosans fascinerande egenskaper har använts i tusentals år av människor, bland annat i formen av textilier, och idag är det viktigare än någonsin att ta vara på ett av naturen mest användbara material.

Denna avhandling avser att analysera cellulösans ordning i framtidens naturmaterial. Textilfibrer från träd och återvunna kläder står högt på listan. Det gör även kolfibrer, från den starka cellulosan och trädens eget bindemedel, ligninet. Det är just ordningen av molekylerna i material som bidrar med positiva egenskaper, såsom materialets styrka.

Den undersökningsteknik som påvisar hög potential för att undersöka naturens material utnyttjar den kärnmagnetiska resonansen, som är en inneboende egenskap hos atomer. Denna teknik används regelbundet för att undersöka molekylers struktur, små som stora. Här undersöks ordningen i cellulosan med hjälp av denna egenskap samt att resultaten jämförs med andra tekniker.

En direkt jämförelse mellan de tre huvudsakliga metoderna som används i denna avhandling har tidigare aldrig gjorts. Därtill har undersökningar av ordning i kompositer tidigare varit ett mycket svårt problem att lösa. Den kärnmagnetiska resonansen erbjuder ett unikt sätt att särskilja signaler från olika material, och således kan även kompositmaterial undersökas.

Foreword

Sometime we find ourselves in a state of mind where we just have to know. We do things, sometimes silly things, like jumping in a puddle to see the ripples. Waves with a known propagation speed. Its reflection on the boundaries, and the eventual interference of itself. Some time ago, curiosity seemed to have gotten the better of me. I had found an interest in magnetic resonance technology. From spin wave systems (spintronics),[1] magnetic resonance imaging,[2] and now materials analysis. Wielding one of the more peculiar phenomena in nature, one can investigate: molecular structure, diffusion[3], ligands[4] and pores.[5, 6] On the more outlandish side, measurements of dark matter have been proposed.[7, 8] And the electron magnetic moment remains one of the most accurate measurements known to man, with the g-factor at a staggering $g/2 = 1.00115965218085(76)$.[9]

All the while, I had luxury of studying a few other phenomena such as the Raman interaction and X-ray scattering. Exploring the physical connections, turning on the lights in the dark, is an invigorating challenge. And hopefully I have made some ripples.

This thesis is a memory of my journey as a doctoral student.

Contents

Abstract	iii
Acknowledgments	iv
List of Publications	v
Authors' contributions	vi
Related Work	vii
List of Acronyms	viii
Sammanfattning	ix
Foreword	x
1 Introduction	1
2 Cellulose	3
2.1 Cellulose, a Natural Polymer	3
2.2 Regenerated Cellulose Fibers	4
2.3 Cellulose-Lignin Carbon Fibers	5
3 Molecular Orientation Distributions in Polymers	7
3.1 Background	7
3.2 Measuring Molecular Orientation	10
3.3 ODF Reconstruction	10
3.4 Choice of Model Function	11
4 NMR Spectroscopy	13
4.1 Introduction to NMR Spectroscopy	13
4.1.1 Precession and Relaxation	13
4.1.2 The Chemical Shielding Effect	17
4.1.3 The Magnetic Dipolar Coupling	18
4.2 Solid State NMR Spectroscopy	19
4.2.1 Magic Angle Spinning	19
4.2.2 Heteronuclear Decoupling	19

4.2.3	Cross Polarization	20
5	Rotor Synchronized MAS	21
5.1	Overview of Rotor Synchronized MAS	21
5.2	Sample Preparation	24
5.3	Mathematical Description of ROSMAS	24
5.4	ROSMAS with Oriented Samples	26
5.5	Properties of the ROSMAS Spectrum	26
5.6	Derivation of the ROSMAS Experiment	28
6	Polarized Raman Spectroscopy	39
6.1	Overview of the Polarized Raman Spectroscopy Experiment	39
6.2	The Wrapped Lorentzian Polarized Raman Spectroscopy Experiment	45
7	X-Ray Scattering	47
8	Crystallinity of Celluloses	51
9	Results and Discussion	53
9.1	Molecular Orientation from ROSMAS and Raman Spectroscopy . . .	53
9.2	Crystallinity Filtered NMR Spectroscopy	60
9.3	Disassociated Molecular Orientation in Cellulose-Lignin Composites .	61
9.4	Backbone and Side Chain Orientation Poly(3-hexylthiophene) Fibers	65
10	Concluding Remarks	69
A	Computational Remarks	71
A.1	Computation of the ROSMAS Intensity and Order Parameters	71
A.2	Computation of the Polarized Raman Experiment	73
B	Derivation of Most Probable ODF	75
C	Links	77
	Bibliography	79

Chapter 1

Introduction

In a strive to develop new materials, we constantly look to what nature assembles to inspire us. Given enough scientific knowledge on these materials, one can make high end specialized materials such as nano-particles, carbon fibers, textiles, and more. This thesis aims to elucidate the molecular order/disorder in cellulose based materials and composites, with a unique twist of spectroscopic techniques, which also translates to any other polymers. A key aspect of cellulose fiber morphology is the molecular orientation distribution along the fiber axis. Molecular orientation is well known to affect macroscopic properties of the fiber and in extension, a textile. Intricacies of measuring molecular orientation arise when the fiber is chemically modified or a part of a composite. Therefore, several methods has to be available in order to avoid pitfalls from experimental limitations. A handful of methods exist to measure molecular anisotropy, namely: (i) rotor synchronized magic angle spinning magnetic resonance spectroscopy (ROSMAS), (ii) polarized Raman spectroscopy, (iii) X-ray scattering, (iv) DECODER NMR, (v) neutron diffraction, (vi) infrared dichroism, (vii) birefringence, and a few other methods. This work concerns methods (i)-(iii), which encompass several features of high value for materials analysis. X-ray scattering is already a commonly used method for analyzing molecular orientation in cellulose fibers and other polymers. The ROSMAS technique was first developed by Harbison and Spiess in 1985, but has rarely been used for routine work. The great chemical selectivity of ROSMAS allows for analysis of composites. The original and sequential authors seemed to have overlooked this, perhaps most important, property of the ROSMAS technique. ROSMAS is also differentiated, by separating chemical information in high dimensional spectra compared to the dimensionally locked Raman spectroscopy and X-Ray scattering. The quantitative aspects of molecular orientation have never previously been explored in such way that (i)-(iii) can be directly compared to each other. [10–18]

Paper I establishes the ROSMAS technique as a method to investigate molecular orientation i cellulose. The method requires accurate knowledge of the chemical shift anisotropy (CSA) in the molecular frame, which was determined by density functional methods. The ROSMAS NMR technique has great potential in resolving molecular anisotropy in composite materials, due to its excellent chemical selectivity. In comparison, X-ray techniques often suffer from similar close range inter molecular

distances in many polymeric materials. These can in many cases produce overlapping scattering patterns for polymers.

Paper II describes a new method using polarized Raman spectroscopy with quantitative properties that relates to both ROSMAS and X-ray scattering. When several investigative techniques are available we can ultimately make stronger claims on the material properties.

In **Paper III** we describe a new way of measuring cellulose crystallinity through T_1 filtering. Crystallinity is a hotly debated topic in the cellulose community and is therefore useful to study. But the goal of this project, from a molecular orientation perspective, is to incorporate T_1 filtering directly in the ROSMAS pulse sequence to ease analysis of semi crystalline materials.

In **Paper IV** we investigate a cellulose-lignin composite carbon fiber precursor in order to separate the molecularly ordered cellulose from the disordered lignin. The observed molecular orientation is put in context from the molecular orientation observed in native wood using ROSMAS. The molecular orientation in the precursor strongly influence the quality of the carbon fiber.

In **Paper V** we investigate the experimentally gained chemical shift anisotropy in the molecular frame of a Poly(3-HexylThiophene) (P3HT) fiber. Molecular orientation in the backbone and the side chains can be analyzed independently using ROSMAS NMR spectroscopy. A doped P3HT has anisotropic electrical conductivity, directly related to the molecular orientation. The material is hence relevant in the field of conducting textiles and solar cells.

The following chapters include essential theoretical framework for the given methods and a synopsis of the appended papers.

Chapter 2

Cellulose

2.1 Cellulose, a Natural Polymer

All trees and plants contain the polysaccharide known as cellulose as a part of their cell wall. The natural polymer can therefore be regarded as a potential renewable resource for the foreseeable future. Cellulose chains typically aggregate to form semi-crystalline structures from the unit chain shown in Figure 2.1. Native cellulose contains the crystalline form “cellulose I”, which is rather a combination of two crystalline forms, I_α and I_β . Plants and bacteria produce different fractions of the two crystalline forms with the bacteria producing higher relative amounts of I_α and plants producing mainly I_β . Cellulose can have additional stable allomorphs. One such crystalline structure is “cellulose II”, the most thermodynamically stable allomorph, which is formed from regeneration or mercerization of cellulose. In contrast to the parallel chain organization of cellulose I, cellulose II chains are organized in an anti-parallel fashion. Cellulose III are made by treatment of liquid ammonia, whereas cellulose IV is formed from heat treatment of cellulose III. These two latter crystalline structures are less relevant for this work and will not be explored further.[19–22]

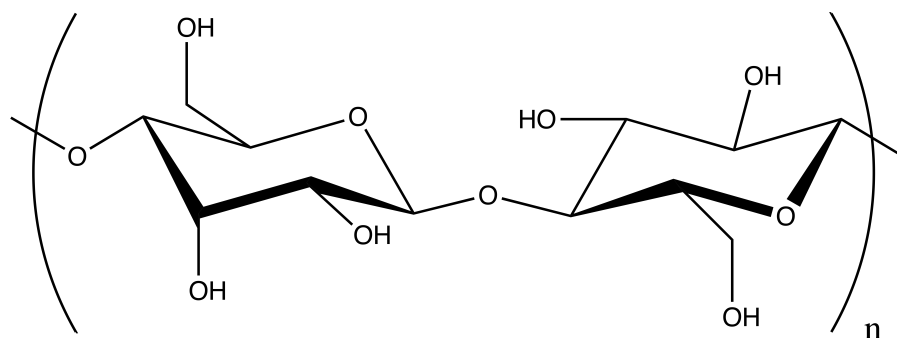


Figure 2.1: The cellulose repeating unit.

This work has been focused on materials with the cellulose II crystalline structure. X-ray structures have previously been reported for mercerized and regenerated cellulose, with no significant differences between these two systems.[23, 24] Figure 2.2 displays a cellulose II cluster as calculated from DFT techniques using the heavy atom coordinates from Langan et al. as starting positions.[18, 24] The hydrogen atoms, not present in X-ray structures, are added according to two bonding patterns.[25]

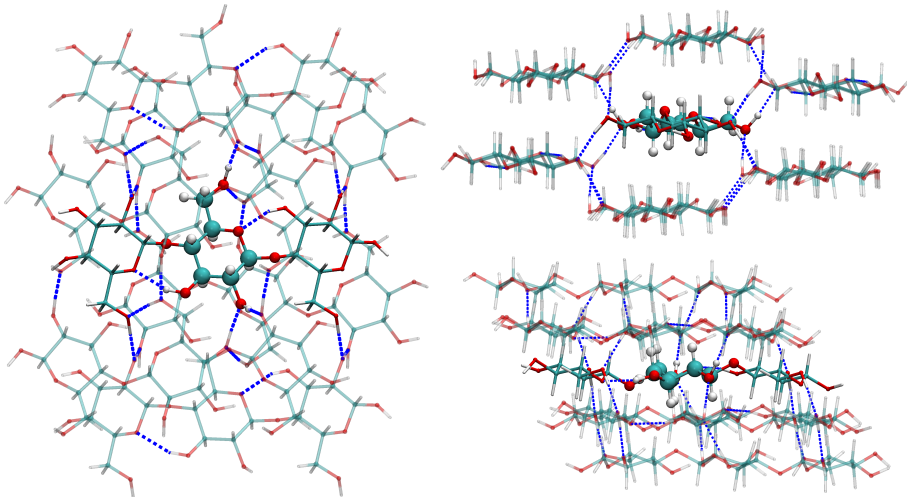


Figure 2.2: Cluster for shielding tensor calculation for the origin chain with H-bond pattern B.[18, 25] The color scheme is determined by carbons (turquoise), oxygen (red) and hydrogen (white) with the dotted pattern as hydrogen bonds.

2.2 Regenerated Cellulose Fibers

Regenerated cellulose fibers have a history stretching back to the 1850s but did not see textile commercialization until 1889. It was then a man with the full name Louis-Marie Hilaire Bernigaud de Grange, Comte de Chardonnet presented a regenerated cellulose textile as synthesized silk at the Exposition Universelle of 1889. Since then several processes have emerged to produce regenerated textile fibers from plants, with the popular methods being Viscose, Lyocell and the more recently developed ionic liquid dissolution methods. The viscose process starts by submerging pulp in aqueous sodium hydroxide solution that converts cellulose into alkali cellulose. The alkali cellulose is then oxidized under precise conditions for partial depolymerization. The resulting mass is reacted with carbon disulfide that forms sodium cellulose xanthate. The cellulose xanthate can now be dissolved in sodium hydroxide solution. The resulting solution is extruded in a coagulation bath of water, zinc sulfate, sodium sulfate and sulfuric acid to form the regenerated cellulose fibers. So far, the viscose process has not received any awards for being an environmentally friendly process. On the other hand, the Lyocell and ionic liquid processes have a brighter prospect. Lyocell was first commercially introduced in 1984 and is now pioneered by the company Lenzing earning them the European Eco-Label for their Lyocell fiber called Tencel.[26] Lenzing has previously made claims that their fiber has higher yield per acre and that Tencel requires less water compared to cotton. Lyocell is produced by

dissolving wood pulp in hot N-methyl morpholine oxide. The solution is extracted through a spinneret coagulating the fiber in a dilute amine oxide bath. The process is designed to recover over 99% of the chemicals used to dissolve the cellulose. According to global markets insight, the Lyocell market was worth around 891 million USD in 2017 and is expected to grow to 1.5 billion USD in 2024.[27]

Ionic liquid dissolved cellulose fibers are conceptually very similar to Lyocell in the context of possible use of a direct solvent, in contrast to the chemical modification needed for Viscose. Although many different ionic liquids could be used to make fibers, there is no commercial large scale production as of 2018. One well studied ionic liquid spun fiber is the Ioncell fiber[28], which is dissolved in 1,5-diazabicyclo[4.3.0]non-5-enium acetate.

In the context of this thesis, molecular orientation distributions in regenerated cellulose fibers are often qualitatively evaluated from birefringence measurements or X-ray scattering patterns. A few works concern quantitative measurements, though that statement should be met with criticism.[29]. Krassig and Lafrance et al. both show the importance of accurate X-ray evaluation of oriented polymers, though without providing a method the correct evaluation.[16, 19]. A publication on fiber deformation and orientation of ionic liquid spun fibers was published in 2016 by Wanasekara and Sixta[30], which uses a Lorentzian curve fitting on wide angle X-ray scattering (WAXS) and polarized Raman spectroscopy by determining a ratio of parallel and anti-parallel polarization, a method useful for studying trends. [19–21, 28, 30–34]

2.3 Cellulose-Lignin Carbon Fibers

The carbon fiber is a light weight material used in aerospace, construction, medical, sports equipment and automotive industry.[35, 36] The carbon fibers have a characteristic high tensile strengths potentially up to 7 GPa. Carbon fibers are produced by carbonizing a polymeric fiber in an inert atmosphere at temperature well over 1000 °C. The exact processes used is dependent on the choice of carbon fiber precursor and final product quality.

The most common carbon fiber precursor is the polyacrylonitrile (PAN) fiber.[37] Recent technologies, however, are developed to produce high yield carbon fibers from natural products, such as, regenerated cellulose and lignin composites.[35, 38–41] These regenerated cellulose-lignin carbon fiber precursors have been shown through life cycle assessment to be an environmentally benign precursor alternative than PAN fibers.[42] In order to efficiently produce a carbon fiber, two important qualities are necessary: 1) high carbon content in the precursor and 2) existence of molecular orientation in the carbon fiber precursor. The introduction of lignin in a cellulose fiber increases the carbon content due to the abundance of aromatic structures in lignin. Existence and quantification of molecular orientation in these composite fibers have so far been challenging to determine.

Chapter 3

Molecular Orientation Distributions in Polymers

3.1 Background

In order to express molecular orientation, it is necessary to lay the foundation of how molecular orientation is defined in different reference frames that later will relate to experiments. A chain-segment is defined in the arbitrarily chosen molecular frame (MF) that represents the direction of a molecule in a chain, with the axis $\{\mathbf{X}_M, \mathbf{Y}_M, \mathbf{Z}_M, \}$. [10] The fiber is defined in the director frame (DF) with the axis $\{\mathbf{X}_D, \mathbf{Y}_D, \mathbf{Z}_D, \}$ with \mathbf{Z}_D as the drawing direction of the fiber. One possible way to relate one frame to another is through Euler angles (ϕ, θ, ψ) . Another popular method for coordinate transformation, with proven computational benefits, is using quaternions. Quaternions will not be introduced here, though they might improve some aspects tensor rotation in NMR modelling. [43, 44] Figure 3.1 shows a molecule that is rotated away from the fiber axis using three Euler rotations. An orientation distribution function (ODF), in the context of polymeric fibers, is a uni-axially symmetric collection of polymer chain-segments, where each individual repeating molecular unit is treated as a rod. The angle ϕ in Figure 3.1 describes distribution around the fiber symmetry axis, which is assumed to be uni-axially symmetric. Also ψ is uniformly distributed but around its own symmetry axis \mathbf{Z}_M , which in the case of cellulose, simultaneously covers the twofold helical structure of cellulose.

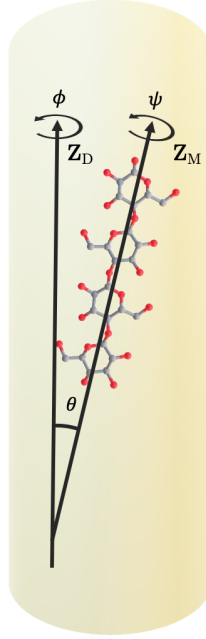


Figure 3.1: Euler angle representation between the director frame and molecular frame.

Without any physical assumptions, it is possible to state a three dimensional orientation distribution function ODF that is positive and normalized for every orientation segment. Since the number of chains segments is usually large for any macroscopic sample, a continuous model can be comfortably applied.

$$\int_0^{2\pi} \int_0^\pi \int_0^{2\pi} f(\phi, \theta, \psi) \sin \theta \, d\phi \, d\theta \, d\psi = 1 \quad (3.1)$$

The function $f(\phi, \theta, \psi)$ is typically not known but can be approximated by series expansion. Although any series expansion with fast converging properties can be used for ODF approximations, most are based on spherical harmonics. For the case where the ODF is symmetric on both ϕ and ψ , as in a fiber, the spherical harmonics expansion is simplified to a Legendre polynomial expansion. Each contribution of the series expansion is weighted by an order parameter P_ℓ . For a strict one dimensional system the Legendre polynomials are defined as:

$$f(\theta) = \sum_{\ell=0}^{\infty} \frac{2\ell+1}{2} \cdot \langle P_\ell \rangle \cdot P_\ell(\cos \theta) \quad (3.2)$$

For a 3 dimensional rotation, as in Equation (3.1) and real world molecular orientation distributions, the Legendre polynomials with 3 dimensional normalization becomes:

$$f(\theta) = \sum_{\ell=0}^{\infty} \frac{2\ell+1}{8\pi^2} \cdot \langle P_\ell \rangle \cdot P_\ell(\cos \theta) \quad (3.3)$$

The Legendre polynomials is most efficiently described by its differential form:

$$P_\ell(\cos \theta) = \frac{1}{2^\ell \ell!} \frac{d^\ell}{d \cos^\ell \theta} (\cos^2 \theta - 1)^\ell \quad (3.4)$$

The order parameter is also described by its Legendre transform, analogous to Fourier transform coefficients:

$$\langle P_\ell \rangle = \int_0^\pi P_\ell(\cos \theta) f(\theta) \sin \theta d\theta \quad (3.5)$$

The ODF in a fiber is only dependent on one angle θ , describing the orientation of a chain-segment in the fiber drawing direction. A wrapped Lorentzian ODF (wL), also known as wrapped Cauchy ODF, is demonstrated in Figure 3.2 with a scale factor of $\lambda = 0.3$. By applying Equation (3.5) to the function in Figure 3.2, the order parameters in Table 3.1 are obtained. The odd terms vanish because they are anti-symmetric functions integrated over the periodic interval $0 - \pi$. In Table 3.1, there exists a trend of decreasing P_ℓ for the wL function.

Table 3.1: Order parameters calculated from the wrapped Lorentzian in Figure 3.2 with a scale factor of $\lambda = 0.3$.

$\langle P_2 \rangle$	$\langle P_4 \rangle$	$\langle P_6 \rangle$	$\langle P_8 \rangle$
0.4488	0.2641	0.1678	0.1107

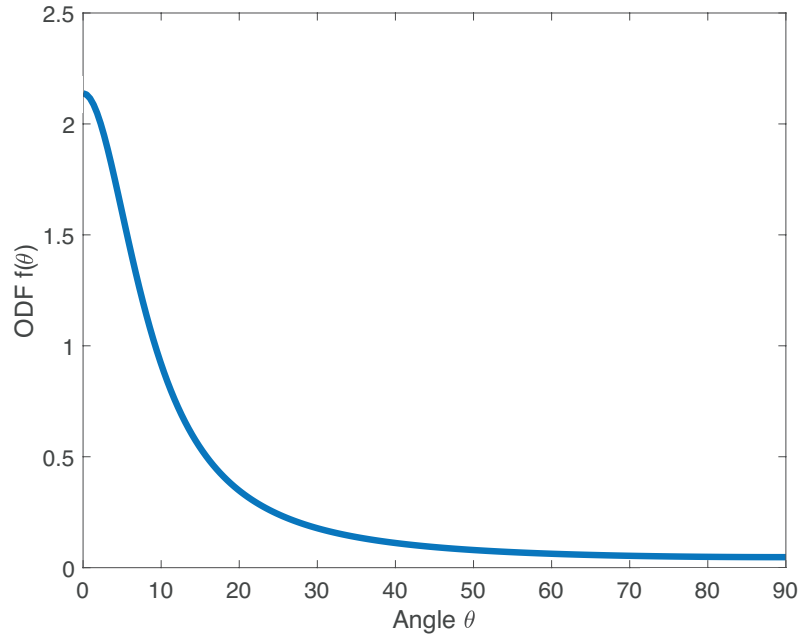


Figure 3.2: Wrapped Lorentzian ODF with a scale factor of $\lambda = 0.3$ dependent on the Euler angle θ between the director frame and the molecular frame.

3.2 Measuring Molecular Orientation

A handful of techniques have been developed that can measure anisotropy in fibers, which includes: rotor synchronized magic angle spinning (ROSMAS) [10, 45–54], DECODER[13, 55, 56] NMR spectroscopy, polarized Raman spectroscopy[11, 57–64], infrared dichroism[12], birefringence[14], X-ray[12, 16, 29, 65] and neutron scattering[15], each having certain limitations. For example, X-ray scattering can measure the complete ODF of a single fiber or bundle. Polarized Raman spectroscopy can measure on a single fiber with some possibility to distinguish between amorphous and crystalline signal contributions. NMR spectroscopy can only measure on fiber bundles, which introduces bundle orientation on top of the molecular fiber orientation. The limitations on the number of order parameters that can be investigated with each method can be seen in Table 3.2.

Table 3.2: Some previously existing methods for characterizing orientation

Method	ODF approximation
Birefringence	$\langle P_2 \rangle$
Infrared dichroism	$\langle P_2 \rangle$
Polarized Raman spectroscopy	$\langle P_2 \rangle, \langle P_4 \rangle$
Rotor synchronized NMR spectroscopy	$\langle P_2 \rangle, \langle P_4 \rangle, \langle P_6 \rangle, \langle P_8 \rangle \dots$
DECODER NMR spectroscopy	$f(\theta)$
X-ray scattering	$f(\theta)$
Neutron diffraction	$f(\theta)$

3.3 ODF Reconstruction

The order parameters give only a hint on how the molecules are oriented with special exception of $\langle P_2 \rangle = 1$ for a perfectly oriented sample. One should be careful with orientation assumptions based only on the order parameters since they alone say little about the shape of the ODF they represent. The ODF can be calculated by nonlinear fitting of Equation (3.6), shown in Figure 3.3 with three different model functions with the same order parameters $\langle P_2 \rangle$ and $\langle P_4 \rangle$.

$$\sum \left(\langle P_\ell \rangle - \int_0^\pi P_\ell(\cos \theta) f_{\text{model}}(\theta) \sin \theta \, d\theta \right)^2 = 0 \quad (3.6)$$

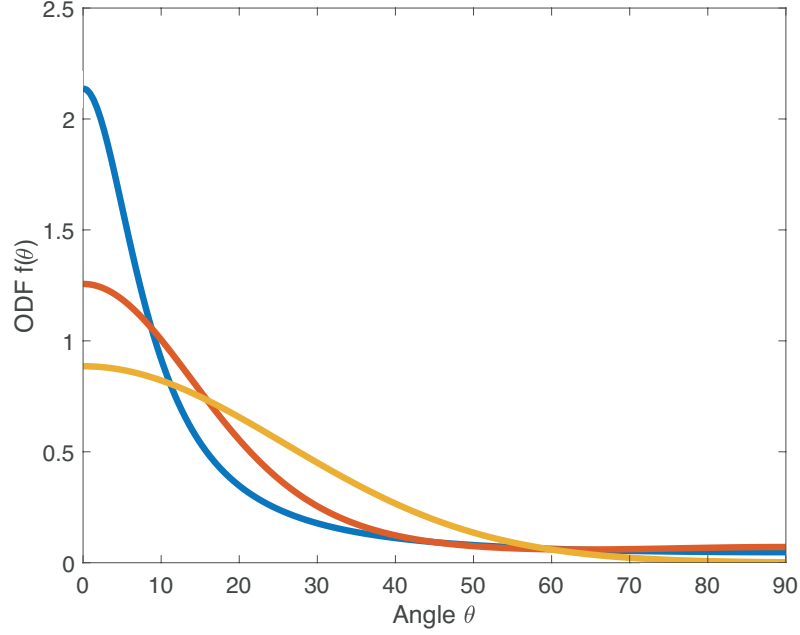


Figure 3.3: Reconstruction of the ODF with order parameters $\langle P_2 \rangle = 0.4488$ and $\langle P_4 \rangle = 0.2641$ using wrapped Lorentzian function (blue), most probable function (red) and Gaussian function (yellow)

From Figure 3.3 it is apparent that the choice of model function is critical to visualize an orientation distribution close to the physical ODF as distributions varies wildly. Although many different models are reported, this work uses information from WAXS patterns to find a likely ODF fit. In Chapter 7 will reveal that a wL ODF is a good choice for molecular orientation of a single drawn regenerated cellulose fiber.

3.4 Choice of Model Function

The wrapped Lorentzian[43] is similar to a traditional Lorentzian probability density function with added periodic condition. In the special case of a fiber, π periodicity is implied. Equation (3.7) shows the normalized wL function centered at 0° with a scale factor λ . It is usually more common to use γ to represent the scaling factor, but it is easily confused with the Euler angle γ used in the ROSMAS related works. Therefore, λ is used in this thesis, while γ is used in **Paper I, II and IV**.

$$f_{\text{wL}}(\theta) = \frac{1}{\pi} \cdot \frac{\sinh \lambda}{\cosh \lambda - \cos 2\theta} \quad (3.7)$$

The most probable ODF was introduced by Bower[11, 58] to be applied with his polarized Raman experiment. The function is derived from a statistical mechanics approach, where the information entropy S is maximized with respect to the ODF. For a molecular distribution discussed in Chapter 3, S is defined as:

$$S = -k \int_0^\pi f(\theta) \ln(f(\theta)) \sin \theta \, d\theta \quad (3.8)$$

By assuming $f(\theta)$ is smooth, the function is maximized using Lagrangian multipliers with the constraint of Equation (3.5). The most probable (mp) ODF is then:

$$f(\theta)_{\text{mp}} = \frac{\exp\left(\sum_{\ell} \lambda_{\ell} P_{\ell}(\cos \theta)\right)}{\int_0^\pi \exp\left(\sum_{\ell} \lambda_{\ell} P_{\ell}(\cos \theta)\right) \sin \theta \, d\theta} \quad (3.9)$$

A derivation of the most probable ODF is found in *Appendix A*.

The Gaussian distribution is commonly used to describe molecular orientation in fibers but lacks evidence to support its use. It is also a non-periodic function, which is in contradiction to the fiber symmetry. For completeness, it is included here:

$$f_{\text{Gauss}}(\theta) = \sqrt{m/\pi} \cdot e^{-m \cdot (\theta - \phi)^2} \quad (3.10)$$

with the scaling factor m .

The mathematical description of a true periodic Gaussian function is rather inconvenient from a computational standpoint.[43] Harbison et al. have cleverly employed a sine based Gaussian function, which also solves the periodic requirement:

$$f_{\text{Gauss}}(\theta) = C \cdot e^{-m \cdot (\sin \theta)^2} \quad (3.11)$$

with the normalization constant C . [10]

Chapter 4

NMR Spectroscopy

4.1 Introduction to NMR Spectroscopy

Magnetic resonance is the underlying phenomenon that led a paradigm shift in scientific analysis. Nuclear magnetic resonance (NMR) spectroscopy can, among other things, with extraordinary detail resolve large molecular structures such as proteins[66] using multidimensional correlation spectroscopy, investigate dynamics and stereo chemistry. For the general public, magnetic resonance imaging (MRI)[2] is more commonly known to help medical doctors diagnose patients with highly detailed soft tissue images of the body. The word "nuclear" is omitted in medical situations to make patients know that it is completely safe and noninvasive.

The purpose of this chapter is to give a general perception on the fundamentals of magnetic resonance. Magnetic resonance is in its heart a quantum mechanical phenomenon. However, for some cases a classical analogy exist, typically for a isolated spin 1/2 system. In other cases it is preferable to describe spin systems with its Hamiltonian operator. In this work, the classical interpretation will be presented when applicable due to its more accessible nature.

4.1.1 Precession and Relaxation

For simplicity and clarity, this section only considers nuclear spin 1/2 systems where the vector model may apply. In the case of an uncoupled spin, each spin is treated as a "bar magnet" and then the sum of all magnetic moments μ will be:

$$\mathbf{M} = \sum \mu \tag{4.1}$$

For a non-magnetic material in a zero magnetic field environment, the net magnetization \mathbf{M} will effectively be $\bar{0}$. But when a magnetic field is applied, some of the magnetic moments will align with and against the magnetic field.

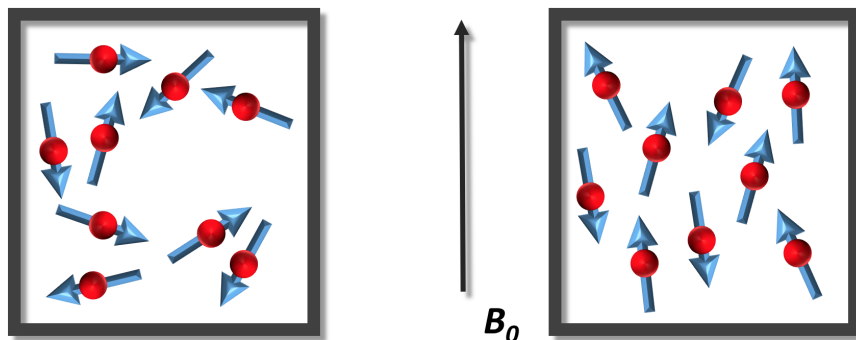


Figure 4.1: Two spin systems without external magnetic field (left) and with external magnetic field (right)

The magnetic moments are Boltzmann distributed, relating to their quantum mechanical spin up and down states. In a magnetic field, each magnetic moment experience precession at the rate of:

$$\frac{\nu_l}{2\pi} = -\gamma B_0 \quad (4.2)$$

where ν_l is the Larmor frequency, γ the gyromagnetic ratio and B_0 the applied magnetic field. The precession of the magnetic moment is shown in Figure 4.2.

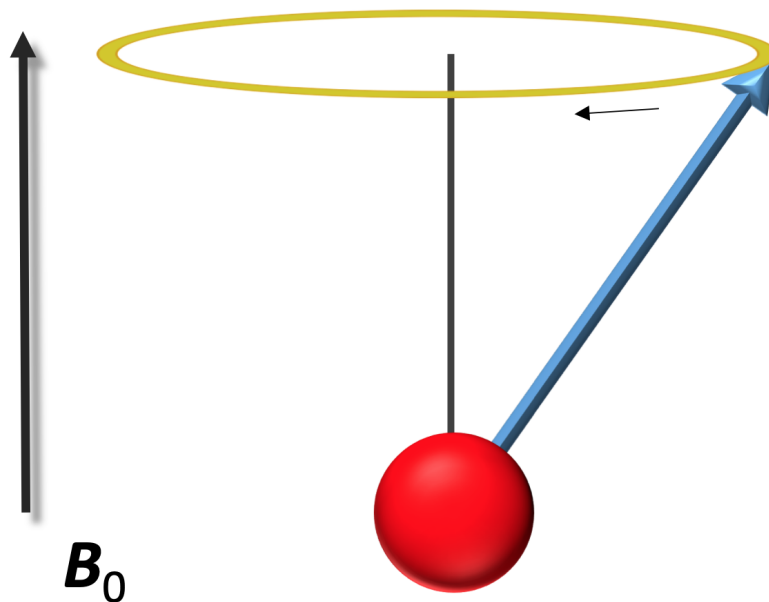


Figure 4.2: A magnetic moment undergoing precession in a magnetic field.

At equilibrium there is no net magnetization in the horizontal plane and all magnetization is in the external magnetic field B_0 direction, which is chosen as the **z**-axis.

$$\mathbf{M} = \begin{pmatrix} 0 \\ 0 \\ M_0 \end{pmatrix} \quad (4.3)$$

By applying a short on-resonance electromagnetic pulse, it is possible to twist the magnetization vector \mathbf{M} around an axis orthogonal to the B_0 field. Typically a pulse of the length that corresponds to twisting \mathbf{M} by 90° is used as in Figure 4.3.

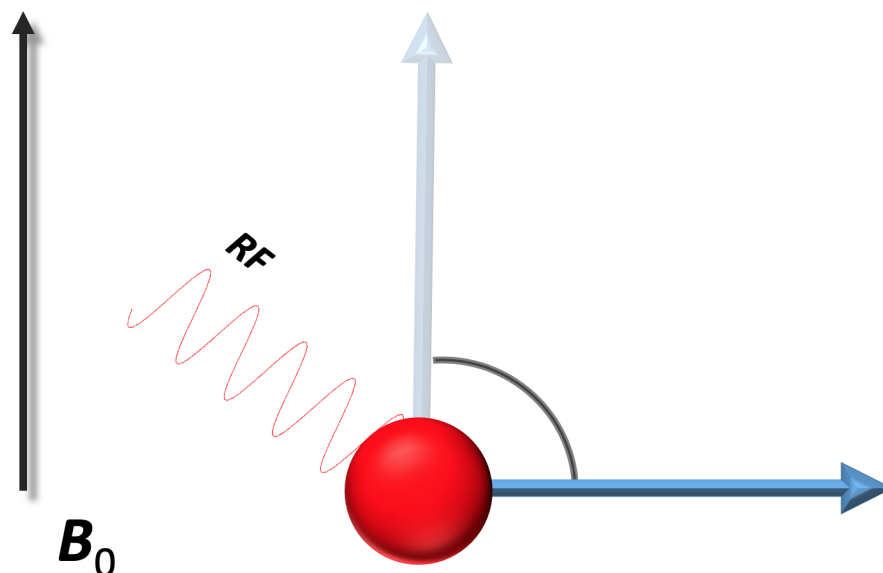


Figure 4.3: A magnetic moment undergoing precession in a magnetic field after a 90° pulse has been applied.

When the magnetization precess, it induces an oscillating magnetic field in a coil, which is the source for our magnetic resonance signal. The signal will inevitably experience decay due to magnetic moment aligning itself with the external magnetic field with the rate $\exp(-t/T_1)$ where T_1 is the longitudinal relaxation time. Initially, all of the magnetic moments precess together in coherence. However, the magnetic vector \mathbf{M} experiences a loss of $M_{x,y}$ magnetization due to each spin slowly rotating out of phase, losing coherence. Transverse relaxation occurs at the rate $\exp(-t/T_2)$ with T_2 as the relaxation time constant. The relaxation time T_2 is often much shorter, compared to T_1 relaxation time, and is therefore often the dominating factor for signal decay. The signal measured from NMR is logically called the free induction decay or FID. The vector representation is purely phenomenological and is typically described by the Bloch equations. The Bloch equations are given by:

$$\frac{dM_x(t)}{dt} = \gamma (\mathbf{M}(t) \times \mathbf{B}_0)_x - \frac{M_x(t)}{T_2} \quad (4.4)$$

$$\frac{dM_y(t)}{dt} = \gamma (\mathbf{M}(t) \times \mathbf{B}_0)_y - \frac{M_y(t)}{T_2} \quad (4.5)$$

$$\frac{dM_z(t)}{dt} = \gamma (\mathbf{M}(t) \times \mathbf{B}_0)_z - \frac{M_z(t) - M_0}{T_1} \quad (4.6)$$

A more fundamental approach would use quantum mechanics to describe both simple precession and the origin of relaxation. However, this is outside the scope of this thesis and it is encouraged to read introduction books by Keeler, Duer and Levitt[67–69] for a more detailed view on the topic.

It should be known that a single magnetic resonance can be described by the Zeeman Hamiltonian, an interaction of the atomic spin \mathbf{I} and the external field \mathbf{B}_0 . For a typical NMR setup the Zeeman Hamiltonian is described as:

$$H_z = -\gamma\hbar\mathbf{I}\mathbf{B}_0 \quad (4.7)$$

and the eigenstate energy levels E are then:

$$E = -\gamma\hbar B_0 \langle I, m | \mathbf{I}_z | I, m \rangle = -\gamma\hbar B_0 m \quad (4.8)$$

which for spin 1/2 gives the energy levels:

$$E = \pm\gamma\hbar B_0/2 \quad (4.9)$$

Then the transition energy becomes:

$$\Delta E = \pm\gamma\hbar B_0 \quad (4.10)$$

The energy is converted to angular frequency ω as:

$$\omega = \gamma B_0 \quad (4.11)$$

The energy is then suspiciously identical to the Larmor frequency, but is actually the energy needed for a spin flip. From an experimental stand point, an orthogonal magnetic field near the Larmor frequency needs to be applied in order to interact with the nuclear spin.

4.1.2 The Chemical Shielding Effect

The chemical shielding effect is determined by the influence of electrons, locally changing the magnetic field felt by the nucleus. Electrons surrounding the nucleus affect the magnetic field felt by the nucleus in mainly two ways. **(1)** The diamagnetic effect caused by electrons moving around the nucleus while under influence of the external magnetic field. These electrons produce a magnetic field counteracting the external magnetic field similar to a coil. **(2)** The paramagnetic effect perturbs electrons on the outer shells, aligning the electrons' spin in the direction of the magnetic field. This further increases the local magnetic field experienced by the nucleus. The molecular bonds influence strongly on how the electrons behave for these two interactions creating a spatial dependence on the magnetic shielding, called chemical shielding/shift anisotropy. The chemical shielding is averaged in liquids by molecular tumbling compared to solids where magic angle spinning of the sample is performed to remove this effect, see Section 4.2.1. The chemical shielding interaction is represented by a second rank tensor $\bar{\sigma}$ which, when multiplied by the external magnetic field \mathbf{B}_0 , gives the local magnetic field.

$$\mathbf{B}_{\text{loc}} = \bar{\sigma} \cdot \mathbf{B}_0 \quad (4.12)$$

with the chemical shielding:

$$\bar{\sigma} = \begin{pmatrix} \sigma_{11} & \sigma_{12} & \sigma_{13} \\ \sigma_{21} & \sigma_{22} & \sigma_{23} \\ \sigma_{31} & \sigma_{32} & \sigma_{33} \end{pmatrix} \quad (4.13)$$

The chemical shielding interaction can be well approximated by the first order perturbation to the Zeeman Hamiltonian,

$$H = H_z + H_{\text{cs}} \quad (4.14)$$

when the chemical shielding interaction is:

$$H_{\text{cs}} = \gamma \hbar \mathbf{I} \bar{\sigma} \mathbf{B}_0 \quad (4.15)$$

The experimental manifestation of chemical shielding is typically appreciated in powders. Randomly oriented contributions give us a spectrum with features similar to Figure 4.4 with the eigenvalues marking the key features of the NMR powder pattern. NMR spectra are typically referenced against some substance and the referenced shielding tensor is called the chemical shift tensor δ , which is given by:

$$\delta_{\alpha\beta} = \frac{\sigma^{\text{ref}} - \sigma_{\alpha\beta}}{1 - \sigma_{\alpha\beta}} \quad (4.16)$$

With $\alpha\beta$ as the tensor indices.

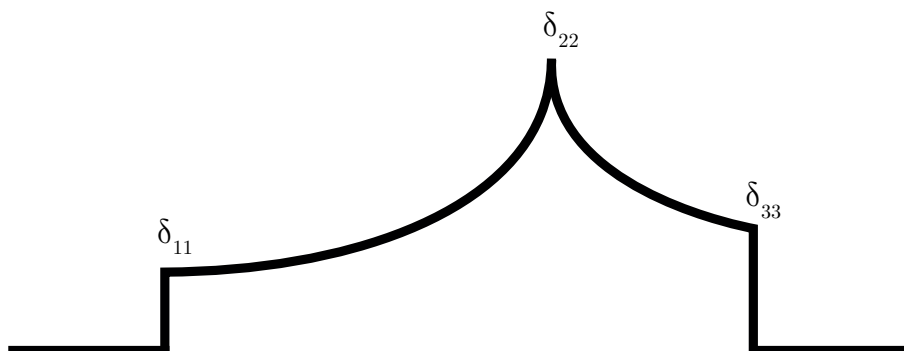


Figure 4.4: A schematic of a typical NMR powder pattern. The principal axis system chemical shift values, the chemical shift tensor eigenvalues, marked by key features of the powder pattern.

4.1.3 The Magnetic Dipolar Coupling

A magnetic dipolar coupling occurs when there are two magnetic sources in proximity, such as two nuclei in a molecule. The dipole coupling can have considerable effects on line broadening and relaxation in NMR spectroscopy. For solids, it is possible to remove a part of the dipolar coupling, again by magic angle spinning Section 4.2.1. Decoupling pulse sequences is often used to improve the line width, and in the case of a heteronuclear dipolar coupling, heteronuclear decoupling can be used as in Section 4.2.2. The first order perturbation of the dipole Hamiltonian is similar to a classical dipole, but with the magnetic moments exchanged for spin operators.

$$H_d = -\frac{\mu_0}{4\pi} \gamma_I \gamma_S \hbar \left(\frac{\mathbf{I} \cdot \mathbf{S}}{r^3} - 3 \frac{(\mathbf{I} \cdot \mathbf{r})(\mathbf{S} \cdot \mathbf{r})}{r^5} \right) \quad (4.17)$$

Where \mathbf{I} and \mathbf{S} are the respective spin operators of the two nuclei and \mathbf{r} as the distance vector between the two magnetic sources.

$$\mu_I = \gamma_I \hbar \mathbf{I} \quad (4.18)$$

$$\mu_S = \gamma_S \hbar \mathbf{S} \quad (4.19)$$

Equation (4.17) can be expanded and the terms that govern relaxation and line broadening can be separated. The line broadening term is shown in Equation (4.20) with polar coordinates, which has important implications for magic angle spinning:

$$H_d^{\text{lb}} = -\frac{\mu_0 \gamma_I \gamma_S \hbar}{4\pi r^3} (3 \cos^2 \theta - 1) \mathbf{I}_z \mathbf{S}_z \quad (4.20)$$

where θ is the angle between the applied magnetic field and the interaction tensor principal axis system (PAS).

4.2 Solid State NMR Spectroscopy

4.2.1 Magic Angle Spinning

In solids both the chemical shielding anisotropy and the dipole coupling contribute to line broadening that is typically averaged out by fast molecular tumbling in liquids. However, both the dipole coupling and chemical shielding effect contain terms in the form $(3 \cos^2 \theta - 1)$. While undergoing fast spinning the term is averaged to $\langle 3 \cos^2 \theta - 1 \rangle = (3 \cos^2 \theta_R - 1)(3 \cos^2 \beta - 1)$ with β as the angle between the spinning axis and the interaction tensor, while θ_R is the angle between the spinning axis and the magnetic field. With the angle $\theta_R = 54.74^\circ$, cleverly named Magic Angle Spinning (MAS), the anisotropic term averages to zero. The dipolar line broadening will narrow as rotation frequency increases, but typically it is difficult to spin at the speeds required for complete averaging. The chemical shielding anisotropy will however split a characteristic powder pattern into many smaller peaks spaced by the rotational frequency ω_R . When the rotational frequency exceeds about 4 times the anisotropy, then the spectrum can be considered to be averaged out.

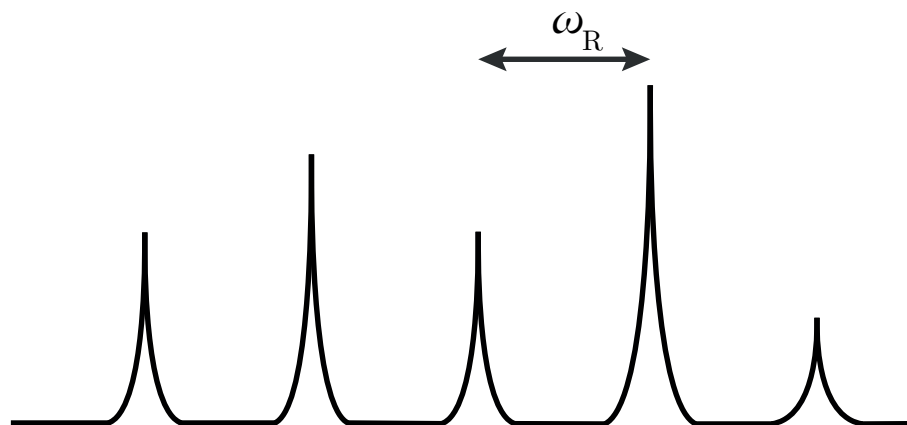


Figure 4.5: Representation of a solid state NMR powder pattern that undergoes Magic Angle Spinning at the speed ω_R .

4.2.2 Heteronuclear Decoupling

Section 4.1.3 previously mentioned that forcing sample rotation can reduce the dipolar effects by fast rotation. However, fast rotation is not enough for complete averaging of the dipolar effect. In the case of heteronuclear dipolar couplings, coupled nuclei are separately irradiated from the observed nuclei at the coupled nucleus's resonance frequency, causing repeated spin flips. These spin flips changes from $\pm 1/2$ for which the observed nuclei only see the time average. If the decoupling frequency greatly surpasses the dipole coupling strength, of about 30 kHz for a typical C-H pair, then the felt dipolar effect is essentially zero for the observed nuclei. High power decoupling is typically applied during the free induction decay signal detection, to improve the signal line width.

4.2.3 Cross Polarization

Directly pulsing and observing ^{13}C signal is not a very efficient way to analyze solids as the natural abundance of ^{13}C nucleus is about 1%, which means that only 1% of the sample is measured. In addition, T_1 relaxation times in solids can also be very long. Let us consider two coupled spins. Flipflop interactions, i.e. $\alpha\beta$ to $\beta\alpha$ spin flips, can occur spontaneously if the energy levels of the two states are the same. We are interested in transferring spin states from a high natural abundance spin 1/2 nuclei ^1H to ^{13}C . Since these spontaneous flipflop interactions are exceptionally infrequent, due to the different energy levels of the two spin states, cross polarization applies radio frequency fields to equalize the energy levels of the spin states. The flipflop interaction will then transfer spin states to thermodynamical equilibrium between the two spin reservoirs. Not only is cross polarization an effective method for enhancing signal to noise, but the experiment is now bound by the usually shorter T_1 relaxation of protons.

Chapter 5

Rotor Synchronized MAS

5.1 Overview of Rotor Synchronized MAS

A few anisotropic phenomena related to NMR can be investigated for use of morphological studies of fibers. The dipole interaction was experimentally explored in the 1970s by V. J. McBrierty[70] and is now used to investigate mobility of relative C-H segments[71]. The quadrupole interaction is also dependent on molecular orientation but since the quadrupole interaction is more complex and contribute to line broadening, it can be a limiting factor for its use.[68] The static reorientation method, DECODER[13, 55, 56], is dependent on special equipment to rotate the sample about 90° as a part of the pulse sequence, which limits its potential use. The chemical shift anisotropy has been explored with several methods of ROSMAS[10, 45–54, 72, 73]. Rotor synchronization, in contrast, does not require special equipment.

It is easy to qualitatively estimate if a sample is oriented or not using ROSMAS from the side band intensities in the indirect dimension, which are greater for samples with higher molecular order. The great chemical sensitivity enables investigations of composite materials, and order parameters can be determined between different moieties in a sample. Figure 5.1 shows two ROSMAS spectra of melt-spun polyethylene and crystalline nanocellulose composite fibers (15 wt% CNC och 85 wt% EAA (polyethylene with 15 wt% sodium acrylate units) with different levels of molecular orientation. The orientation dependent signal is manifested in the indirect dimension, $M \neq 0$. In Figure 5.1 the polyethylene orientation is visible by eye in the 0-50 ppm region, due to mechanical stretching of the sample. The lower fractional content of cellulose orientation is visible in Figure 5.2. The orientation difference from the impact of stretching is clearly much higher for the polyethylene compared to the nanocellulose.

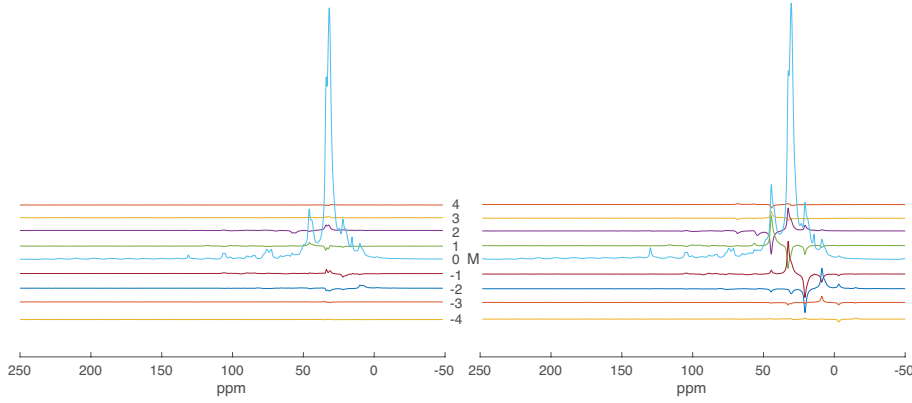


Figure 5.1: Two ROSMAS spectra of melt-spun polyethylene and crystalline nanocellulose composite fibers. non-stretched (left) stretched (right).

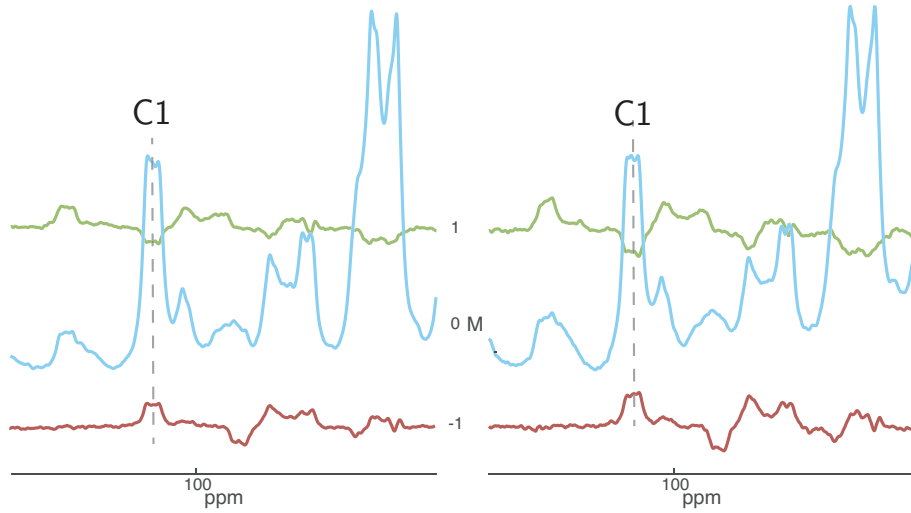


Figure 5.2: Two ROSMAS spectra of melt-spun polyethylene and crystalline nanocellulose composite fibers focusing on the C1 signal of the nanocellulose. non-stretched (left) stretched (right).

For a quantitative description, we have to compare the obtained spectra to theoretically evaluated spectra with an assumed orientation distribution model. Well resolved spectra can in theory be used to determine infinite number of order parameters, but only up to $\langle P_8 \rangle$ has been reported for ROSMAS.[72, 73] In order to use chemical shielding to quantify molecular orientation, the values of the chemical shift anisotropy (CSA), and its orientation with respect to the molecular frame, have to be known *a priori*. A density functional theory approach for the crystalline CSA of cellulose II is therefore used in **Paper I**.

The CSA tensor, CSA orientation with respect to the molecular frame, and order parameters was simultaneously measured accurately by Gabrielse[50, 51] with ^{13}C labeled poly(ethylene terephthalate) (PET). This method that sets both the CSA tensor principal axis components and the Euler angles in the molecular frame tensor, respectively, as free parameters. However, Gabrielse's method will not be spectroscopically possible for regenerated cellulose because of the lower amount of

separable signals from the lower CSA from cellulose. But a variant of this method is demonstrated in **Paper V** on poly(3-hexylthiophene) fibers.

Chemical shielding is spatially dependent, i.e. the magnetic moments within a molecule resonate at different frequencies dependent on the molecule's position relative to the external magnetic field. It is in general difficult to analyze anisotropic samples since a large amount of disordered molecules will produce broad signal distributions. By rotating the sample at high speeds, chemical shielding will average out and therefore anisotropic information is lost. Rotating the sample at slow speeds will produce several peaks, separated by the rotation frequency, as shown in Section 4.2.1. Peaks can be individually evaluated but the essential molecular orientation can not be derived exclusively from a typical cross polarized spectrum. The underlying cause is, that our rotating anisotropic source is sampled at essentially random starting positions, making the CSA effect only shown as an rotational average. To device a pulse sequence with the CSA orientation dependency intact, a rotational dependence is implied by starting a cross polarization pulse sequence with a tachometer trigger, hence preserving the information of the CSA starting position. Figure 5.3 shows a pulse sequence where t_1 is sampled n times over a rotor period. The resulting data set is sequentially Fourier transformed on both directions. After the Fourier transform, the ω_1 axis is denoted by integers of M . The side bands of a single CSA source are denoted on the ω_2 axis by their periodic integer N , which has the shift $N\omega_R$ from its center band. The resulting two dimensional absorption spectrum is phase shifted in the M direction to account for the initial position of the sample in the rotor.

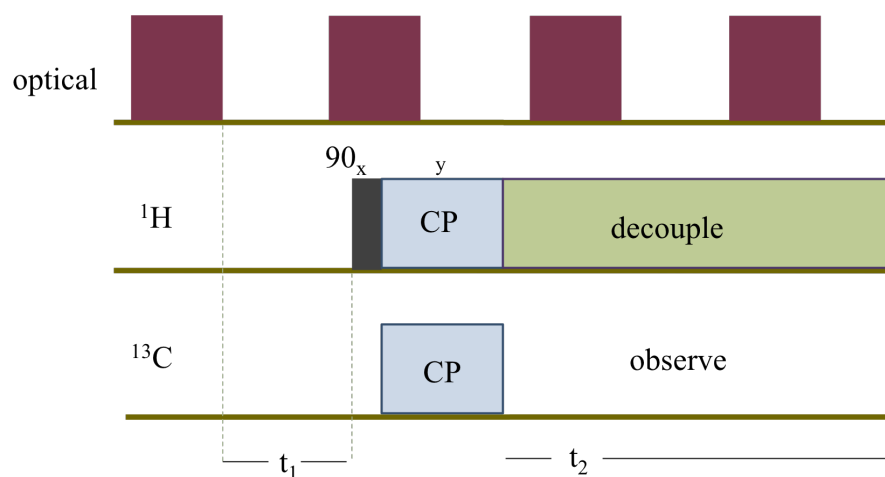


Figure 5.3: Rotor synchronized MAS pulse sequence (ROSMAS) scheme. The optical signal triggers a start of a cross-polarization sequence with a 90° pulse followed by a Hartmann Hahn matched coherence transfer from the abundant H^1 nuclei to C^{13} .

5.2 Sample Preparation

A sample of oriented fibers that physically fits in the NMR rotor has to be made in order to produce spectra with molecular orientation dependence. Therefore, a bundle of fibers is spun around a flat spool and a layer of adhesive is applied. Pieces of glued fiber films are cut out and stacked to produce a cuboid that fits in the rotor. The adhesive does not have a preferred molecular orientation, and will not contribute to the $M \neq 0$ sidebands of the oriented spectra. Figure 5.4 shows an illustration of an oriented fiber bundle with an angle $\beta_1 = 60^\circ$. The optimal angle can usually be found somewhere between $30^\circ - 60^\circ$. For signals that have the CSA tensor parallel to the molecular frame, the optimal angle to maximize the $M = \pm 1$ was found to be 45° , a useful insight for the C1 cellulose signal. No orientation dependence is produced for $\beta_1 = 0^\circ$ since fiber orientation is symmetrical with the rotation of the rotor. For $\beta_1 = 90^\circ$ the experiment is limited with information only located at the $M = 0$ and $M = \pm 2$. [10]

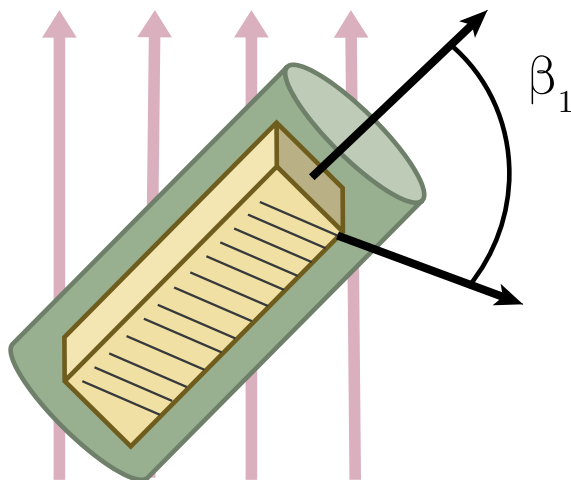


Figure 5.4: Rotor filled with aligned fiber bundle with the rotor at the magic angle and the fiber bundle with fibers at an angle $\beta_1 = 60^\circ$ from the rotor axis.

5.3 Mathematical Description of ROSMAS

As previously mentioned, it is easy to see if a sample is oriented or not since the side band intensities in $M \neq 0$ are greater for samples with a higher molecular order. But for a quantitative description, the obtained spectra has to be compared with a theoretically evaluated spectra with an assumed orientation distribution model. Spiess's ROSMAS [10] model is based on a Herzfeld and Berger analysis, which describes 1D powder patterns for side bands. The extended 2D ROSMAS of an isotropic powder pattern is given by:

$$I_{M,N} = \frac{1}{32\pi^4} \int_0^{2\pi} \int_0^\pi \int_0^{2\pi} K_{M,N}(\alpha_2, \beta_2, \bar{\sigma}) \exp(iM\gamma_2) \sin \beta_2 d\alpha_2 d\beta_2 d\gamma_2 \quad (5.1)$$

with

$$K_{M,N}(\alpha_2, \beta_2, \bar{\sigma}) = \int_0^{2\pi} \int_0^{2\pi} \exp[i(N-M)\omega_R t_1] \exp[-iN\omega_R t_2] F^*(\omega_R t_1) F(\omega_R t_2) d\omega_R t_1 d\omega_R t_2 \quad (5.2)$$

where $\omega_R t_1$ is the variable of integration correlating the CSA tensor rotation in the molecular frame and $\omega_R t_2$ is the rotating effective magnetic field in the rotor frame. The variable ω_R is the rotation speed of the rotor. The integration variables α_2 , β_2 and γ_2 relate the molecular frame to the rotor frame. The function F^* is the complex conjugate of F , where:

$$F(\alpha_2, \beta_2, x) = \exp\left[i\left(\bar{A}_2 \sin 2x - \bar{B}_2 \cos 2x + \bar{A}_1 \sin x - \bar{B}_1 \cos x\right)\right] \quad (5.3)$$

where the variables \bar{A}_1 , \bar{A}_2 , \bar{B}_1 , \bar{B}_2 are:

$$\begin{aligned} \bar{A}_1 = & -\frac{\omega_L \sqrt{2}}{\omega_R 3} \left\{ \sin 2\beta_2 \left[\frac{1}{2} (\sigma_{22} + \sigma_{11}) - \frac{1}{2} (\sigma_{22} - \sigma_{11}) \cos 2\alpha_2 + \sigma_{12} \sin 2\alpha_2 - \sigma_{33} \right] \right. \\ & \left. + 2 \cos 2\beta_2 [\sigma_{13} \cos \alpha_2 + \sigma_{23} \sin \alpha_2] \right\} \end{aligned} \quad (5.4)$$

$$\begin{aligned} \bar{A}_2 = & -\frac{\omega_L}{\omega_R 6} \left\{ (\sigma_{22} + \sigma_{11}) \frac{1}{4} [\cos 2\beta_2 - 1] - \frac{1}{4} (\sigma_{22} - \sigma_{11}) \cos 2\alpha_2 [3 + \cos 2\beta_2] \right. \\ & + \frac{1}{2} \sigma_{12} \sin 2\alpha_2 [3 + \cos 2\beta_2] - \sigma_{13} \sin 2\beta_2 \cos \alpha_2 \\ & \left. - \sigma_{23} \sin \alpha_2 \sin 2\beta_2 + \frac{1}{2} \sigma_{33} [1 - \cos 2\beta_2] \right\} \end{aligned} \quad (5.5)$$

$$\begin{aligned} \bar{B}_1 = & -\frac{\omega_L 2\sqrt{2}}{\omega_R 3} \left\{ \sin \beta_2 \left[\frac{1}{2} (\sigma_{22} - \sigma_{11}) \sin 2\alpha_2 + \sigma_{12} \cos 2\alpha_2 \right] \right. \\ & \left. + \cos \beta_2 [\sigma_{23} \cos \alpha_2 - \sigma_{13} \sin \alpha_2] \right\} \end{aligned} \quad (5.6)$$

$$\begin{aligned} \bar{B}_2 = & -\frac{\omega_L}{\omega_R 3} \left\{ \cos \beta_2 \left[\frac{1}{2} (\sigma_{22} - \sigma_{11}) \sin 2\alpha_2 + \sigma_{12} \cos 2\alpha_2 \right] \right. \\ & \left. + \sin \beta_2 [\sigma_{13} \sin \alpha_2 - \sigma_{23} \cos \alpha_2] \right\} \end{aligned} \quad (5.7)$$

when the principal axis system of the CSA tensor is at a different angle from the molecular frame.

5.4 ROSMAS with Oriented Samples

So far, the uni-axially distributed molecules are not included in the model, for which in principal any ODF may be used to describe the molecular orientation in the fiber. Without specific knowledge about the ODF, a Legendre polynomial distribution is chosen because of its linear and periodic properties by directly multiplying the ODF into Equation (5.1), with θ being the molecular frame deviation from the director frame, i.e. the fiber direction. In the rotor frame, $\cos \theta$ is expressed as:

$$\cos \theta = \sin \beta_1 \sin \beta_2 \cos \gamma_2 + \cos \beta_1 \cos \beta_2 \quad (5.8)$$

where β_1 is the angle the fiber bundle is placed in the rotor. The resulting series of sub spectra then is:

$$I_{M,N} = \sum_{\ell=0}^{\infty} (2\ell + 1) \langle P_{\ell} \rangle \frac{1}{32\pi^4} \int_0^{2\pi} \int_0^{\pi} \int_0^{2\pi} P_{\ell}(\beta_2, \gamma_2) K_{M,N}(\alpha_2, \beta_2, \bar{\sigma}) \exp(iM\gamma_2) \sin \beta_2 d\alpha_2 d\beta_2 d\gamma_2 \quad (5.9)$$

for even ℓ . The experimental side bands are then approximated by the linear sum of sub spectra:

$$(I_{M,N})_{\text{exp}} = \sum_{\ell=0}^{\infty} \langle P_{\ell} \rangle (I_{\ell,M,N})_{\text{calc}} \quad (5.10)$$

Once the resulting sub spectra are calculated, Equation 5.10 can easily evaluated and normalized $\langle P_{\ell} \rangle$ so that $\langle P_0 \rangle = 1$.

5.5 Properties of the ROSMAS Spectrum

A few important properties from the ROSMAS spectra exist that are of specific interest.

- (i) The spectra can be phased to be completely in absorption mode, giving us an important indicator on how well the experiment was performed with the tachometer trigger being a unique error source.
- (ii) The spectra are also symmetric on a diagonal line given by:

$$I_{M,N} = I_{-M,N-M} \quad (5.11)$$

The symmetrical nature of ROSMAS gives us another chance to scrutinize the experimental performance.

- (iii) The intensities at $M = 0$ are all positive and the sum is equal to one for the theoretical spectrum.

$$\sum_N I_{M,N} = 1 \quad \text{for} \quad M = 0 \quad (5.12)$$

Note that:

$$I_{L,M,N} = 0 \quad \text{for} \quad |M| > L \quad (5.13)$$

(iv) The intensities $M \neq 0$ contain both negative and positive contributions and their sum equals to zero:

$$\sum_N I_{M,N} = 0 \quad \text{for} \quad M \neq 0 \quad (5.14)$$

(v) An non-synchronized spectrum can be constructed by summing the signal over the rotor period dimension M :

$$\sum_M I_{M,N} = I_N^{\text{nonsynch}} \quad (5.15)$$

with the additional normalization constraint:

$$\sum_N I_N^{\text{nonsynch}} = 1 \quad (5.16)$$

Phasing of the ROSMAS spectrum is first done by summing the indirect signals by rule (v), followed by a phasing of the direct dimension. Direct dimension phase then is applied to the direct dimension in the ROSMAS 2D spectrum. Phasing the indirect (orientation dependent) dimension is performed with a linear phase. Determining if the signals have a positive or negative intensity requires a bit of knowledge of the molecular structure or by probing the intensity from the theoretical ROSMAS spectrum.

5.6 Derivation of the ROSMAS Experiment

Calculations for the ROSMAS experiment spinning sidebands, which are derived from the Herzfeld and Berger[74] analysis, are made by first defining our experimental reference frames. The reference frames for the experiment are expressed in the "Rotor Frame", and the notation of reference frames are shown in Figure 5.5 and visualized in Figure 5.6. Since the ROSMAS experiment is performed in the rotor frame the other systems have to be described by rotating their respective coordinate system to the rotor frame.

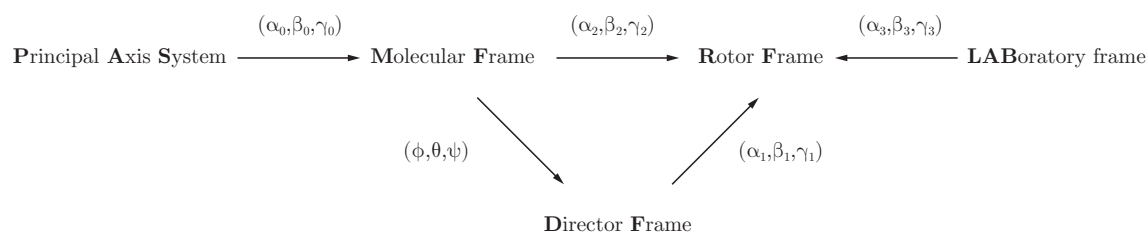


Figure 5.5: The notation of reference frames for the ROSMAS experiment.

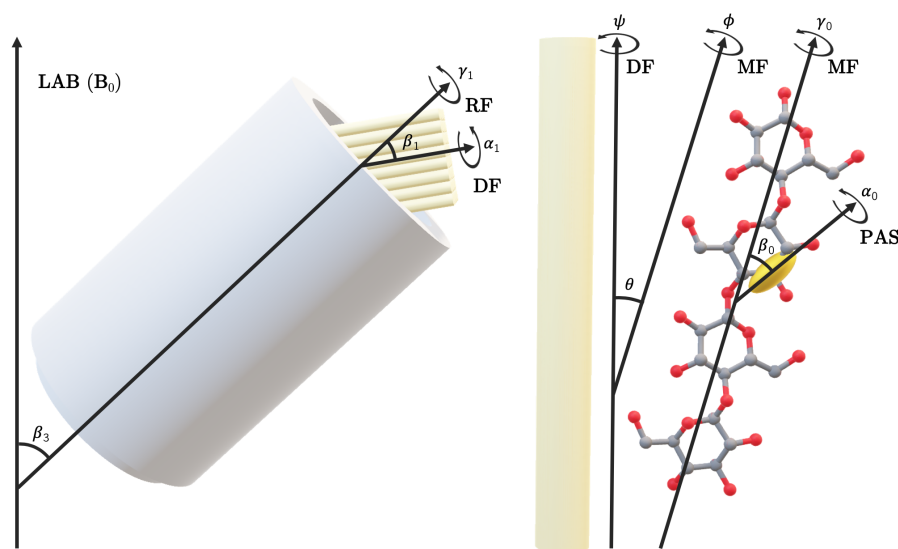


Figure 5.6: Image of the reference frames used in the ROSMAS experiment. Left side portraits a bundle of fibers in a solid state NMR rotor. Right side portraits the molecule and chemical shift anisotropy orientations relative orientations to the fiber axis.

The Larmor frequency shift in the rotating frame is given by the \mathbf{z} , or B_0 , component of the CSA tensor by Equation (5.17), analogous to Equation (4.15).

$$\omega^{\text{RF}} = \gamma B_0 \bar{\mathbf{b}}_{\text{RF}}(t) \bar{\boldsymbol{\sigma}}^{\text{RF}} \bar{\mathbf{b}}_{\text{RF}}^{-1}(t) \quad (5.17)$$

where the time dependent vector $\bar{\mathbf{b}}_{\text{RF}}^{-1}(t)$ is expressed by:

$$\bar{\mathbf{b}}_{\text{RF}}^{-1}(t) = \begin{pmatrix} \sin \beta_3 \cos \gamma_3 \\ \sin \beta_3 \sin \gamma_3 \\ \cos \beta_3 \end{pmatrix} \quad (5.18)$$

with the rotation of $\gamma_{3,0} + \omega_R t$ at the tilt angel β_3 , which is usually set to the magic angle. By expending Equation (5.17) to:

$$\begin{aligned} \omega^{\text{RF}} = \gamma B_0 \left\{ \underbrace{\sigma_{33}^{\text{RF}} \cos^2 \beta_3 + \sin^2 \beta_3 \left[\left(\sigma_{11}^{\text{RF}} \cos^2 \gamma_3 + \sigma_{22}^{\text{RF}} \sin^2 \gamma_3 \right) + \sigma_{12}^{\text{RF}} \sin 2\gamma_3 \right]}_{\omega_{\text{part}}^{\text{RF}}} \right. \\ \left. + 2 \sin \beta_3 \cos \beta_3 \left(\sigma_{13}^{\text{RF}} \cos \gamma_3 + \sigma_{23}^{\text{RF}} \sin \gamma_3 \right) \right\} \end{aligned} \quad (5.19)$$

$$\begin{aligned} \omega_{\text{part}}^{\text{RF}} &= \sigma_{33}^{\text{RF}} \cos^2 \beta_3 \\ &+ \frac{1}{2} \sin^2 \beta_3 \left[\underbrace{\left(\sigma_{11}^{\text{RF}} + \sigma_{22}^{\text{RF}} - \underbrace{(\sigma_{11}^{\text{RF}} + \sigma_{22}^{\text{RF}})(\sin^2 \gamma_3 + \cos^2 \gamma_3)}_{\sin^2 \beta_3 \frac{1}{2} (\sigma_{11}^{\text{RF}} - \sigma_{22}^{\text{RF}}) \cos 2\gamma_3} \right)}_{\sin^2 \beta_3 \frac{1}{2} (\sigma_{11}^{\text{RF}} - \sigma_{22}^{\text{RF}}) \cos 2\gamma_3} + \sigma_{11}^{\text{RF}} \cos^2 \gamma_3 + \sigma_{22}^{\text{RF}} \sin^2 \gamma_3 \right] \\ \omega_{\text{part}}^{\text{RF}} &= \underbrace{\sigma_{33}^{\text{RF}} \cos^2 \beta_3 + \frac{1}{2} \sin^2 \beta_3 (\sigma_{11}^{\text{RF}} + \sigma_{22}^{\text{RF}})}_{\sigma_{\text{iso}} + \frac{1}{2} (3 \cos^2 \beta_3 - 1) (\sigma_{33}^{\text{RF}} - \sigma_{\text{iso}})} + \sin^2 \beta_3 \frac{1}{2} (\sigma_{11}^{\text{RF}} - \sigma_{22}^{\text{RF}}) \cos 2\gamma_3 \end{aligned} \quad (5.20)$$

We get Equation (5.21), similar to *Equation 4* from Herzfeld and Berger[74].

$$\begin{aligned} \omega^{\text{RF}} = -\gamma B_0 \left\{ \sigma_{\text{iso}} + \frac{1}{2} (3 \cos^2 \beta_3 - 1) (\sigma_{33}^{\text{RF}} - \sigma_{\text{iso}}) \right. \\ \left. + \sin^2 \beta_3 \left[\frac{1}{2} (\sigma_{11}^{\text{RF}} - \sigma_{22}^{\text{RF}}) \cos 2\gamma_3 + \sigma_{12}^{\text{RF}} \sin 2\gamma_3 \right] \right. \\ \left. + 2 \sin \beta_3 \cos \beta_3 (\sigma_{13}^{\text{RF}} \cos \gamma_3 + \sigma_{23}^{\text{RF}} \sin \gamma_3) \right\} \end{aligned} \quad (5.21)$$

with

$$\sigma_{\text{iso}} = \frac{1}{3} (\sigma_{11}^{\text{RF}} + \sigma_{22}^{\text{RF}} + \sigma_{33}^{\text{RF}}) \quad (5.22)$$

which also extends to the MF diagonal tensor and the PAS tensor:

$$\sigma_{\text{iso}} = \sigma_{\text{iso}}^{\text{MF}} = \sigma_{\text{iso}}^{\text{PAS}} \quad (5.23)$$

Equation (5.23) can be derived directly from solving Equation (5.26). The rotational sideband intensities calculated by Herzfeld and Berger are independent from tensor orientations. A typical pulse sequence has no information on tensor orientation due to the spatially random component in the rotor spinning. To this extent the Herzfeld and Berger sidebands were derived with the CSA tensor parallel to the molecular frame, described only by the principal axis system components of the tensor, as in Equation (5.24).

$$\sigma^{\text{PAS}} = \begin{pmatrix} \sigma_{11}^{\text{PAS}} & 0 & 0 \\ 0 & \sigma_{22}^{\text{PAS}} & 0 \\ 0 & 0 & \sigma_{33}^{\text{PAS}} \end{pmatrix} \quad (5.24)$$

Since the tensor orientation will be important to the ROSMAS experiment, we have to derive the ROSMAS model with the molecular frame CSA tensor in a more general, non-diagonal, form.

$$\sigma^{\text{MF}} = \begin{pmatrix} \sigma_{11} & \sigma_{12} & \sigma_{13} \\ \sigma_{21} & \sigma_{22} & \sigma_{23} \\ \sigma_{31} & \sigma_{32} & \sigma_{33} \end{pmatrix} \quad (5.25)$$

The CSA tensor σ^{RF} components is related to the molecular frame CSA tensor by:

$$\sigma^{\text{RF}} = \mathbf{R}(\alpha_2, \beta_2, \gamma_2) \sigma^{\text{MF}} \mathbf{R}^{-1}(\alpha_2, \beta_2, \gamma_2) \quad (5.26)$$

where \mathbf{R} is the Euler rotation matrix.

Due to the lack of conventions on how tensor rotations are performed, it is crucial to have an understanding of the tensor rotation formalism. A summary of tensor rotations in NMR was made by Mueller,[75] and the concepts will be reviewed here. Mueller describes an active rotation, where the object is moved in from a fixed observer, as a Z-Y-Z rotation. Simply, the object is first rotated by the angle ϕ around the Z-axis, chosen to coincide with the σ_{33} direction. The rotation is followed by a Y-rotation in the new system with the angle θ , followed by another Z-rotation with the angle ψ .

As a personal note: Several sources of literature explains Euler rotations this way. However, I have found it more useful to evaluate rotations from the perspective, in the context of a CSA tensor, that the coordinate system is *always* rotated. The rotations are then first applied by its innermost elementary rotation, which for an active rotation is ψ . The elementary rotations for an active rotation are shown in Equation (5.6). The reason to stay consistent with exclusive coordinate transformations is to show that performing a reverse active rotation (i.e. passive rotation) sequentially

after an active rotation will return the tensor to its original coordinate system, as shown by Equation (5.29).

$$\begin{aligned}\mathbf{R}_{\text{active}}(\phi, \theta, \psi) &= \mathbf{R}_Z(\phi)\mathbf{R}_Y(\theta)\mathbf{R}_Z(\psi) \\ &= \begin{pmatrix} \cos \phi & -\sin \phi & 0 \\ \sin \phi & \cos \phi & 0 \\ 0 & 0 & 1 \end{pmatrix} \begin{pmatrix} \cos \theta & 0 & \sin \theta \\ 0 & 1 & 0 \\ -\sin \theta & 0 & \cos \theta \end{pmatrix} \begin{pmatrix} \cos \psi & -\sin \psi & 0 \\ \sin \psi & \cos \psi & 0 \\ 0 & 0 & 1 \end{pmatrix} \quad (5.27)\end{aligned}$$

Herzfeld and Berger and previous ROSMAS users do not use the active Z-Y-Z rotation notation.[10, 49–51, 74] They instead opt for a passive Z-Y-Z rotation. The passive rotation can be rewritten for positive angles such that:

$$\begin{aligned}\mathbf{R}_{\text{passive}}(\phi, \theta, \psi) &= \mathbf{R}_Z^{-1}(\psi)\mathbf{R}_Y^{-1}(\theta)\mathbf{R}_Z^{-1}(\phi) \\ &= \begin{pmatrix} \cos \psi & \sin \psi & 0 \\ -\sin \psi & \cos \psi & 0 \\ 0 & 0 & 1 \end{pmatrix} \begin{pmatrix} \cos \theta & 0 & -\sin \theta \\ 0 & 1 & 0 \\ \sin \theta & 0 & \cos \theta \end{pmatrix} \begin{pmatrix} \cos \phi & \sin \phi & 0 \\ -\sin \phi & \cos \phi & 0 \\ 0 & 0 & 1 \end{pmatrix} \quad (5.28)\end{aligned}$$

The identity matrix \mathbf{I}_3 relation is then:

$$\mathbf{I}_3 = \mathbf{R}_{\text{passive}}(\phi, \theta, \psi) \mathbf{R}_{\text{active}}(\phi, \theta, \psi) \mathbf{I}_3 \mathbf{R}_{\text{active}}(\phi, \theta, \psi)^{-1} \mathbf{R}_{\text{passive}}(\phi, \theta, \psi)^{-1} \quad (5.29)$$

The rotation from the CSA tensor PAS to the MF has to be performed with a known CSA and its corresponding Euler angles. In **Paper II** the PAS to MF rotation was calculated with Gaussian[76] DFT modelling with an active Z-X-Z rotation.

To follow the previous derivation of the ROSMAS experiment, the passive Z-Y-Z rotation $\mathbf{R}_{\text{passive}}$ has to be used to rotate from the molecular frame to the rotor frame with Equation (5.26). Due to the somewhat messy operation of solving Equation (5.26), it can be challenging to arrive to the equivalent of Herzfeld and Berger *Equation 16*[74].

The trick is to assume a matrix with the α_2 and β_2 rotations as:

$$\mathbf{Q}(\alpha_2, \beta_2) = \begin{pmatrix} q_{11} & q_{12} & q_{13} \\ q_{21} & q_{22} & q_{23} \\ q_{31} & q_{32} & q_{33} \end{pmatrix} = \mathbf{R}_Y^{-1}(\beta_2)\mathbf{R}_Z^{-1}(\alpha_2)\boldsymbol{\sigma}^{\text{MF}}\left(\mathbf{R}_Y^{-1}(\beta_2)\mathbf{R}_Z^{-1}(\alpha_2)\right)^{-1} \quad (5.30)$$

A simpler system can now be solved for γ_2 , which will show to be a rotation parallel to the time dependent rotor rotation γ_3 . The intermediate solution is then:

$$\boldsymbol{\sigma}^{\text{RF}} = \mathbf{R}_Z^{-1}(\gamma_2) \mathbf{Q}(\alpha_2, \beta_2) \left(\mathbf{R}_Z^{-1}(\gamma_2) \right)^{-1} \quad (5.31)$$

$$= \begin{pmatrix} \cos \gamma_2 (q_{11} \cos \gamma_2 + q_{12} \sin \gamma_2) + \sin \gamma_2 (q_{12} \cos \gamma_2 + q_{22} \sin \gamma_2) \\ \cos \gamma_2 (q_{12} \cos \gamma_2 - q_{11} \sin \gamma_2) + \sin \gamma_2 (q_{22} \cos \gamma_2 - q_{12} \sin \gamma_2) \\ q_{13} \cos \gamma_2 + q_{23} \sin \gamma_2 \\ \\ \cos \gamma_2 (q_{12} \cos \gamma_2 + q_{22} \sin \gamma_2) - \sin \gamma_2 (q_{11} \cos \gamma_2 + q_{12} \sin \gamma_2) \\ \cos \gamma_2 (q_{22} \cos \gamma_2 - q_{12} \sin \gamma_2) - \sin \gamma_2 (q_{12} \cos \gamma_2 - q_{11} \sin \gamma_2) \\ q_{23} \cos \gamma_2 - q_{13} \sin \gamma_2 \\ \\ q_{13} \cos \gamma_2 + q_{23} \sin \gamma_2 \\ q_{23} \cos \gamma_2 - q_{13} \sin \gamma_2 \\ q_{33} \end{pmatrix} \quad (5.32)$$

It is now easier to express the $\boldsymbol{\sigma}^{\text{RF}}$ components in Equation (5.21).

$$\begin{aligned} \frac{\sigma_{11}^{\text{RF}} - \sigma_{22}^{\text{RF}}}{2} &= \frac{q_{11}}{2} \underbrace{(\cos^2 \gamma_2 - \sin^2 \gamma_2)}_{\cos 2\gamma_2} + \frac{q_{22}}{2} \underbrace{(\sin^2 \gamma_2 - \cos^2 \gamma_2)}_{-\cos 2\gamma_2} \\ &\quad + q_{12} \underbrace{2 \cos \gamma_2 \sin \gamma_2}_{\sin 2\gamma_2} \\ &= \cos 2\gamma_2 \frac{q_{11} - q_{22}}{2} + q_{12} \sin 2\gamma_2 \\ &= A_2 \cos 2\gamma_2 + B_2 \sin 2\gamma_2 \end{aligned} \quad (5.33)$$

$$\begin{aligned} \sigma_{12}^{\text{RF}} &= \underbrace{(\cos^2 \gamma_2 - \sin^2 \gamma_2)}_{\cos 2\gamma_2} q_{12} - \underbrace{\sin \gamma_2 \cos \gamma_2}_{\frac{\sin 2\gamma_2}{2}} (q_{11} - q_{22}) \\ &= B_2 \cos 2\gamma_2 - A_2 \sin 2\gamma_2 \end{aligned} \quad (5.34)$$

$$\begin{aligned} \sigma_{13}^{\text{RF}} &= q_{13} \cos \gamma_2 + q_{23} \sin \gamma_2 \\ &= A_1 \cos \gamma_2 + B_1 \sin \gamma_2 \end{aligned} \quad (5.35)$$

$$\begin{aligned} \sigma_{23}^{\text{RF}} &= q_{23} \cos \gamma_2 - q_{13} \sin \gamma_2 \\ &= B_1 \cos \gamma_2 - A_1 \sin \gamma_2 \end{aligned} \quad (5.36)$$

Inserting Equations (5.33)-(5.36) into Equation (5.21), while setting β_3 to the magic angle, we end up with the following expression:

$$\begin{aligned}
\omega^{\text{RF}} = \gamma B_0 \Big\{ & \sigma_{\text{iso}} + \frac{2}{3} \Big(A_2 \cos 2\gamma_2 \cos 2\gamma_3 + B_2 \sin 2\gamma_2 \cos 2\gamma_3 \\
& + B_2 \cos 2\gamma_2 \sin 2\gamma_3 - A_2 \sin 2\gamma_2 \sin 2\gamma_3 \Big) \\
& + \frac{2}{3} \sqrt{2} \Big(A_1 \cos \gamma_2 \cos \gamma_3 + B_1 \sin \gamma_2 \cos \gamma_3 \\
& + B_1 \cos \gamma_2 \sin \gamma_3 - A_1 \sin \gamma_2 \sin \gamma_3 \Big) \Big\} \quad (5.37)
\end{aligned}$$

$$\begin{aligned}
\omega^{\text{RF}} = \gamma B_0 \Big\{ & \sigma_{\text{iso}} + \frac{2}{3} \Big(A_2 \cos (2\gamma_3 + 2\gamma_2) + B_2 \sin (2\gamma_3 + 2\gamma_2) \Big) \\
& + \frac{2}{3} \sqrt{2} \Big(A_1 \cos (\gamma_3 + \gamma_2) + B_1 \sin (\gamma_3 + \gamma_2) \Big) \Big\} \quad (5.38)
\end{aligned}$$

The constants A_2 , B_2 , A_1 and B_1 are expressed by solving Equation (5.30) with:

$$\begin{aligned}
A_2 = \frac{q_{11} - q_{22}}{2} = \frac{1}{2} \Big\{ & \sigma_{11} \cos^2 \alpha_2 \cos^2 \beta_2 - \sigma_{11} \sin^2 \alpha_2 \\
& - \sigma_{22} \cos^2 \alpha_2 + \sigma_{22} \cos^2 \beta_2 \sin^2 \alpha_2 \\
& + 2 \sigma_{12} \cos \alpha_2 \cos^2 \beta_2 \sin \alpha_2 + \sigma_{12} \sin 2\alpha_2 \\
& - 2 \sigma_{13} \cos \alpha_2 \cos \beta_2 \sin \beta_2 \\
& - 2 \sigma_{23} \cos \beta_2 \sin \alpha_2 \sin \beta_2 \\
& + \sigma_{33} \sin^2 \beta_2 \Big\} \quad (5.39)
\end{aligned}$$

With some reshuffling A_2 becomes:

$$\begin{aligned}
A_2 = \frac{1}{2} \Big\{ & \frac{1}{4} (\sigma_{22} + \sigma_{11}) [\cos 2\beta_2 - 1] - \frac{1}{4} (\sigma_{22} - \sigma_{11}) \cos 2\alpha_2 [3 + \cos 2\beta_2] \\
& + \frac{1}{2} \sigma_{12} \sin 2\alpha_2 [3 + \cos 2\beta_2] - \sigma_{13} \sin 2\beta_2 \cos \alpha_2 \\
& - \sigma_{23} \sin \alpha_2 \sin 2\beta_2 + \frac{1}{2} \sigma_{33} [1 - \cos 2\beta_2] \Big\} \quad (5.40)
\end{aligned}$$

$$\begin{aligned}
B_2 = q_{12} = \cos \alpha \Big(& \sigma_{12} \cos \alpha \cos \beta - \sigma_{23} \sin \beta + \sigma_{22} \cos \beta \sin \alpha \Big) \\
& - \sin \alpha \Big(\sigma_{11} \cos \alpha \cos \beta - \sigma_{13} \sin \beta + \sigma_{12} \cos \beta \sin \alpha \Big) \quad (5.41)
\end{aligned}$$

$$\begin{aligned}
B_2 = \cos \beta_2 \Big[& \frac{1}{2} (\sigma_{22} - \sigma_{11}) \sin 2\alpha_2 + \sigma_{12} \cos 2\alpha_2 \Big] \\
& + \sin \beta_2 [\sigma_{13} \sin \alpha_2 - \sigma_{23} \cos \alpha_2] \quad (5.42)
\end{aligned}$$

$$\begin{aligned}
A_1 = q_{13} = & \cos \beta_2 (q_{13} \cos \alpha_2 \cos \beta_2 - q_{33} \sin \beta_2 + q_{23} \cos \beta_2 \sin \alpha_2) \\
& + \cos \alpha_2 \sin \beta_2 (q_{11} \cos \alpha_2 \cos \beta_2 - q_{13} \sin \beta_2 + q_{12} \cos \beta_2 \sin \alpha_2) \\
& + \sin \alpha_2 \sin \beta_2 (q_{12} \cos \alpha_2 \cos \beta_2 - q_{23} \sin \beta_2 + q_{22} \cos \beta_2 \sin \alpha_2) \quad (5.43)
\end{aligned}$$

$$\begin{aligned}
A_1 = & \frac{1}{2} \sin 2\beta_2 \left[\frac{1}{2} (\sigma_{22} + \sigma_{11}) - \frac{1}{2} (\sigma_{22} - \sigma_{11}) \cos 2\alpha_2 + \sigma_{12} \sin 2\alpha_2 - \sigma_{33} \right] \\
& + \cos 2\beta_2 [\sigma_{13} \cos \alpha_2 + \sigma_{23} \sin \alpha_2] \quad (5.44)
\end{aligned}$$

$$\begin{aligned}
B_1 = q_{23} = & \cos \beta_2 (q_{23} \cos \alpha_2 - q_{13} \sin \alpha_2) \\
& + \cos \alpha_2 \sin \beta_2 (q_{12} \cos \alpha_2 - q_{11} \sin \alpha_2) \\
& + \sin \alpha_2 \sin \beta_2 (q_{22} \cos \alpha_2 - q_{12} \sin \alpha_2) \quad (5.45)
\end{aligned}$$

$$\begin{aligned}
B_1 = & \sin \beta_2 \left[\frac{1}{2} (\sigma_{22} - \sigma_{11}) \sin 2\alpha_2 + \sigma_{12} \cos 2\alpha_2 \right] \\
& + \cos \beta_2 [\sigma_{23} \cos \alpha_2 - \sigma_{13} \sin \alpha_2] \quad (5.46)
\end{aligned}$$

The free induction decay $g(t)$ of the sample is determined by:

$$g(t) = \frac{1}{8\pi^2} \int_0^{2\pi} \int_0^\pi \int_0^{2\pi} \exp[i\theta(\alpha_2, \beta_2, \gamma_2, t)] \sin \beta_2 d\alpha_2 d\beta_2 d\gamma_2 \quad (5.47)$$

By inserting the rotational dependence of the rotor frequency $\gamma_3 = \gamma_{3,0} + \omega_R t$ we get:

$$\begin{aligned}
\theta(\alpha_2, \beta_2, \gamma_2, t) = & \int_0^t \omega(\alpha_2, \beta_2, \gamma_2, t) dt \\
= & -\gamma B_0 \sigma_{\text{iso}} t + f(\gamma_{3,0} + \omega_R t + \gamma_2) - f(\gamma_{3,0} + \gamma_2) \quad (5.48)
\end{aligned}$$

with:

$$\begin{aligned}
f(x) = & -\omega_L \left(\frac{2}{3 \cdot 2\omega_R} A_2 \sin 2x - \frac{2}{3 \cdot 2\omega_R} B_2 \cos 2x + \frac{2\sqrt{2}}{3\omega_R} A_1 \sin x - \frac{2\sqrt{2}}{3\omega_R} B_1 \cos x \right) \\
= & \bar{A}_2 \sin 2x - \bar{B}_2 \cos 2x + \bar{A}_1 \sin x - \bar{B}_1 \cos x \quad (5.49)
\end{aligned}$$

for the Larmor frequency $\gamma B_0 = \omega_L$.

To introduce the two-dimensional ROSMAS experiment the rotating magnetic field is expressed in the rotor frame $\omega_R t_2$, i.e. the direct dimension. The rotating CSA tensor $\omega_R t_1$ is Fourier transformed over the rotor period i.e. the indirect dimension. A rotation around γ_2 will evolve the rotor phase and therefore imply the rotor phase dependence in the ROSMAS experiment. With the two correlation times in mind, $\omega_R t_1$ is expressed as a rotation around γ_2 :

$$\theta(\alpha, \beta, \gamma, t_1, t_2) = -\gamma B_0 \sigma_{\text{iso}} t_2 + f(\gamma_{3,0} + \omega_R t_1 + \omega_R t_2 + \gamma_2) - f(\gamma_{0,3} + \omega_R t_1 + \gamma_2) \quad (5.50)$$

The function $F(x)$ is defined as:

$$F(x) = \exp[if(x)] \quad (5.51)$$

and:

$$G(\omega_R t_1, \omega_R t_2) = F(\gamma_{3,0} + \omega_R t_1 + \omega_R t_2 + \gamma_2) F^*(\gamma_{3,0} + \omega_R t_1 + \gamma_2) \quad (5.52)$$

Then, the free induction decay can be written as:

$$g(t_1, t_2) = \frac{1}{8\pi^2} \exp(-i\gamma B_0 \sigma_{\text{iso}} t_2) \int_0^{2\pi} \int_0^\pi \int_0^{2\pi} G(\omega_R t_1, \omega_R t_2) \sin \beta_2 \, d\alpha_2 \, d\beta_2 \, d\gamma_2 \quad (5.53)$$

The $G(\omega_R t_1, \omega_R t_2)$ is a periodic function and can then be expanded as a double complex Fourier series:

$$G(\omega_R t_1, \omega_R t_2) = \sum_{N=-\infty}^{\infty} \sum_{M=-\infty}^{\infty} G_{M,N} \exp(-iN\omega_R t_2) \exp(-iM\omega_R t_1) \quad (5.54)$$

with the coefficients $G_{M,N}$:

$$G_{M,N} = \frac{1}{4\pi^2} \int_0^{2\pi} \int_0^{2\pi} G(\omega_R t_1, \omega_R t_2) \exp(-iN\omega_R t_2) \exp(-iM\omega_R t_1) \, d\omega_R t_1 \, d\omega_R t_2 \quad (5.55)$$

By inserting Equation (5.54) into (5.53) and identifying the resulting equation as the discrete Fourier transform of Equation (5.53) at the isotropic shift $\gamma B_0 \sigma_{\text{iso}}$ with sideband intensities at $\omega_1 = M\omega_R$ and $\omega_2 = \omega_L \sigma_{\text{iso}} + N\omega_R$, we get:

$$I_{M,N} = \frac{1}{8\pi^2} \int_0^{2\pi} \int_0^\pi \int_0^{2\pi} G_{M,N} \sin \beta_2 \, d\alpha_2 \, d\beta_2 \, d\gamma_2 \quad (5.56)$$

To arrive at the final expression we have to simplify $G_{M,N}$ further:

$$G_{M,N} = \frac{1}{4\pi^2} \int_0^{2\pi} \left[\underbrace{\int_0^{2\pi} F(\gamma_{3,0} + \omega_R t_1 + \omega_R t_2 + \gamma_2) \exp(-iN\omega_R t_2) \, d\omega_R t_2}_{\Lambda_1} \times F^*(\gamma_{3,0} + \omega_R t_1 + \gamma_2) \exp(-iM\omega_R t_1) \right] d\omega_R t_1 \quad (5.57)$$

Λ_1 can be expressed as:

$$\begin{aligned}
\Lambda_1 &= \int_0^{2\pi} F(\gamma_{3,0} + \omega_R t_1 + \omega_R t_2 + \gamma_2) \exp(-iN\omega_R t_2) \exp[-iN(\gamma_{3,0} + \omega_R t_1 + \gamma_2)] \\
&\quad \times \exp[iN(\gamma_{3,0} + \omega_R t_1 + \gamma_2)] d\omega_R t_2 \\
&= \int_0^{2\pi} F(\gamma_{3,0} + \omega_R t_1 + \omega_R t_2 + \gamma_2) \exp[-iN(\gamma_{3,0} + \omega_R t_1 + \omega_R t_2 + \gamma_2)] \\
&\quad \times \exp[iN(\gamma_{3,0} + \omega_R t_1 + \gamma_2)] d\omega_R t_2 \\
&= \int_0^{2\pi} F(\omega_R t_2) \exp(-iN\omega_R t_2) \exp[iN(\gamma_{3,0} + \omega_R t_1 + \gamma_2)] d\omega_R t_2 \quad (5.58)
\end{aligned}$$

Recognizing that $\gamma_{3,0} + \omega_R t_1 + \gamma_2$ can be discarded, being constants in a periodic function on the periodic interval. Inserting Λ_1 back into Equation (5.57) we get:

$$\begin{aligned}
G_{M,N} &= \frac{1}{4\pi^2} \underbrace{\int_0^{2\pi} F^*(\gamma_{3,0} + \omega_R t_1 + \gamma_2) \exp(-iM\omega_R t_1) \exp[iN(\gamma_{3,0} + \omega_R t_1 + \gamma_2)] d\omega_R t_1}_{\Lambda_2} \\
&\quad \times \int_0^{2\pi} F(\omega_R t_2) \exp(-iN\omega_R t_2) d\omega_R t_2 \quad (5.59)
\end{aligned}$$

Λ_2 can be expressed as:

$$\begin{aligned}
\Lambda_2 &= \int_0^{2\pi} F^*(\gamma_{3,0} + \omega_R t_1 + \gamma_2) \exp(-iM\omega_R t_1) \exp[-iM(\gamma_{3,0} + \gamma_2)] \\
&\quad \times \exp[iN(\gamma_{3,0} + \omega_R t_1 + \gamma_2)] \exp[iM(\gamma_{3,0} + \gamma_2)] d\omega_R t_1 \\
&= \int_0^{2\pi} F^*(\gamma_{3,0} + \omega_R t_1 + \gamma_2) \exp[-iM(\gamma_{3,0} + \omega_R t_1 + \gamma_2)] \\
&\quad \times \exp[iN(\gamma_{3,0} + \omega_R t_1 + \gamma_2)] \exp[iM(\gamma_{3,0} + \gamma_2)] d\omega_R t_1 \\
&= \int_0^{2\pi} F^*(\omega_R t_1) \exp[i(N-M)\omega_R t_1] \exp[iM(\gamma_{3,0} + \gamma_2)] d\omega_R t_1 \quad (5.60)
\end{aligned}$$

Inserting Λ_2 back into Equation (5.57) and we get Equation (5.1). One may notice that the normalization of $32/\pi$ is different from the literature[10], though later works seem to have corrected it.[48] Computation of the ROSMAS experiment also confirms its correctness. One explanation for irregularities in the literature could be that to add the molecular orientation distribution function, the ODF is simply multiplied into Equation (5.1). The Legendre polynomials are often referenced with a normalization of a one dimensional system as in Equation (5.61):

$$\sum_{\ell=0}^{\infty} \frac{2\ell+1}{2} \cdot \langle P_\ell \rangle \cdot P_\ell(\cos \theta) \quad (5.61)$$

Over all Euler angles, a normalization with $1/(8\pi^2)$ must be applied.[10, 77] This normalization is performed on the FID function $g(t_1, t_2)$ in Equation (5.53).

Therefore, there is no need to normalize the Legendre polynomials again. The Legendre polynomials without normalization are given by:

$$\sum_{\ell=0}^{\infty} (2\ell + 1) \cdot \langle P_{\ell} \rangle \cdot P_{\ell}(\cos \theta) \quad (5.62)$$

with θ as the angle between the director frame and the molecular frame.

The function $\cos \theta$ can be expressed in terms of:

$$\cos \theta = \sin \beta_1 \sin \beta_2 \cos \gamma_2 + \cos \beta_1 \cos \beta_2 \quad (5.63)$$

The relation in Equation (5.63) was previously pointed out by Harbison et al.,[10] but a more transparent proof is presented here. The Euler rotations between the rotor frame, molecular frame and director are expressed as:

$$\sigma^{\text{RF}} = \mathbf{R}(\alpha_1, \beta_1, \gamma_1) \sigma^{\text{DF}} \mathbf{R}^{-1}(\alpha_1, \beta_1, \gamma_1) \quad (5.64)$$

$$\sigma^{\text{RF}} = \mathbf{R}(\alpha_2, \beta_2, \gamma_2) \sigma^{\text{MF}} \mathbf{R}^{-1}(\alpha_2, \beta_2, \gamma_2) \quad (5.65)$$

$$\sigma^{\text{DF}} = \mathbf{R}(\phi, \theta, \psi) \sigma^{\text{MF}} \mathbf{R}^{-1}(\phi, \theta, \psi) \quad (5.66)$$

By inserting equation Equation (5.66) into Equation (5.64), we find the equality:

$$\mathbf{R}(\alpha_2, \beta_2, \gamma_2) = \mathbf{R}(\alpha_1, \beta_1, \gamma_1) \mathbf{R}(\phi, \theta, \psi) \quad (5.67)$$

By recognizing:

$$\begin{aligned} \mathbf{R}_{33}(\phi, \theta, \psi) &= \cos \theta = (\mathbf{R}(\alpha_1, \beta_1, \gamma_1) \mathbf{R}(\alpha_2, \beta_2, \gamma_2))_{33} = \\ &\sin \beta_1 \cos \gamma_1 \sin \beta_2 \cos \gamma_2 + \sin \beta_1 \sin \gamma_1 \sin \beta_2 \sin \gamma_2 + \cos \beta_1 \cos \beta_2 \end{aligned} \quad (5.68)$$

and setting $\gamma_1 = 0$, as this experimental independent angle can be chosen freely, we find the equality in Equation (5.63). When the Legendre polynomial is multiplied into Equation (5.1), while setting β_1 to the fiber angle from the rotor z-axis, we get the final expression:

$$\begin{aligned} I_{\text{M,N}} &= \sum_{\ell=0}^{\infty} (2\ell + 1) \langle P_{\ell} \rangle \frac{1}{32\pi^4} \cdot \\ &\int_0^{2\pi} \int_0^{\pi} \int_0^{2\pi} P_{\ell}(\beta_2, \gamma_2) K_{\text{M,N}}(\alpha_2, \beta_2, \bar{\sigma}) \exp(iM\gamma_2) \sin \beta_2 \, d\alpha_2 \, d\beta_2 \, d\gamma_2 \end{aligned} \quad (5.69)$$

Chapter 6

Polarized Raman Spectroscopy

6.1 Overview of the Polarized Raman Spectroscopy Experiment

The phenomenon of Raman scattering was first discovered by Sir Chandrasekhara Venkata Raman in 1928 for which he received the Nobel Prize in 1930. With Raman spectroscopy it is possible to analyze the vibrations of molecular bonds while perturbed by an incident light source, typically a monochromatic laser with a wavelength in the 250-1000 nm wavelength region. The Raman interaction is an inelastic scattering during which the incoming light interacts with matter, i.e. with the molecular bonds, and the scattered light loses or gains some of its energy. The majority of light is back scattered with no energy loss (Rayleigh scattering), while a minor portion of light is scattered with a lower (Stokes shift) or higher (anti-Stokes shift) frequency than that of the incident light. In order to catch these events, band pass filters are included in the optical path of the scattered light. Raman and infrared spectroscopy are closely related, although they are sensitive to different bond properties (polarizability and dipole moment, respectively), wherefore they also are complementary. According to some selection rules, some vibrational modes that are sensitive to Raman are not sensitive to infrared, and vice versa.[78]

A method, based on Raman spectroscopy, has been developed by Bower[11] to investigate molecular orientation distributions in polymeric fibers. Bower's classical approach allows polarized light to interact with the Raman vibrational tensor and is subsequently analyzed through a polarization filter. Bower showed that the scattered intensity can be written in the form of Equation (6.1), where α is the Raman tensor, $f(\theta)$ is the implied uni-axial molecular orientation distribution, I_0 is the laser intensity and N_0 is the number of chain elements, illuminated by the laser. The only currently available model is the one that assumes the PAS Raman tensor to coincide with the MF.[59–61, 63, 64, 79] This limits the number of vibrational modes that can be quantitatively analyzed. Moreover, the Euler angles relevant to the polarized Raman experiments ϕ , θ , and ψ describe the transformation from directly the PAS to the fiber DF as in Equation 6.1:

$$I_0 \sum \alpha_{ij} \alpha_{pq} = I_0 N_0 \int_0^{2\pi} \int_0^\pi \int_0^{2\pi} f(\theta) \alpha_{ij} \alpha_{pq} \sin \theta \, d\phi \, d\theta \, d\psi \quad (6.1)$$

By using the tensor identity,

$$\alpha_{ij} = \sum_{k=1}^3 a_{ik} a_{jk} \alpha_k \quad (6.2)$$

where a is a component of a rotational matrix, the intensity can be described in terms of the principal axis components and the implied ODF. I suggest that the polarized Raman experiment could be rewritten in a general form that includes the tensor orientation relative to the molecular frame. For my own amusement, the polarized Raman experiment with an arbitrarily oriented Raman tensor is derived for the first time (to my current knowledge) here. The reference frames are shown in Figure 6.1 and visualized in Figure 6.2.

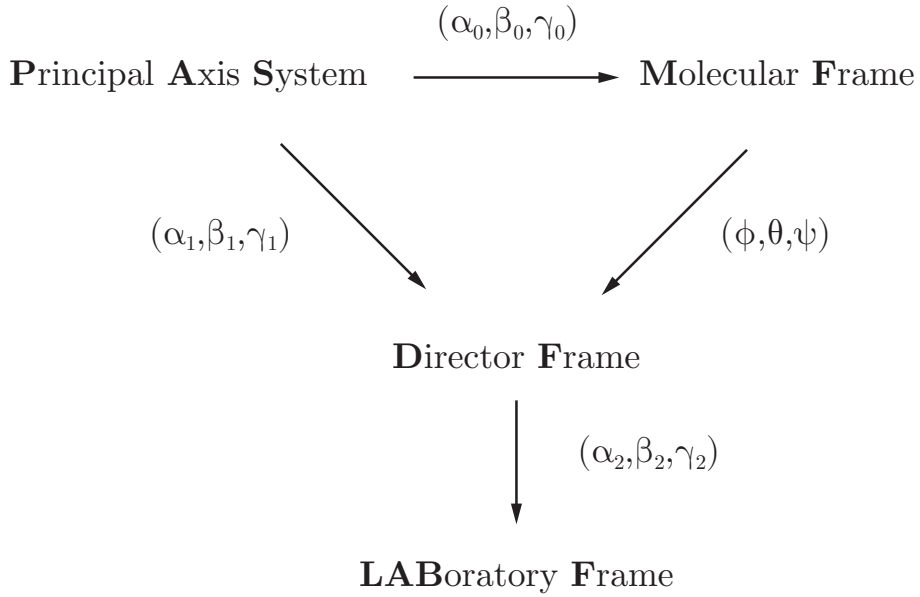


Figure 6.1: The notation of reference frames for the polarized Raman experiment.

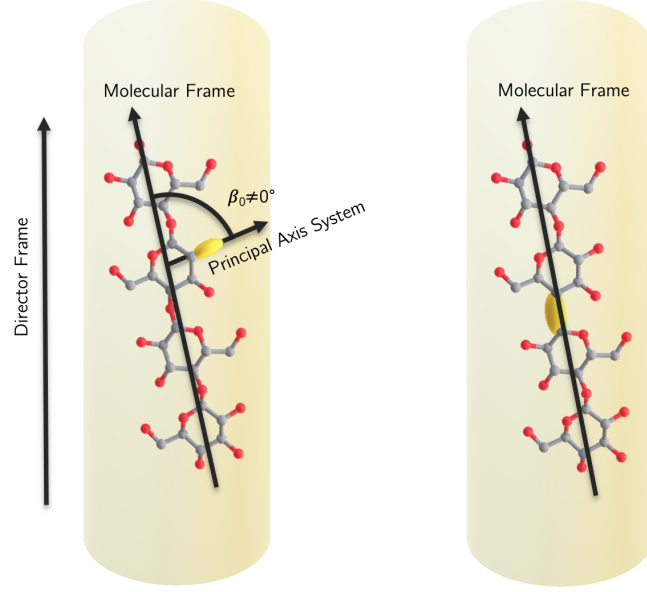


Figure 6.2: A visualization of the Raman tensor related reference frames in a cellulose fiber. (Left) A Raman vibrational mode that is not parallel to the Molecular Frame. (Right) A Raman vibrational mode with the Raman PAS tensor parallel to the Molecular Frame.

We find the relations:

$$\alpha^{\text{DF}} = \mathbf{R}(\alpha_1, \beta_1, \gamma_1) \alpha^{\text{PAS}} \mathbf{R}^{-1}(\alpha_1, \beta_1, \gamma_1) \quad (6.3)$$

$$\alpha^{\text{MF}} = \mathbf{R}(\alpha_0, \beta_0, \gamma_0) \alpha^{\text{PAS}} \mathbf{R}^{-1}(\alpha_0, \beta_0, \gamma_0) \quad (6.4)$$

$$\alpha^{\text{DF}} = \mathbf{R}(\phi, \theta, \psi) \alpha^{\text{MF}} \mathbf{R}^{-1}(\phi, \theta, \psi) \quad (6.5)$$

By inserting Equation (6.4) into Equation (6.5), we find the equality:

$$\mathbf{R}(\alpha_1, \beta_1, \gamma_1) = \mathbf{R}(\phi, \theta, \psi) \mathbf{R}(\alpha_0, \beta_0, \gamma_0) \quad (6.6)$$

The rotation formalism used in the seminal work by Bower[11] is an active, or forward, Z-Y-Z rotation. This means that we express the Raman tensor in the director frame by rotating the coordinate system from the PAS tensor by first γ , then β and finally α . The equivalent object rotation would be to rotate the Raman tensor from the DF to its position by first α , then β and finally γ rotation. Integrating over all molecular angles relative to the DF, we get:

$$I_0 \sum \alpha_{ij}^{\text{DF}} \alpha_{pq}^{\text{DF}} = I_0 N_0 \int_0^{2\pi} \int_0^\pi \int_0^{2\pi} f(\theta) \alpha_{ij}^{\text{DF}}(\alpha_1, \beta_1, \gamma_1) \alpha_{pq}^{\text{DF}}(\alpha_1, \beta_1, \gamma_1) \sin \theta \, d\phi \, d\theta \, d\psi \quad (6.7)$$

With α_{ij}^{DF} describing a direct Euler rotation from the PAS to the DF, such as:

$$\alpha_{ij}^{\text{DF}}(\alpha_1, \beta_1, \gamma_1) = \left[\mathbf{R}(\alpha_1, \beta_1, \gamma_1) \boldsymbol{\alpha}^{\text{PAS}} \mathbf{R}^{-1}(\alpha_1, \beta_1, \gamma_1) \right]_{ij} \quad (6.8)$$

By expressing $\boldsymbol{\alpha}^{\text{DF}}$ in terms of its equivalent rotation from Equation (6.6), we get:

$$\begin{aligned} I_0 \sum \alpha_{ij}^{\text{DF}} \alpha_{pq}^{\text{DF}} &= I_0 N_0 \int_0^{2\pi} \int_0^\pi \int_0^{2\pi} f(\theta) \\ &\left[\mathbf{R}(\phi, \theta, \psi) \mathbf{R}(\alpha_0, \beta_0, \gamma_0) \boldsymbol{\alpha}^{\text{PAS}} \mathbf{R}^{-1}(\alpha_0, \beta_0, \gamma_0) \mathbf{R}^{-1}(\phi, \theta, \psi) \right]_{ij} \\ &\left[\mathbf{R}(\phi, \theta, \psi) \mathbf{R}(\alpha_0, \beta_0, \gamma_0) \boldsymbol{\alpha}^{\text{PAS}} \mathbf{R}^{-1}(\alpha_0, \beta_0, \gamma_0) \mathbf{R}^{-1}(\phi, \theta, \psi) \right]_{pq} \\ &\sin \theta \, d\phi \, d\theta \, d\psi \end{aligned} \quad (6.9)$$

The angle α_0 coincides with molecular rotational symmetry for a sample with many semi crystalline molecular chain elements, as in a polymer, and can be chosen freely. In usual circumstances, it is convenient to set α_0 to 0. In contrast, ROSMAS is symmetric on γ_0 if the passive rotation formalism is used. The unknown Euler angles β_0 and γ_0 can be determined either from experimental observation or computational modelling. Finally, the fiber sample is rotated around the lab frame Y-axis, the direction of the incident light, such that the general expression for both the back scattering and right angle scattering can be expressed as:

$$\mathbf{I}(\beta_2) = I_0 \sum \left[\mathbf{R}_Y(\beta_2) \boldsymbol{\alpha}^{\text{DF}} \mathbf{R}_Y^{-1}(\beta_2) \right] \cdot \left[\mathbf{R}_Y(\beta_2) \boldsymbol{\alpha}^{\text{DF}} \mathbf{R}_Y^{-1}(\beta_2) \right] \quad (6.10)$$

From which all of the scattering geometries can be derived. The angle β_2 corresponds to the Y-rotation of the fiber in the $\mathbf{x}_1 - \mathbf{x}_3$ plane, with $\beta_2 = 0$ for a fiber in the \mathbf{x}_3 or Z-direction. For the three back scattering polarization configurations, corresponding to the matrix indices, Equations (6.11) through (6.15) are obtained.

$$I_{33}^{\text{BS}}(\beta_2) = I_{33}^{\text{RAS}^*}(\beta_2) = I_0 \sum \left(\alpha_{33}^{\text{DF}} \cos^2 \beta_2 - \alpha_{13}^{\text{DF}} \sin 2\beta_2 + \alpha_{11}^{\text{DF}} \sin^2 \beta_2 \right)^2 \quad (6.11)$$

$$I_{11}^{\text{BS}}(\beta_2) = I_0 \sum \left(\alpha_{11}^{\text{DF}} \cos^2 \beta_2 + \alpha_{13}^{\text{DF}} \sin 2\beta_2 + \alpha_{33}^{\text{DF}} \sin^2 \beta_2 \right)^2 \quad (6.12)$$

$$I_{13}^{\text{BS}}(\beta_2) = I_0 \sum \left(\alpha_{13}^{\text{DF}} \cos^2 \beta_2 + \frac{1}{2} \alpha_{33}^{\text{DF}} \sin 2\beta_2 - \frac{1}{2} \alpha_{11}^{\text{DF}} \sin 2\beta_2 - \alpha_{13}^{\text{DF}} \sin^2 \beta_2 \right)^2 \quad (6.13)$$

$$I_{23}^{\text{RAS}}(\beta_2) = I_0 \sum \left(\alpha_{23}^{\text{DF}} \cos \beta_2 - \alpha_{21}^{\text{DF}} \sin \beta_2 \right)^2 \quad (6.14)$$

$$I_{21}^{\text{RAS}}(\beta_2) = I_0 \sum \left(\alpha_{21}^{\text{DF}} \cos \beta_2 + \alpha_{23}^{\text{DF}} \sin \beta_2 \right)^2 \quad (6.15)$$

With the cylindrical symmetry of a fiber, there are the additional symmetry conditions:

$$\alpha_{11}^{\text{DF}} = \alpha_{22}^{\text{DF}} \quad (6.16)$$

$$\alpha_{23}^{\text{DF}} = \alpha_{13}^{\text{DF}} \quad (6.17)$$

BS and RAS refer to back scattering and right angle scattering experiments, respectively, as illustrated in Figure 6.3. The subscripts in $I_{ij}^{\text{BS}}(\beta)$ refer to the polarization of the analyzer (i) and of the incident light (j), respectively, as visualized in Figure 6.3 and 6.4. To obtain the expressions of Citra et al., the fiber is simply rotated with an X-rotation, and changing a possible error in the minus sign in Citra et al. Equation 12, Equation 14 and Equation 15.[59]

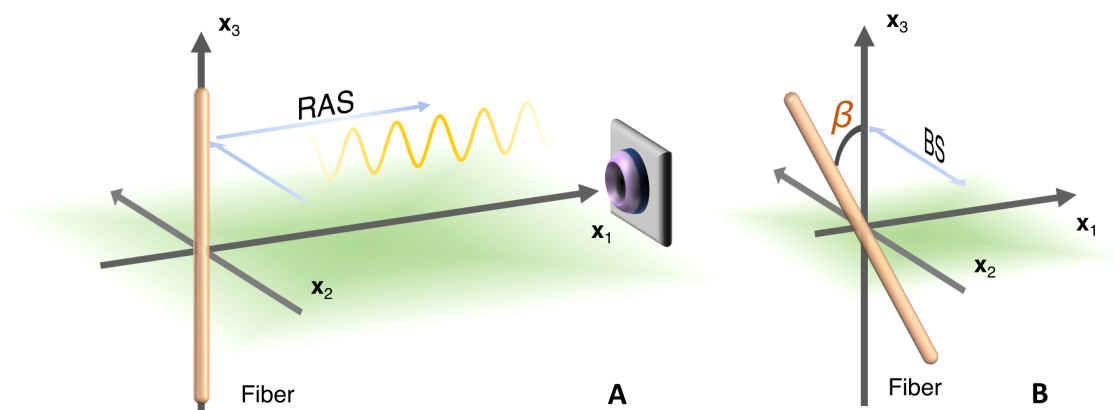


Figure 6.3: Schematic of the Right Angle Scattering (RAS) experiment (A) with the laser entering in the \mathbf{x}_2 direction and exiting in the direction of \mathbf{x}_1 . Back Scattering (BS) experiment (B) with the laser entering in the \mathbf{x}_2 direction and exiting at \mathbf{x}_2 . The fiber is positioned in the \mathbf{x}_1 - \mathbf{x}_3 plane with an angle β that is parallel to \mathbf{x}_3 when $\beta = 0$. Reprinted with permission from Svenningsson et al., *Macromolecules* 2019, 52, 3918-3924. Copyright 2019 American Chemical Society.

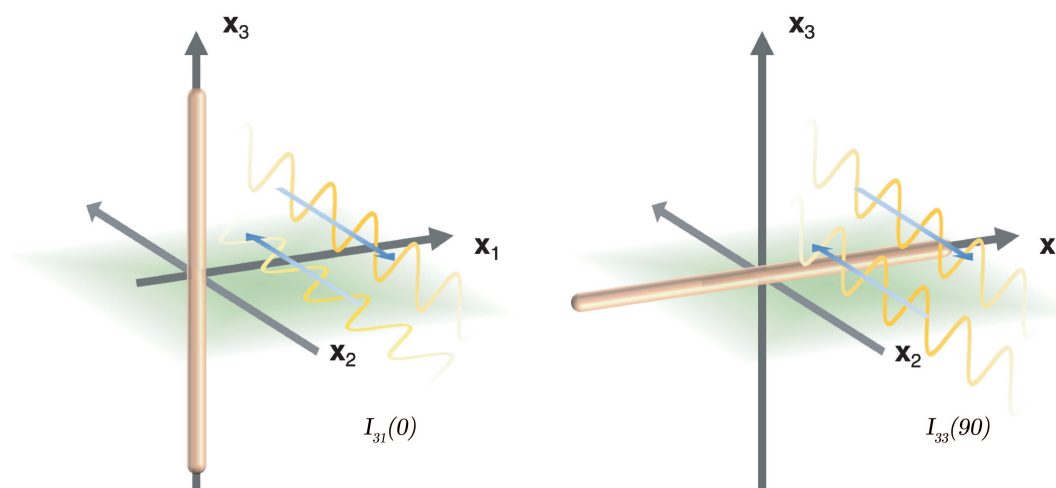


Figure 6.4: Schematic of the $I_{31}^{\text{BS}}(0)$ and $I_{33}^{\text{BS}}(90)$ configurations, with polarized laser in the \mathbf{x}_2 direction. Reprinted with permission from Svenningsson et al., *Macromolecules* 2019, 52, 3918-3924. Copyright 2019 American Chemical Society.

The resulting set of experiments can be used to calculate the molecular orientation

for an arbitrarily oriented Raman tensor in a polymeric fiber. When the molecular orientation is known, from for example WAXS or ROSMAS NMR, the equation can be a tool to determine the orientation of Raman active vibrations relative to the molecular frame. Preferably, experimental vibrational intensities can be experimentally collected for many scattering angles and fitted with the model by traditional methods or machine learning solutions. Calculating the Raman tensor orientation has been done before in crystals and in fibrillar materials, though those cases assume a perfect molecular orientation distributions.[80] The model presented in this chapter contains both the orientation distribution and the tensor Euler angles relative to the molecular frame with a material fiber symmetry.

To calculate Raman scattering intensity, the ODF can be approximated as a sum of weighted Legendre polynomials as discussed in Section 3, which have more advantages than only being the standard method to describe molecular orientation in fibers. The linear contributions of cosines enables us to solve the integral in Equation (6.1) analytically. When the Raman spectroscopy is put into an experimental context[60] the following sets of equations are valid if the Raman tensor in the PAS coincide with the MF:

$$\begin{aligned}
 I_{33}^{\text{BS}}(0) &= I_0 \sum (\alpha_{33}^{\text{DF}})^2 = \\
 & b \left[(3a_1^2 + 3a_2^2 + 3 + 2a_1a_2 + 2a_1 + 2a_2) / 15 - \right. \\
 & P_2 (3a_1^2 + 3a_2^2 - 6 + 2a_1a_2 - a_1 - a_2) / 21 + \\
 & \left. P_4 (3a_1^2 + 3a_2^2 + 8 + 2a_1a_2 - 8a_1 - 8a_2) / 35 \right] \quad (6.18)
 \end{aligned}$$

$$\begin{aligned}
 I_{33}^{\text{BS}}(90) &= I_{11}^{\text{BS}}(0) = I_0 \sum (\alpha_{22}^{\text{DF}})^2 = I_0 \sum (\alpha_{11}^{\text{DF}})^2 = \\
 & b \left[(3a_1^2 + 3a_2^2 + 3 + 2a_1a_2 + 2a_1 + 2a_2) / 15 + \right. \\
 & P_2 (3a_1^2 + 3a_2^2 - 6 + 2a_1a_2 - a_1 - a_2) / 21 + \\
 & \left. P_4 (3a_1^2 + 3a_2^2 - 6 + 2a_1a_2 - 8a_1 - 8a_2) / 280 \right] \quad (6.19)
 \end{aligned}$$

$$\begin{aligned}
 I_{31}^{\text{BS}}(0) &= I_{31}^{\text{BS}}(90) = I_{23}^{\text{RAS}}(0) = I_0 \sum (\alpha_{23}^{\text{DF}})^2 = I_0 \sum (\alpha_{31}^{\text{DF}})^2 = \\
 & b \left[(a_1^2 + a_2^2 + 1 - a_1a_2 - a_1 - a_2) / 15 - \right. \\
 & P_2 (a_1^2 + a_2^2 - 2 - 4a_1a_2 + 2a_1 + 2a_2) / 42 - \\
 & \left. P_4 (3a_1^2 + 3a_2^2 + 8 + 2a_1a_2 - 8a_1 - 8a_2) / 70 \right] \quad (6.20)
 \end{aligned}$$

$$\begin{aligned}
 I_{21}^{\text{RAS}}(0) &= I_0 \sum (\alpha_{21}^{\text{DF}})^2 = \\
 & b \left[(a_1^2 + a_2^2 + 1 - a_1a_2 - a_1 - a_2) / 15 + \right. \\
 & P_2 (a_1^2 + a_2^2 - 2 - 4a_1a_2 + 2a_1 + 2a_2) / 21 + \\
 & \left. P_4 (3a_1^2 + 3a_2^2 + 8 + 2a_1a_2 - 8a_1 - 8a_2) / 280 \right] \quad (6.21)
 \end{aligned}$$

$$\begin{aligned}
I_{31}^{\text{BS}}(45) = & \frac{1}{4}I_0 \sum (\alpha_{11}^{\text{DF}})^2 - \frac{1}{2}I_0 \sum \alpha_{11}^{\text{DF}} \alpha_{33}^{\text{DF}} + \frac{1}{4}I_0 \sum (\alpha_{33}^{\text{DF}})^2 = \\
& b \left[(a_1^2 + a_2^2 + 1 - a_1 a_2 - a_1 - a_2) / 15 - \right. \\
& P_2 (a_1^2 + a_2^2 - 2 - 4a_1 a_2 + 2a_1 + 2a_2) / 42 + \\
& \left. P_4 (3a_1^2 + 3a_2^2 + 8 + 2a_1 a_2 - 8a_1 - 8a_2) / 1120 \right] \quad (6.22)
\end{aligned}$$

Equations (6.18)-(6.21) are given as in Citra[59] and Equation (6.22) is derived by Yang [60]. In addition,

$$\begin{aligned}
b &= I_0 N_0 (\alpha_{33}^{\text{PAS}})^2 \\
a_1 &= \alpha_{11}^{\text{PAS}} / \alpha_{33}^{\text{PAS}} \\
a_2 &= \alpha_{22}^{\text{PAS}} / \alpha_{33}^{\text{PAS}}
\end{aligned}$$

where N_0 is the number of repeating molecular units in the volume excited by the laser and I_0 is the laser intensity. The variables α_{11}^{PAS} , α_{22}^{PAS} and α_{33}^{PAS} refers to the Raman tensor principal axis components.

By simultaneously solving Eqs (6.18)-(6.22) and choosing the physical solutions[58, 59, 81], the two order parameters, P_2 and P_4 , are obtained. Bower's model is only valid when the Raman tensor principal axis coincides with the molecular frame. **Paper II** investigates the 1096 cm^{-1} feature of regenerated cellulose. The 1096 cm^{-1} signal is known to correspond to the glycosidic COC bond[82], which has a strong vibration in the approximate direction of the cellulose unit chain. As a note, the method by Bower is often referred as the "complete method" when no approximations are made, while Yang et al.'s method [60] is referred to as the "complete (tilt) method".

6.2 The Wrapped Lorentzian Polarized Raman Spectroscopy Experiment

As reviewed in Chapter 3, plotting the limited number of Legendre contributions allows for negative probability densities. Only from reconstruction with the order parameters, a more realistic ODF is obtained. Still, an ODF has to be assumed.

My hypothesis is as follows: If the mathematical form of the ODF is known, it should be possible to reformulate Bower's polarized Raman experiment to reduce the number of necessary measurements.

The main methods to investigate the ODF directly are wide angle X-ray scattering, neutron diffraction and DECODER NMR. In **Paper I** and **Paper II** a wL function is shown to fit well with the azimuthal angle of the 002 reflection from X-ray scattering. The X-ray scattering pattern motivates a wL polarized Raman experiment, where the sum of Legendre polynomials is exchanged with the wL function. The benefit of doing so is to reduce the number of unique experiments to four. Particularly, it lets us remove the infrequently used RAS method. Consequently, the availability of the

technique is increased for more Raman spectroscopy setups. The only drawback of the wL method is that Equation (6.1) has to be solved numerically, either with some initial conditions for the Raman tensor eigenvalues and the Lorentzian scale factor λ , estimated from previous results or literature. Or the function can be solved for the entire estimated search space.

Chapter 7

X-Ray Scattering

X-ray crystallography has a long history with probably the most famous discovery being the DNA double helix contributions by Rosalind Franklin and Raymond Gosling, eventually earning Francis Crick, James Watson and Maurice Wilkins the Nobel Prize in 1962.[83] Light interacts with any grating, forcing a diffraction pattern, most easily observed when the wavelength is similar to the spaces in the grating. Wide angle X-ray scattering (WAXS) looks at inter molecular distances yielding patterns of the molecular structure. X-ray scattering was used to determine the crystallographic structure of cellulose II in 1975 by Kolpak[84]. Figure 7.1 displays a crystalline cellulose II structure using Krässig's[19] cellulose II crystal lattice notation with the cellulose chain in the b direction.

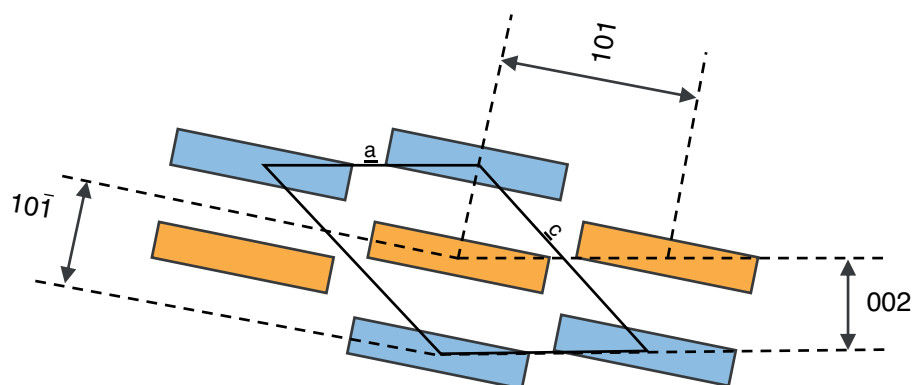


Figure 7.1: Reflections on the cellulose crystal lattice viewed along the chain with blue as parallel and orange as anti-parallel chains. Each rectangle represents an anhydroglucose cellulose unit.

Wide angle X-ray scattering is probably one of the most accessible methods to directly observe molecular orientation distributions in oriented polymers. Still, quantitative analysis has so far relied heavily on the users' preferred evaluation routines.[19] An automated curve fitting procedure of my own design handles the information of molecular orientation, background noise, and misalignment of the fiber in the sample holder. The orientation distribution was measured by extracting a thin strip of the 002 reflection in Figure 7.2a from the azimuthal angle 0° to 45° in order to prevent influence from the 021 reflection centered around 60° . The

extracted data is fitted with a wL function and a constant baseline, as in Figure 7.2b. Wanasekara used a Lorentzian function in their study of ionic liquid spun fibers, which in many cases are sufficient.[30] However, for low molecular orientation distributions, the ODF has to have periodic characteristics to fully accommodate the periodic molecular orientation information. The fitted curve can be used with Equation (3.6) to calculate the Legendre order parameters.

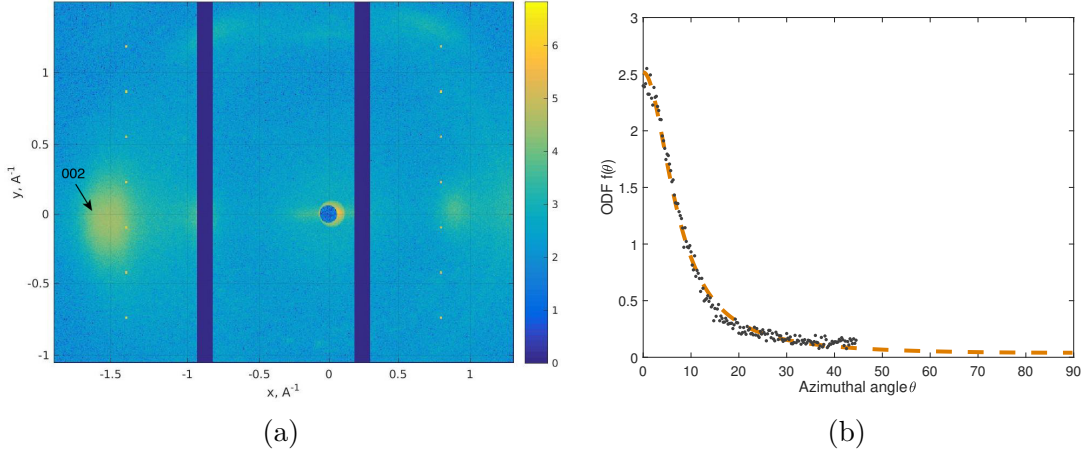


Figure 7.2: (a) 2D wide angle X-ray scattering log intensity plot of a 15 μm Lyocell fiber, with the fiber along the y-direction. (b) Wrapped Lorentzian azimuthal angle curve fitting (dashed) of the 002 WAXS reflection of a regenerated cellulose fiber (dots).

Figure 7.3 shows it is possible to fit a wL ODF to the regenerated cellulose signal from a cellulose-lignin composite fiber with different draw ratios. The study underpins the generality of this function for the regenerated cellulose fiber materials, of which the wL fits well with both neat and composite regenerated cellulose-lignin fibers. The function was also successfully implemented in **Paper I** and **Paper II**, replacing the Legendre polynomials with the wL function in the ROSMAS and polarized Raman spectroscopy experiments, respectively.

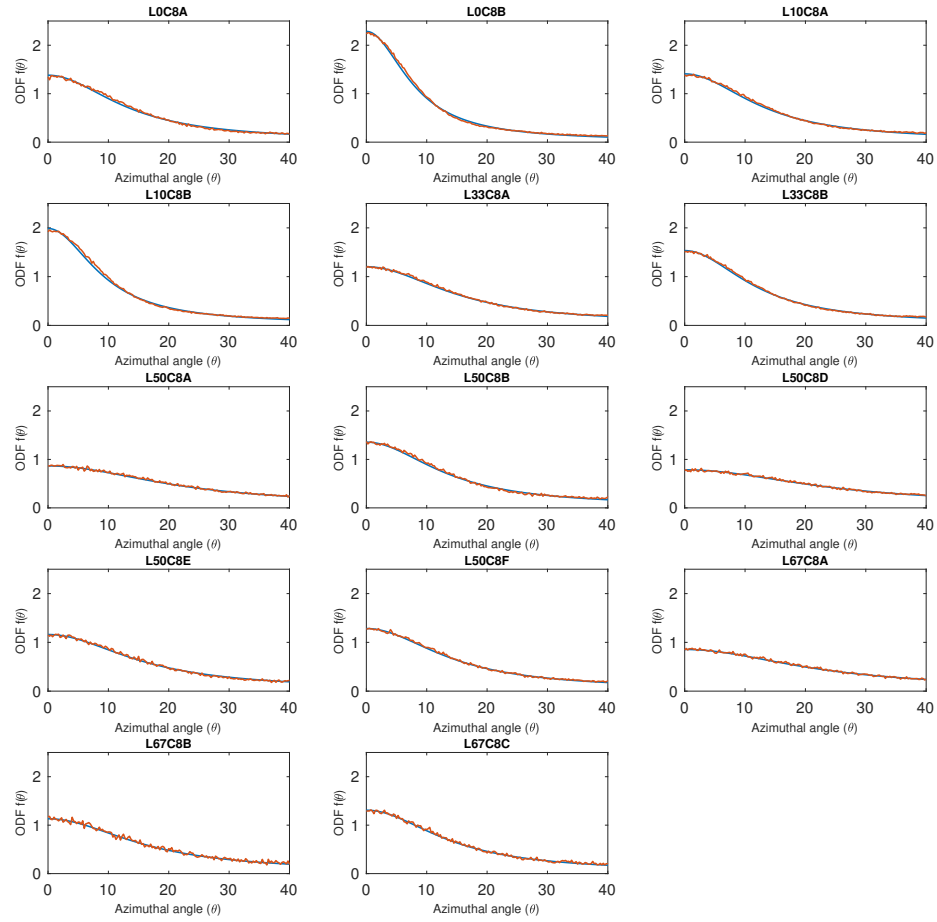


Figure 7.3: Wrapped Lorentzian azimuthal angle curve fittings of the 002 WAXS reflection of regenerated cellulose and lignin composite fibers.

Chapter 8

Crystallinity of Celluloses

Crystallinity in the context of cellulose is the fraction of polymeric material that express similar behaviour as crystals, compared to its non-crystalline parts. Crystalline and non-crystalline information of polymers can be separated with various techniques, such as solid-state NMR spectroscopy[33, 85, 86], Raman spectroscopy[87], and X-ray scattering[88]. The crystalline/non-crystalline separated information strongly depends on the polymer in question. Cellulose, being a stiff polymer may show little difference in chemical selectivity regarding many spectroscopic techniques. A flexible polymer, such as polyethylene can be differentiated more easily with a greater chemical perturbation in the kinks. In my work I consistently use the term non-crystalline for polymers. The commonly used corresponding term, amorphous, is often misused since it implies that the polymer is disorganized. With ROSMAS NMR, it can be demonstrated that non-crystalline cellulose also has significant molecular order. The crystalline and non-crystalline marks in Figure 8.1 are regarded as a simplification of many contributing factors to the signal separation but are often used to determine crystallinity in polymers.[85, 89] The C1 peak in cellulose also contains amorphous signals that can be separated by deconvolution. The two separate peak intensities in a CP-MAS polyethylene spectrum are strongly dependent on the cross-polarization coherence transfer, making it a weak method of quantitative analysis compared to direct polarization, without specific knowledge of the CP enhancement factors. The CP coherence transfer is more evenly distributed among the crystalline and non-crystalline regions in cellulose using correct CP settings.

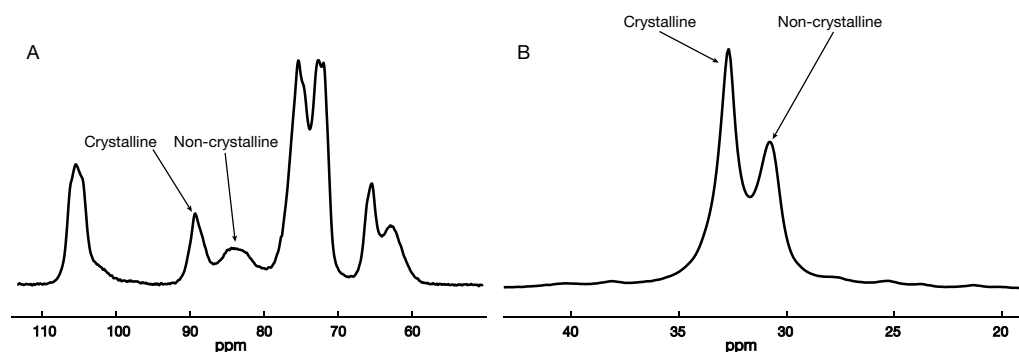


Figure 8.1: A: Solid-state NMR spectrum of native cellulose. B: Solid-state NMR spectrum of polyethylene.

Any one specific investigative method may have physical limitations in determining fractions of crystallinity. One such example is X-ray scattering, where light interacts with the spatial cavities between polymer chain segments. Regenerated cellulose typically has crystalline domains with typically ten nanometers in diameter and a few hundred nanometers in length[19, 90] and the fraction of surface to bulk crystalline cellulose may affect the perceived crystallinity.[88] Solid-state NMR spectroscopy offers an additional set of methods to measure crystallinity. Typical methods include C4 deconvolution of wet cellulose and simple integration of the C4 signal features. [33, 85, 86, 91] A novel method based on T_1 relaxation signal filtration is described in **Paper III**.

Crystallinity correlates well with mechanical and morphological properties.[28, 92] Permeability of gases and water steam in cellulose films is affected by crystalline packing.[20] The size of crystalline domains hampers chemical and biological reactions such as chemical hydrolysis into nanocrystalline cellulose and enzymatic degradation. [20, 32, 33, 90] Many more examples can be made, and therefore accurate measurements of crystallinity have an important role in cellulose and polymer science.

Chapter 9

Results and Discussion

9.1 Molecular Orientation from ROSMAS and Raman Spectroscopy

Molecular orientation distributions can be measured with many techniques, though quantitative aspects of the molecular orientation can be challenging to obtain. If we move into the realm of composites, partially modified and semi-crystalline materials, many techniques can struggle to disassociate the signal origin. Solid-state NMR spectroscopy is a powerful technique, which can separate molecular information well in one dimension, but also in high-dimensional spectra. In **Paper I** we investigate the ROSMAS technique as a quantitative solid-state NMR measurement technique for molecular orientation distributions. A combination of ROSMAS, X-ray scattering, and polarized Raman spectroscopy enables confident use of ROSMAS for quantitative measurements on cellulose and other polymers. The work in **Paper I** and **Paper II** was the first time these three techniques have ever been directly compared to measure molecular orientation. Not only were the results consistent, but it was also possible to single out a specific ODF, i.e. the wL function from WAXS and parse the ROSMAS and polarized Raman spectroscopy experiments with the same function while retaining orientation information in a neat regenerated cellulose fiber. A strong indication of the technique's solid theoretical foundation.

Figure 9.1 shows a calibration curve for cellulose II where the order parameter from the wL assumption is compared with the Legendre polynomials, where only a difference of $\Delta P_2 = 0.01$ is found for the upper limit of the regenerated cellulose order parameter. The results also suggest that a wL curve fit from WAXS should receive a minor calibration based on the data in Figure 9.1.

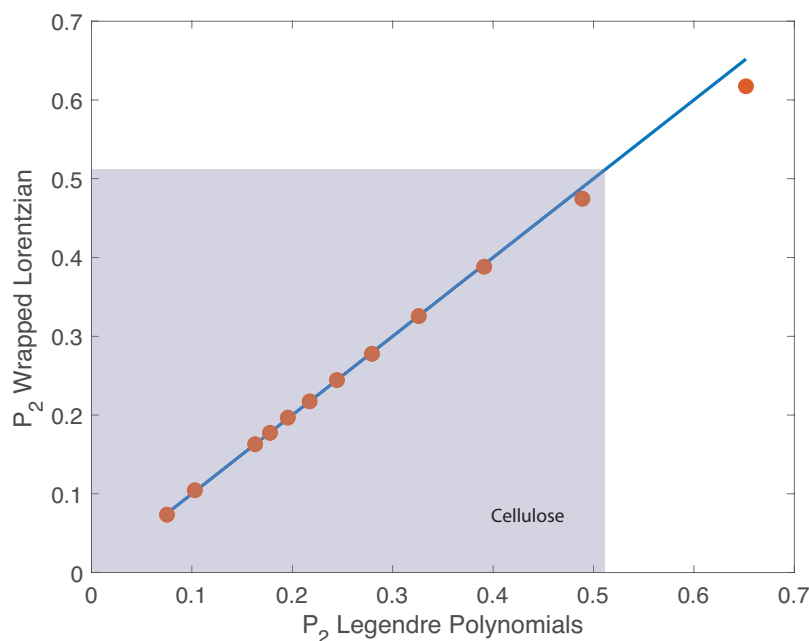


Figure 9.1: ROSMAS performance calculation of different molecular orientations using the wrapped Lorentzian orientation distribution function in comparison to the direct application of Legendre polynomials.

The ROSMAS technique is described in Chapter 4.2.1 and is used in conjuncture with a DFT study on the chemical shift anisotropy. The shift tensors for the two dissimilar polymer backbones in cellulose II, named the origin and center chain, are shown in Table 9.1.

Table 9.1: Chemical shift tensors of Cellulose II

Origin Chain Atom	δ_{11} (ppm)	δ_{22} (ppm)	δ_{33} (ppm)	α ($^{\circ}$)	β ($^{\circ}$)	γ ($^{\circ}$)
C1	122.21	108.42	90.96	211.17	28.30	75.01
C2	98.21	69.91	50.58	272.12	78.70	177.02
C3	87.18	78.60	54.71	56.60	52.41	37.19
C4	110.63	102.25	50.22	180.82	31.47	136.47
C5	98.46	82.42	44.12	194.01	26.96	56.87
C6	90.69	69.61	27.20	52.19	52.31	24.62
Center Chain Atom	δ_{11} (ppm)	δ_{22} (ppm)	δ_{33} (ppm)	α ($^{\circ}$)	β ($^{\circ}$)	γ ($^{\circ}$)
C1	123.80	105.77	85.72	92.69	36.89	122.45
C2	96.98	70.65	56.78	54.71	87.25	3.41
C3	90.62	74.13	65.66	279.73	60.74	143.42
C4	105.52	100.86	60.33	147.77	32.90	31.88
C5	96.99	80.05	38.97	128.59	29.27	130.15
C6	96.35	66.16	27.10	266.99	43.87	150.73

Using the ROSMAS NMR pulse sequence, the CSA is probed on the C1 carbon in the cellulose chain, which forms a part of the glycosidic COC bond between two saccharides. A deconvolution of the C1 contribution in the ROSMAS spectra was used to determine the crystalline integrals[91] as in Figure 9.2. The deconvolution implies conditions of both crystalline contributions having the same or similar orientation distribution.

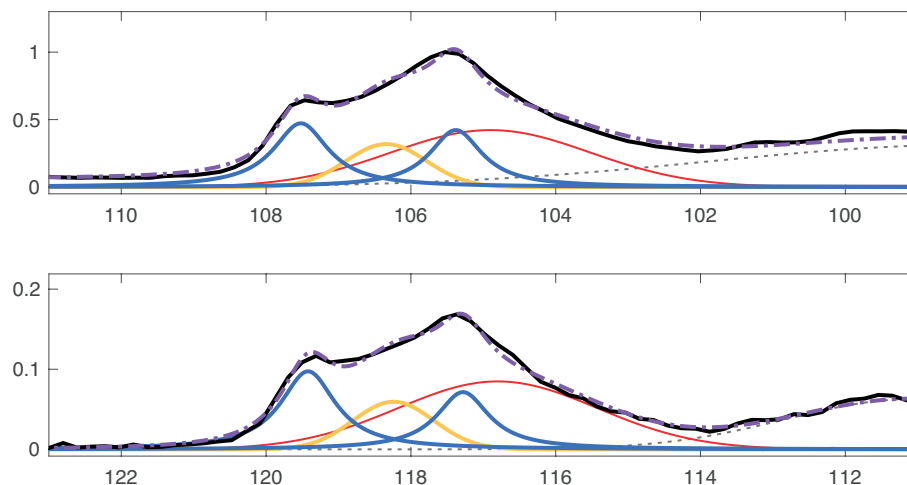


Figure 9.2: ROSMAS NMR spectra of oriented cellulose fibers (black) deconvoluted with crystalline (blue Lorentzian), surface moieties (orange Gaussian), amorphous (red Gaussian) signal and a base line (not shown). A Gaussian correction (gray dotted) is added for corrections from C4 sideband interference. The resulting deconvolution (purple dot-dashed) is shown with the base line. $M = 0$ (top) and $M = 1$ bottom.

The intensities for deconvolution were then used together with an analytical model of the ROSMAS spectra to determine the order parameter P_2 . The calculated spectra were based on two models: (1) The chemical shielding tensor as given by our DFT study and (2) a stretched fiber model where the glycosidic COC bond is approximated as parallel with the molecular frame. Model (2) was used successfully in **Paper II** to correlate polarized Raman spectroscopy with WAXS measurements. In addition, a peak height intensity based model is suggested, which can be used to determine the order parameter with a smaller error compared to deconvolution, thus reducing the total experimental time and removing a non-trivial deconvolution procedure.

The results in Table 9.2 in conjunction with **Paper II** suggests that the stretched fiber model better approximates the orientation distribution, consequentially implying that the idea of the cellulose II crystalline structure is different when mechanically processed. The study also suggests that the non-crystalline orientation distribution is the same as the crystalline molecular orientation as a result of the similar C1 line shape in $M = 0$ and $M = 1$, shown in Figure 9.2, in combination with the CSA tensor being parallel to the molecular frame. The conclusion is further motivated by the polarized Raman spectroscopy study that studies a vibration originating from both crystalline and non-crystalline signals. The wL ODF was also successfully

implemented to ROSMAS molecular orientation distribution analysis by exchanging the Legendre polynomials with wL ODF.

Table 9.2: Order parameters calculated from the ROSMAS experiments on a fiber bundle by deconvolution and peak height intensity along with X-ray scattering on a bundle of Lyocell fibers.

	$\langle P_2 \rangle$	$\langle P_2 \rangle_{\text{err}}$
ROSMAS - relaxed fiber model - deconvolution	0.77	0.12
ROSMAS - stretched fiber model - deconvolution	0.42	0.12
ROSMAS - stretched fiber model - peak height	0.45	0.02
wL ROSMAS - stretched fiber model - peak height	0.44	0.01
Wide angle X-ray scattering (bundled fibers)	0.46	0.02
Wide angle X-ray scattering (single fiber)	0.48	0.03
wL Polarized Raman spectroscopy (single fiber)	0.50	0.03

The theory behind the polarized Raman spectroscopy experiment is fully described in Chapter 6. The order parameters are measured by applying the complete polarized Raman experiment and a new wL ODF based experiment. The 1096 cm^{-1} band that has previously been assigned to the glycosidic COC bond and therefore analyzed to determine molecular orientation.[30, 82] The 1096 cm^{-1} Raman band is assumed to contain a strong Raman vibration in the molecular chain direction. Polarized Raman spectra at different angles can confirm that the strongest vibration occurs when polarization is parallel with a highly ordered fiber.

The "complete" polarized Raman experiment is limited in that it requires the very specific RAS experiment, not commonly available for many Raman spectrometers. To alleviate the inconvenience of RAS, the ODF shape is recognized WAXS to be well approximated by the wL ODF. When the sum of Legendre polynomials are exchanged with the wL function, the polarized Raman experiment is only dependent on one parameter, therefore RAS experiments can be removed to accommodate the lower amount of degrees of freedom. The Raman tensor principal axis components were calculated to $\alpha_{11} = -0.098$, $\alpha_{22} = 0.172$ and $\alpha_{33} = 0.458$ for the 785 nm wL experiment. The 1096 cm^{-1} Raman mode is likely to contain both crystalline and non-crystalline cellulose, which could affect how orientation should be interpreted. However, as mentioned above, no or negligible differences in orientation for these two phases in this specific sample were found using ROSMAS solid-state NMR spectroscopy.[17]

A few researchers have tried to implement models to remove the RAS measurement. These include: cylindrically symmetric Raman tensors, complementary depolarization measurements, and assumption of a most probable ODF. Each of these techniques have some flaws that can be refuted. When cylindrical symmetric tensor is implied, then $P_2 = 0.42$ and $\alpha_{11} = \alpha_{22} = 0.038$ and $\alpha_{33} = 0.424$. Since neither the tensors nor the order parameter agrees with our results, therefore it can be concluded that the cylindrical symmetric tensors are a poor approximation for regenerated cellulose

fibers. For materials where cylindrical symmetry can be applied, it is possible to remove an additional measurement, such as $I_{31}(45)$, by combining it with the wL ODF method.

In the publication of Richard-Lacroix and Pellerin[63] the most probable function is used to predict P_4 from P_2 . However, this method underestimates P_4 when compared to our WAXS study ($P_2 = 0.48 \rightarrow P_4 = 0.15$), which sequentially leads to a few unlikely solutions when their P_4 prediction is applied as a condition to remove RAS from the complete (tilt) method. The non-complex solution pairs are then: $P_2 = 0.15$ with $P_4 = 0.01$ and $P_2 = 0.72$ with $P_4 = 0.37$. The most probable approximation is therefore not compatible with external evidence. In addition, Richard-Lacroix and Pellerin constructed their model on fiber symmetry while spuriously applying them to films. An example of bi-axial distributions was demonstrated by Chmelka et al., using DECODER NMR spectroscopy.[13]

Figure 9.3 shows the curve fitting of the $I_{33}(0)$ 514 nm and 785 nm measurements. Figure 9.4 shows the remaining spectra for the 785 nm WL measurements.

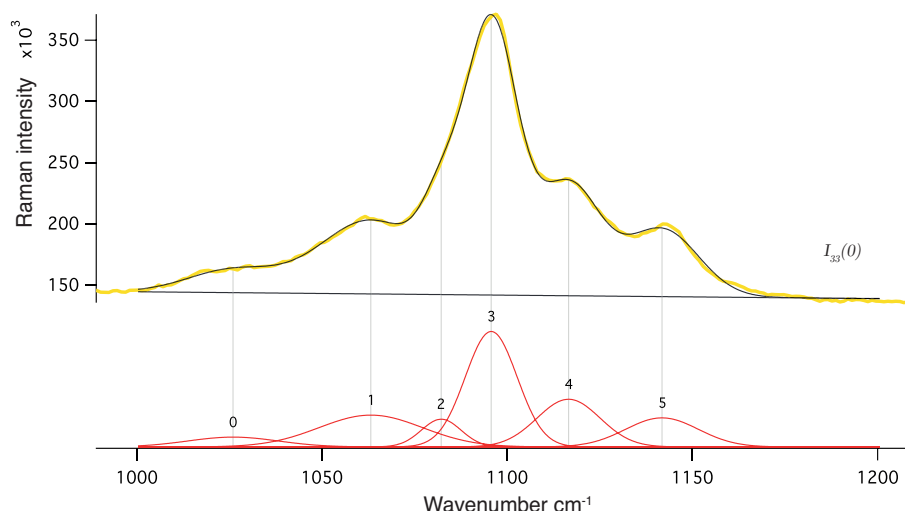


Figure 9.3: Peak fitting of the 1100 cm^{-1} region with laser polarization, analyzer filter and fiber in parallel for Tencell fiber Raman spectra ($I_{33}(0)$). *Reprinted with permission from Svenningsson et al., Macromolecules 2019, 52, 3918-3924. Copyright 2019 American Chemical Society.*

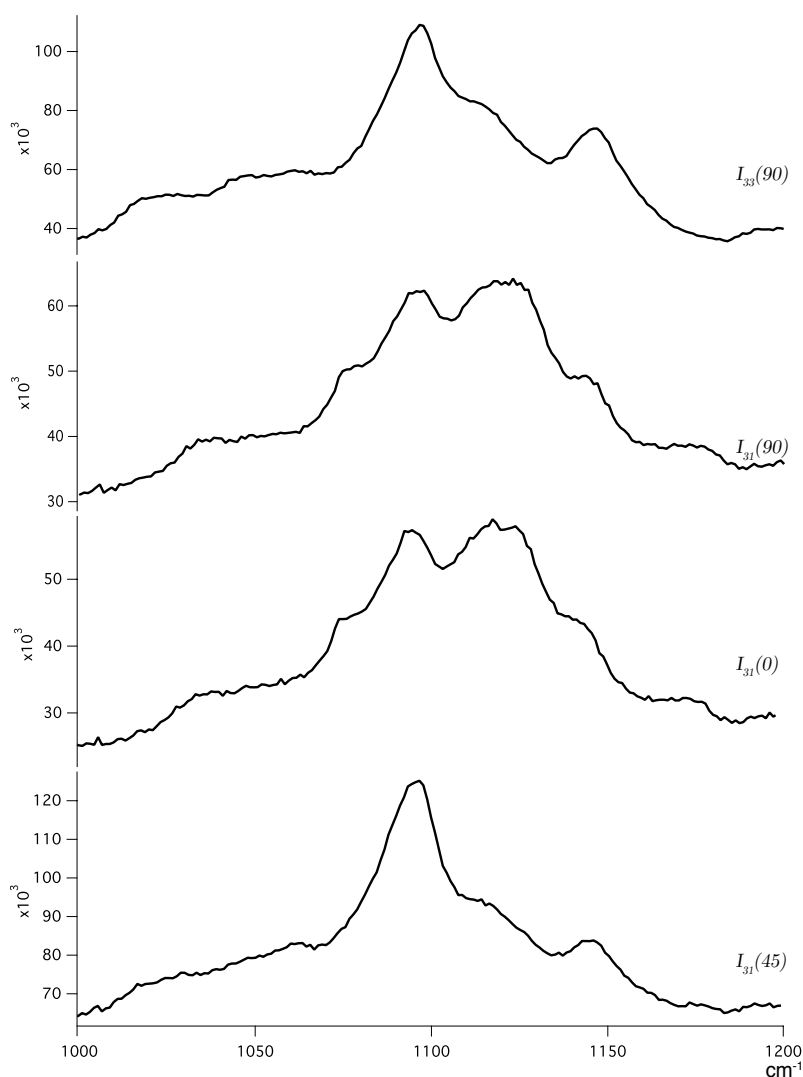


Figure 9.4: Tencell fiber Raman spectra of the 1000-1200 cm^{-1} region for the $I_{33}(90)$, $I_{31}(90)$, $I_{31}(0)$ and $I_{31}(45)$ configuration using the 785 nm laser. Reprinted with permission from Svenningsson et al., *Macromolecules* 2019, 52, 3918-3924. Copyright 2019 American Chemical Society.

Both **Paper I** and **Paper II** investigate the molecular orientation of Lyocell fibers from WAXS. The proceeding are described in Chapter 7 and will not be further discussed here. In Figure 9.5a we see a wL function fitted with the azimuthal 002 WAXS reflection. For correctness and intuition we reconstruct several ODFs to compare with the wL ODF which reflects the WAXS measurement. Figure 9.5b shows different ODFs reconstructed from the order parameters of a Lyocell fiber. Historically the ODF modelling has been done with little insight of choosing a correct model function[58, 61] but is now included here.

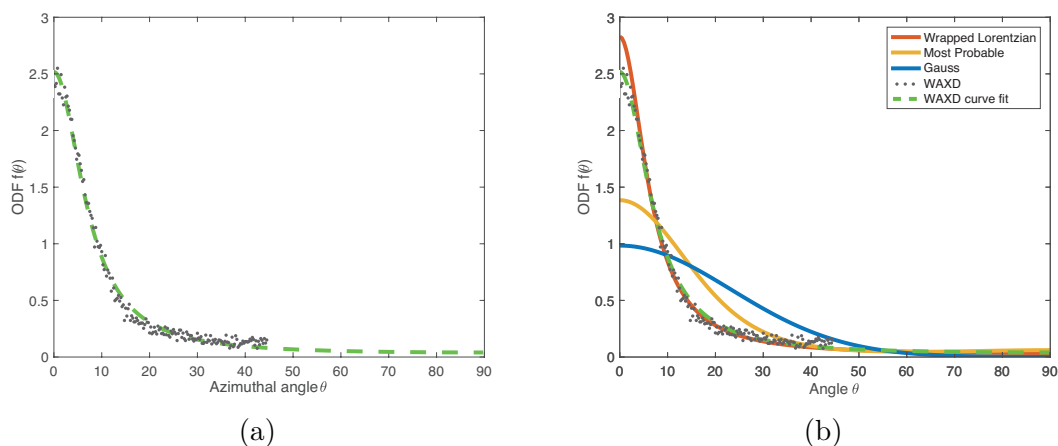


Figure 9.5: (a) Wrapped Lorentzian azimuthal angle curve fitting (dashed) of the 002 WAXS reflection (dots). *Reprinted with permission from Svenningsson et al., Macromolecules 2019, 52, 3918-3924. Copyright 2019 American Chemical Society.* (b) WAXS data with order parameters $P_2 = 0.48$ and $P_4 = 0.29$ from Figure 9.5a displayed alongside ODF reconstruction using $P_2 = 0.50$ and $P_4 = 0.31$, experimentally received using the complete (tilt) method with a regenerated cellulose fiber. *Reprinted with permission from Svenningsson et al., Macromolecules 2019, 52, 3918-3924. Copyright 2019 American Chemical Society.*

The work in **Paper II** also shows that it is not possible to remove RAS if Legendre polynomials are expressed with P_2 only. The reason being, the two equations for $I_{31}^{P_2}(45)$ and $I_{31}^{P_2}(0)$ become equal when solving Equation (6.1).

$$I_{31}^{P_2}(45) = I_{31}^{P_2}(0) = I_0 \left[14\alpha_1^2 + 14\alpha_2^2 + 14\alpha_3^2 - 14\alpha_1\alpha_2 - 14\alpha_1\alpha_3 - 14\alpha_2\alpha_3 + P_2 \left(-5\alpha_1^2 - 5\alpha_2^2 + 10\alpha_3^2 + 20\alpha_1\alpha_2 - 10\alpha_1\alpha_3 - 10\alpha_2\alpha_3 \right) \right] / 105 \quad (9.1)$$

As a complement, the Matlab scripts for both Bower's polarized Raman and wL polarized Raman experiments are provided:

github.com/LeoSvenningsson/Raman-ODF.

The ROSMAS calculations are available at:

github.com/LeoSvenningsson/ROSMAS.

9.2 Crystallinity Filtered NMR Spectroscopy

Solid-state NMR spectroscopy is a well known technique to measure crystallinity in cellulose. The most common NMR based method is to analyze the separated C4 peaks, as done in Chapter 8.[33, 86] The method suggested in **Paper III** exploits the different T_1 relaxation times of crystalline and non-crystalline cellulose, which can have over an order of magnitude in difference. The work in **Paper III** investigates the crucial properties of cross-polarization enhancement and T_1 relaxation to measure crystallinity from inversion recovery and saturation recovery experiments. The new signal filtering technique from **Paper III** has a potential use in relation to ROSMAS. It can be necessary to determine the fractions of crystalline and non-crystalline components, which may have different orientation distributions. ROSMAS allows for additional pulse sequences to be directly included with rotor synchronization. Therefore, it is possible to design a ROSMAS experiments with amorphous filtering included.

Equation (9.2) gives the expected relaxation time from a inversion recovery experiment of non-crystalline cellulose to reach $\langle \mathbf{I}_z \rangle = 0$. The calculated non-crystalline cellulose filtration time for MCC C1 signal can be calculated to $t_r = 15.29$ seconds from values obtained from **Paper III**.

$$\frac{1}{1 + e_{CP}} = \exp\{-t_r/T_1\} \quad (9.2)$$

A combined ROSMAS and inversion recovery experiment is shown in Figure 9.6. When t_r is set to negate the non-crystalline cellulose signal, we obtain a pure crystalline signal. This pulse sequence is however significantly longer than the typical cross-polarization experiment, from around a total of 3 seconds per cycle (ROSMAS) to 18 seconds (inv-rec ROSMAS) for cellulose. A significant cost, but a cost that could be be payed for difficult materials with overlapping moieties. The synchronization is applied right before the detection pulse to maintain the spatial encoding over the long pulse sequence. This makes the filtering time t_r variable in length, but the synchronization time t_1 is much smaller (10^{-4}) than the filtering time t_r and can therefore be ignored. Another method that has been explored in synthetic polymers is the spin-lattice relaxation in the rotating frame ^{13}C ($T_{1\rho}$) signal filtration. However, attempts to implement a spin-lattice relaxation sequence to filter cellulose moieties where unsuccessful.

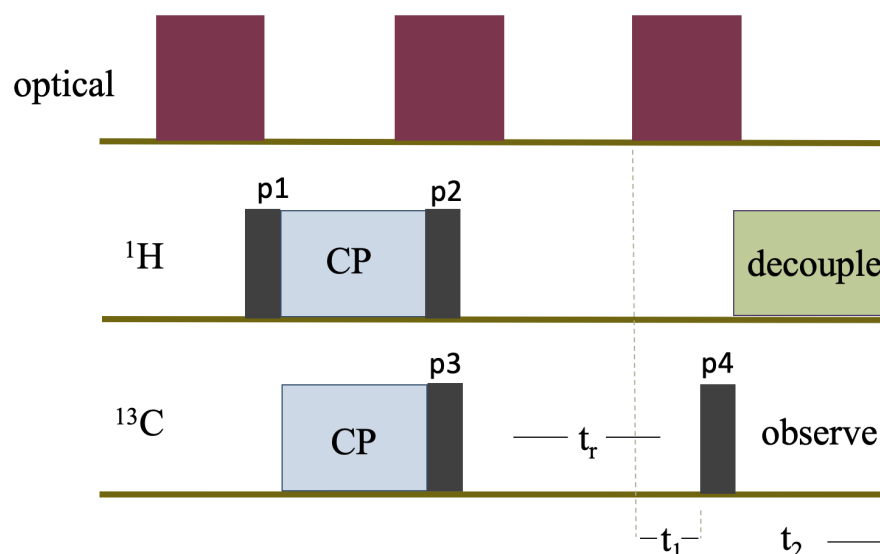


Figure 9.6: The ROSMAS pulse sequence combined with a inversion-recovery for non-crystalline (mobile) cellulose. The rf pulse p1 is a 90° ^1H excitation pulse while p2 is a 90° ^1H flip-back. For ^{13}C , p3 is a 90° rf pulse that inverts the ^{13}C magnetization after the CP transfer while p4 are 90° to flip the signal to the x-y plane to record the signal. The optical tachometer signal controls the starting position of the rotor.

9.3 Disassociated Molecular Orientation in Cellulose-Lignin Composites

Possibly the greatest benefit of the ROSMAS NMR method is its ability to separate information from composite materials. Curiously, this feature was never explored by the authors who first developed ROSMAS and sequential researchers who accrued on their work. The filtering was always in place since the adhesive used to collect the fibers in the rotor already makes the sample a composite. For the first time, this useful feature of the ROSMAS method is applied to a cellulose-lignin carbon fiber precursor. Lignin is typically a large branched biopolymer with little long range structure. The lignin structure is also largely dependent on the source and the extraction method. Lignin can be used as a cheap carbon source for carbon fibers, but a great carbon fiber is produced when the precursor polymer is oriented. The scientific question concerns whether the stretched lignin in the composite fiber is molecularly ordered. A main component of lignin is variants of aromatic structures. These aromatic structures are perfect candidates for ROSMAS analysis, due to their inherent relatively large CSA. Aromatic CSA span ($\sigma_{11} - \sigma_{33}$) are commonly around 150-200 ppm compared to the cellulose II C1 CSA span of 30-40 ppm. A large CSA will increase the signal sensitivity of the ROSMAS experiment. Figure 9.7 shows a photograph of regenerated cellulose-lignin composite fibers with clearly darker fibers for samples with high lignin content.



Figure 9.7: Photograph of three cellulose-lignin fibers. Top: 67, Mid: 33, Bot: 10 wt% lignin.

All fiber samples that were measured with ROSMAS, including measurements with a 4 kHz rotation rate not published in **Paper IV**, revealed completely disordered aromatic lignin. Figure 9.8 shows ROSMAS spectra of cellulose-lignin composite fibers. The signal in $M \neq 0$ contains only cellulose signal for all samples and trace amounts of oriented polystyrene are seen in the samples in Figure 9.8b. The absence of lignin signal in $M \neq 0$ tells us that the softwood kraft lignin, extracted with the LignoBoost method, is completely disordered. There are some oriented lignin signals in $M = \pm 2$ in the 25-60 ppm region. Orientation signal in only $M = \pm 2$ can appear if the sample DF-axis is perpendicular to the rotor axis. Such a system can only exist if smaller molecules, or flexible side chains are oriented due to rotational forces. Therefore, we do not attribute these signals as oriented lignin.

The molecular orientation of the fibers, which is derived from wood products, is compared to native wood from European spruce. The rotation rate for the wood sample is higher, at 4 kHz, to increase the aromatic signals found in lignin. Four signals from oriented lignin are observed around 125-190 ppm in $M = -1$ in a spruce solid wood sample, in addition to the oriented cellulose in Figure 9.9. Atalla and Agarwal first discovered oriented lignin near cell walls using polarized Raman spectroscopy.[93] The ROSMAS study seems to confirm that some oriented aromatics of lignin in wood do exist. The ROSMAS NMR studies suggest that the oriented lignin seen in wood is not regained in a regenerated composite fiber from the same, although intensely processed, raw materials. For example, LignoBoost extracted lignin is known to be different from native lignin. Kang et al. published recent findings in Nature Communications, which showed that lignin is bound to xylans rather than to the cellulose itself in a cellulose-xylan-lignin system.[94] Oriented lignin could be formed from the cellulose-xylan-lignin bridge, with the cellulose and hemicellulose acting as a scaffold. The ROSMAS study can not currently investigate a cellulose-xylan-lignin model since the relative amounts of xylan in dissolving pulp is much lower compared to wood. The xylan to cellulose ratio in dissolving pulp, which is used in the cellulose-lignin fibers, is 36% of the xylan to cellulose ratio of the less pure softwood kraft paper grade pulp[40]. For the sake of the discussion, if a

cellulose-xylan-lignin bridge is the key to oriented lignin, then one could possibly tailor the carbon fiber precursor manufacturing to reestablish the cellulose-xylan-lignin scaffold. The choice of wood source could impact the fractional contents xylan and other hemicelluloses, as well as differences in lignin itself, to increase the orientation of the lignin in a composite fiber.

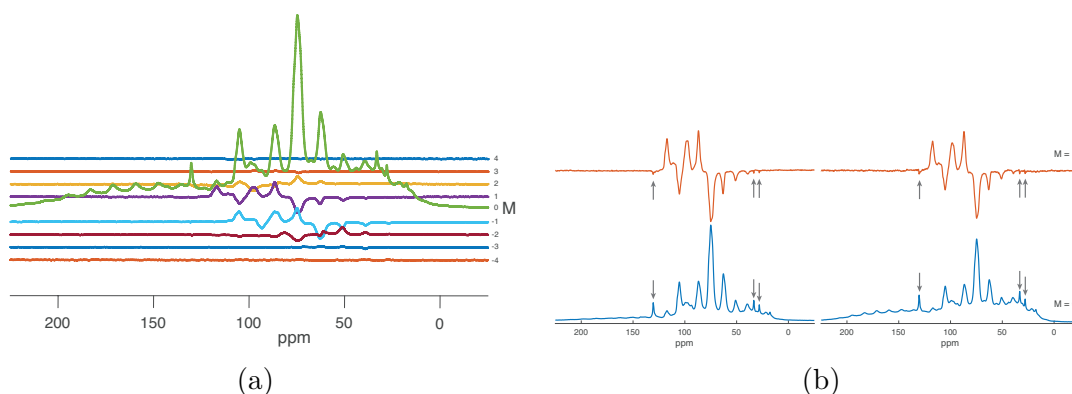


Figure 9.8: (a) ROSMAS NMR spectrum of regenerated cellulose and lignin composite fibers produced with 50 wt% lignin and draw ratio 2. (b) ROSMAS NMR spectra of regenerated cellulose and lignin composite fibers with draw ratio 6, produced with 10 wt% (left) 50 wt% (right). Arrows mark trace amounts oriented polystyrene, only seen in these two samples.

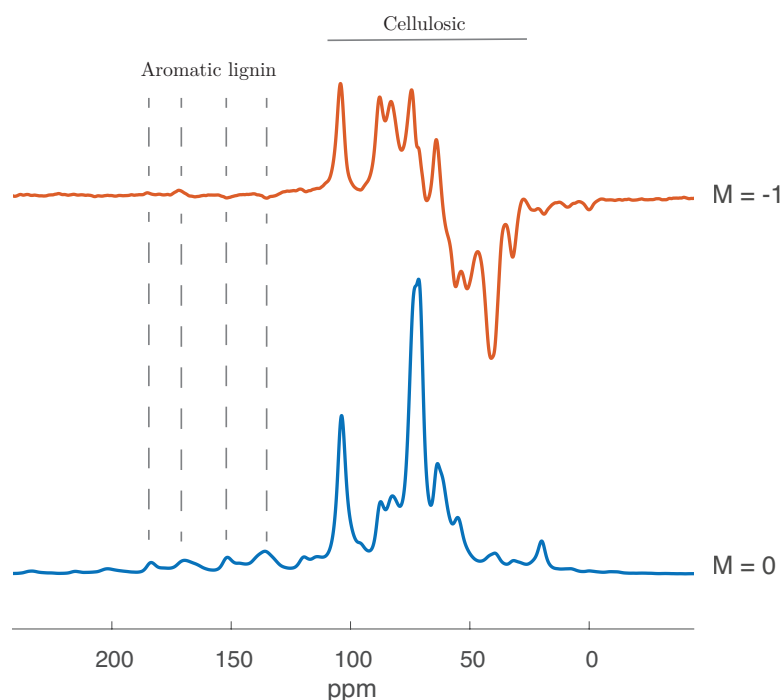


Figure 9.9: ROSMAS NMR spectra of a European spruce oriented wood sample, cut at 45° from the grain direction. Rotation rate at 4 kHz. Oriented aromatic lignin seen in the 125-190 ppm region.

Table 9.3 shows molecular orientation in the form of P_2 order parameter from WAXS and ROSMAS with regard to lignin content, draw ratio, and dope solution temperature. Trends show decreasing orientation with increase in lignin, and also an increase in orientation with increasing draw ratio. The molecular orientation results also suggest that the crystalline cellulose is ordered at low stretching, and the non-crystalline cellulose requires additional stretching to be maximally ordered.

Table 9.3: Molecular orientation data from birefringence (Δn) WAXS (P_2), and ROSMAS NMR (P_2) from fibers with varying lignin ratio, draw ratio and solution temperature.

Sample	LR	DR	°C	Δn	WAXS P_2	NMR P_2
L0A	0%	2	40	0.042 ± 0.003	0.37 ± 0.01	0.45 ± 0.01
L0B	0%	6	40	0.042 ± 0.005	0.46 ± 0.01	-
L10A	10%	2	40	0.038 ± 0.003	0.37 ± 0.01	-
L10B	10%	6	40	0.038 ± 0.004	0.44 ± 0.01	0.43 ± 0.02
L33A	33%	2	40	0.028 ± 0.003	0.34 ± 0.01	-
L33B	33%	6	40	0.032 ± 0.003	0.39 ± 0.01	-
L50A	50%	2	40	0.020 ± 0.003	0.26 ± 0.01	-
L50B	50%	6	40	0.023 ± 0.002	0.36 ± 0.01	-
L50D	50%	2	70	0.018 ± 0.002	0.24 ± 0.01	0.35 ± 0.02
L50E	50%	6	70	0.020 ± 0.001	0.33 ± 0.01	0.41 ± 0.02
L50F	50%	10	70	0.021 ± 0.003	0.35 ± 0.01	0.41 ± 0.03
L67A	67%	2	70	0.0129 ± 0.0003	0.26 ± 0.01	-
L67B	67%	6	70	0.0149 ± 0.0004	0.33 ± 0.02	0.39 ± 0.05
L67C	67%	10	70	0.016 ± 0.001	0.36 ± 0.01	-

A P_2 order parameter can in theory be calculated for birefringence, however it is challenging to correctly determine the required maximum birefringence for every new lignin blend,[14] therefore only the birefringence values are shown in Table 9.3. The birefringence in cellulose-lignin composite fibers is shown in Figure 9.10 to be strongly dependent on the lignin content. The strong dependence of composite mixture without any way to separate the signal makes birefringence inconvenient for quantitative composite analysis. The birefringence measurements are very fast and can be used to measure statistical differences in fibers from one batch as done in **Paper II**.

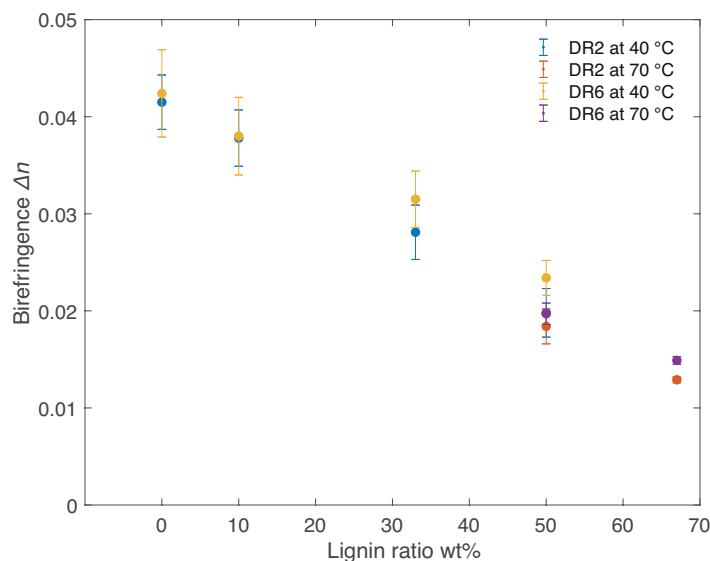


Figure 9.10: Birefringence of cellulose-lignin fibers as a function of lignin content.

9.4 Backbone and Side Chain Orientation Poly(3-hexylthiophene) Fibers

The quantitative ROSMAS experiments require rigorously accurate measurements of the CSA principal axis components and its Euler angles with respect to the molecular frame. In this work the CSA principal axis components and its Euler angles, in addition to the molecular orientation of the backbone and side chain, are determined for "crystalline"/non-crystalline moieties of poly(3-hexylthiophene) (P3HT). The CSA principal axis components was determined using Herzfeld-Berger modelling of spinning side bands from cut and disordered (P3HT) fibers. The Euler angles were determined from the ROSMAS method on oriented fibers by a minimizing function of Equation (5.10), setting the order parameters and Euler angles as free parameters. The CSA and orientation with respect to the molecular frame are given in Table 9.4 with a molecular representation of the CSA in the molecular frame given in Figure 9.11. The C7 and C7* signals were attributed to the crystalline and non-crystalline forms of P3HT, which determines its unique material properties as a conductor of electricity after doping. The electrical conductivity is then strongly related to the molecular orientation, which motivates this work.

Table 9.4: The chemical shift anisotropy, Euler angles with respect to the molecular frame and Order parameters of the poly(3-hexylthiophene) backbone carbons.

	δ_{11}	δ_{22}	δ_{33}	α_0	β_0	γ_0	P_2
C7	215 ± 2	151 ± 1	42 ± 2	$38^\circ \pm 1^\circ$	$84^\circ \pm 1^\circ$	-	0.87 ± 0.03
C7*	199 ± 1	166 ± 1	52 ± 1	$37^\circ \pm 1^\circ$	$90^\circ \pm 10^\circ$	-	0.42 ± 0.02
C8+C8*	193 ± 3	129 ± 3	56 ± 3	$40^\circ \pm 3^\circ$	$90^\circ \pm 18^\circ$	-	0.58 ± 0.15
C9	192 ± 1	138 ± 2	63 ± 2	$29^\circ \pm 1^\circ$	$90^\circ \pm 20^\circ$	-	$0.48 + 0.12 - 0.01$
C10	205 ± 1	139 ± 1	55 ± 1	$0^\circ \pm 25^\circ$	$90^\circ \pm 20^\circ$	-	$0.36 + 0.3 - 0.01$

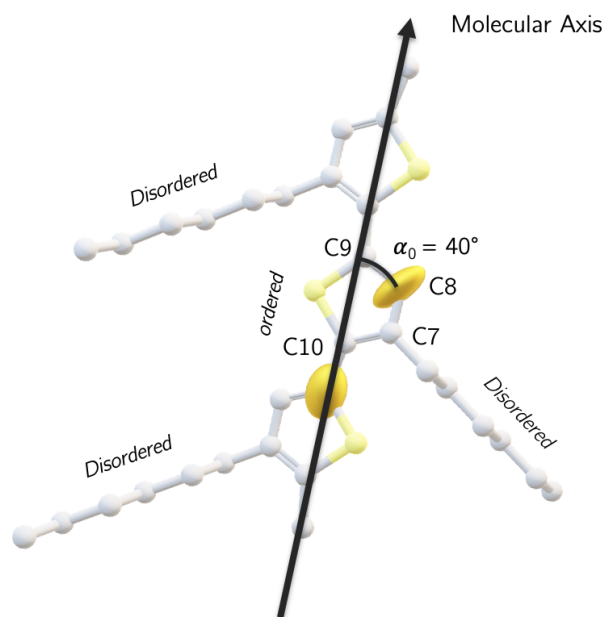


Figure 9.11: Representation the chemical shift anisotropy tensor in the molecular frame.

Qualitatively, the ROSMAS experiments reveal a highly ordered backbone while the side chain is largely disordered in Figure 9.13 and Figure 9.14. The α -carbon is somewhat oriented, while the C1 through C5 carbons only barely show effects of orientation. Information on the orientation of the side chains let us reevaluate previous assignments, with the new labeling in Figure 9.12.[95–99] Trends in a few of the ROSMAS experiments conducted within the work of this thesis have revealed additional information sourced to dynamic parts of the molecule. An ordered "rigid" polymer has its orientation side bands following the $I_{M,N} = I_{-M,N-M}$ symmetry of all absorption mode signals. Figure 9.14a reveals three non-phasable signals, corresponding to the C1-C3 carbons, at $N = 0$ for all M . The signals are attributed to molecular dynamics of the flexible side chain ends, though more work needs to be performed on the interpretation of these signals. The C1-C3 isotropic sidebands are also around 15 times smaller than what is predicted through Herzfeld-Berger analysis of a polyethylene model system. Which is attributed to molecular dynamics averaging of the CSA. The same effect is also found for the soft polystyrene adhesive

observed at 130.5 ppm in Figure 9.13b. A small amount of oriented signals from the C1 and C2 carbons, respectively, are observed. These signals have a stronger signal contributions in $M = \pm 2$ compared to $M = \pm 1$. This signal distribution occurs when the material is ordered 90° from the rotor direction. Consequentially, a small amount of the C1 and C2 carbons are therefore observed to align with the rotational forces in the rotor. The new features of dynamic origin add to a more complete understanding of polymeric systems.

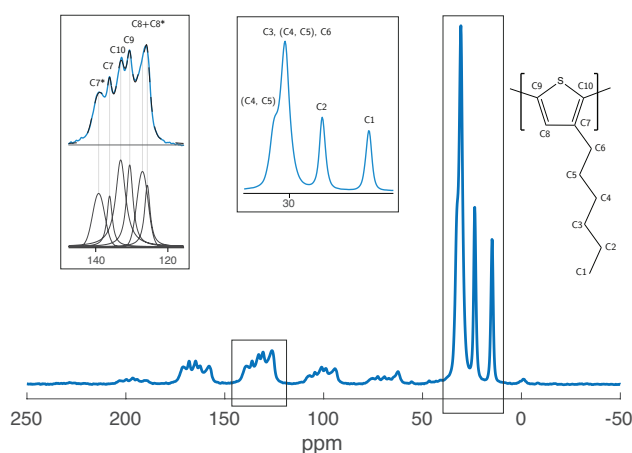


Figure 9.12: Solid-state NMR spectrum of cut poly(3-hexylthiophene) fibers at 4 kHz rotation rate. Insert shows the deconvolution scheme of the polymer signals.

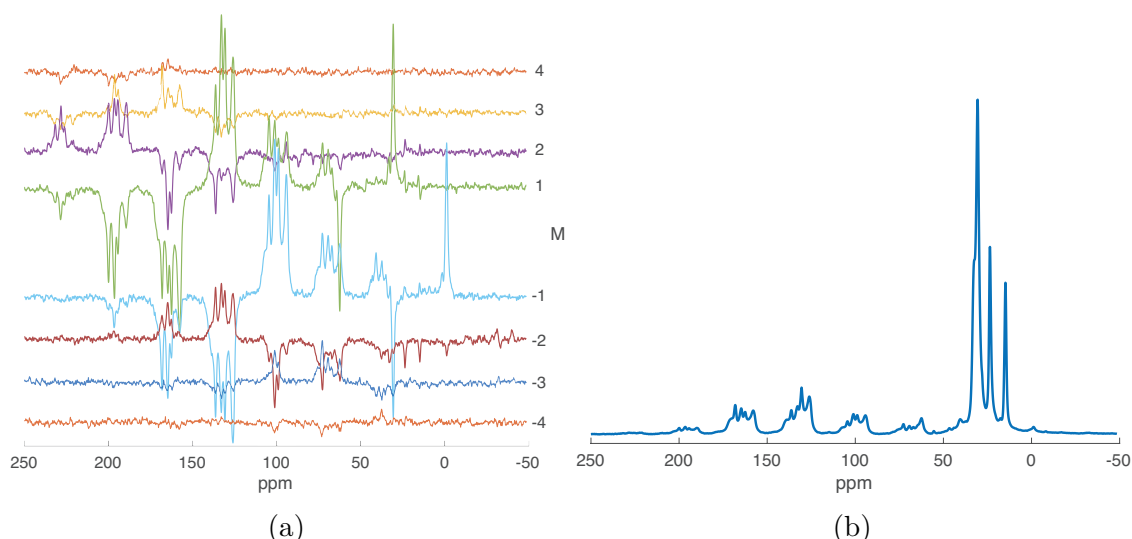


Figure 9.13: (a) Solid-state NMR ROSMAS 2D spectrum of oriented poly(3-hexylthiophene) fibers at 4 kHz rotation rate. The center $M = 0$ band is removed for visibility. (b) Solid-state NMR ROSMAS center $M = 0$ spectrum of oriented poly(3-hexylthiophene) fibers at 4 kHz rotation rate.

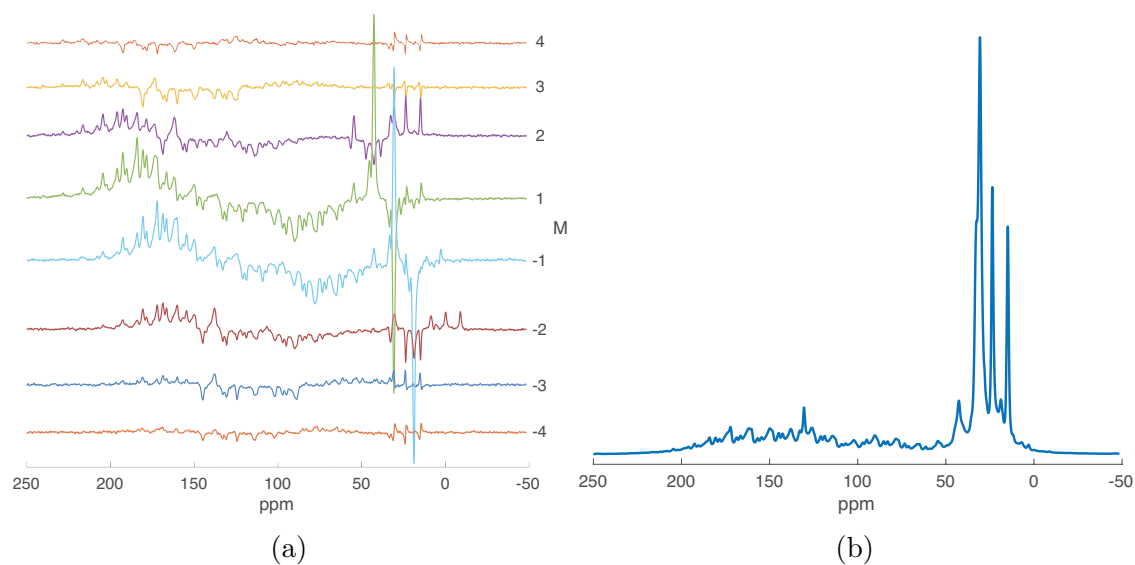


Figure 9.14: (a) Solid-state NMR ROSMAS 2D spectrum of oriented poly(3-hexylthiophene) fibers at 1.5 kHz rotation rate. The center $M = 0$ band is removed for visibility. (b) Solid-state NMR ROSMAS center $M = 0$ spectrum of oriented poly(3-hexylthiophene) fibers at 1.5 kHz rotation rate.

Chapter 10

Concluding Remarks

This work have established ROSMAS solid-state NMR as a quantitative technique by analyzing the trifecta of NMR spectroscopy, Raman spectroscopy and X-ray scattering. Analysis of orientation distributions on composites have long been a challenging task. This work demonstrates ROSMAS NMR spectroscopy as a powerful method to investigate cellulose composites, and composites in general. Although ROSMAS was first conceptualized before I was born, it is its application, or lack thereof, that ultimately determines its usefulness.

The three fundamentally different techniques have allowed us to scrutinize the evaluation of sensitive molecular orientation distribution X-ray scattering data by independently measuring Legendre polynomial order parameters from ROSMAS NMR. The choice of ODF found from X-ray patterns was implemented as a model for ROSMAS NMR spectroscopy and Raman spectroscopy, while retaining all quantitative aspects. As a consequence, the design of a significantly improved adaptation of the complete polarized Raman experiment was made.

ROSMAS was employed to investigate the molecular orientation of lignin-cellulose composite fibers. The technique effectively filtered out lignin signals, which had no significant orientation, while leaving the cellulose orientation signals in the $M \neq 0$ sidebands. Native wood was also studied where molecular orientation of the lignin was revealed. The oriented lignin in wood is not regained in the cellulose-lignin fiber. The lignin based carbon fiber industry have now gained a tool to investigate possible molecular orientation of various kinds of lignin, which may determine the best form of lignin for carbon fiber production.

The ROSMAS technique can be used to determine the chemical shift anisotropy, and its orientation in relation to the molecular frame, here in the case of poly(3-hexylthiophene) fibers. The study revealed a significant difference in molecular orientation between its "crystalline" and non-crystalline forms. The alkyl side chain display no orientation dependence at all, apart from minor orientation in the α -carbon. The tools are developed to study the anisotropic electrical conductivity of the doped polymers, of which molecular orientation is highly responsible.

Any technique imaginable is based on measuring a set of fundamental properties. Scattering of light through gratings, relative electron-nucleus vibrations or atomic spin resonances. These concepts inevitably have their own unique set of information. In harmony, these methods makes an orchestra. The audience is listening, eagerly interpreting its meaning.

Appendix A

Computational Remarks

A.1 Computation of the ROSMAS Intensity and Order Parameters

The methods used to calculate ROSMAS, Raman and WAXS information should be accessible with only an undergraduate knowledge in computational mathematics. But to ease the process of understanding the methods in code, and to possibly improve on them, I will go through a few of the crucial steps.

A time consuming step in the ROSMAS process is the calculation of the 5-dimensional integral of Equation (5.4). At integral dimensions higher than 3, it is beneficial to calculate the integral with a Monte Carlo solver. The solver calculates random elements in the 5-dimensional space and the average of these random elements is the sought integral. The downside is that the expected error has to scale with the random noise. The noise follows an SNR scaling of $1/\sqrt{n_{\text{MC}}}$ of the standard deviation, where n_{MC} is the number of Monte Carlo steps. The number of steps required to calculate the integral should be large enough to have the MC error be lower than the experimental error. Figure A.1 and A.2 shows a flow chart of the two ROSMAS methods used in paper **Paper I**.

The wL ROSMAS method differs computationally in one major way, compared to ROSMAS using the Legendre polynomials. The orientation determining factor γ in Equation (3.7) is not linearly separable from the integral like the Legendre polynomials would be. One can resort to iterative solutions methods at the cost of computational power, since each iteration has to solve the 5-dimensional MC integral. However, each step also has to have a MC error lower than $\Delta\gamma$. A homemade iterator dynamically changes the number of MC steps to not waste computational time.

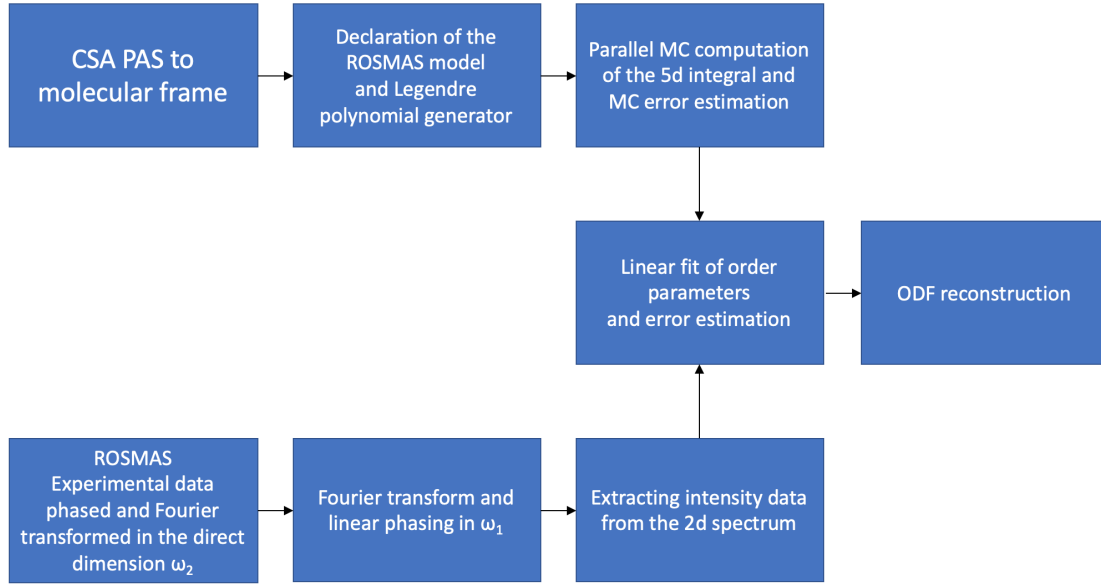


Figure A.1: Flowchart of data processing and computation of ROSMAS related equations

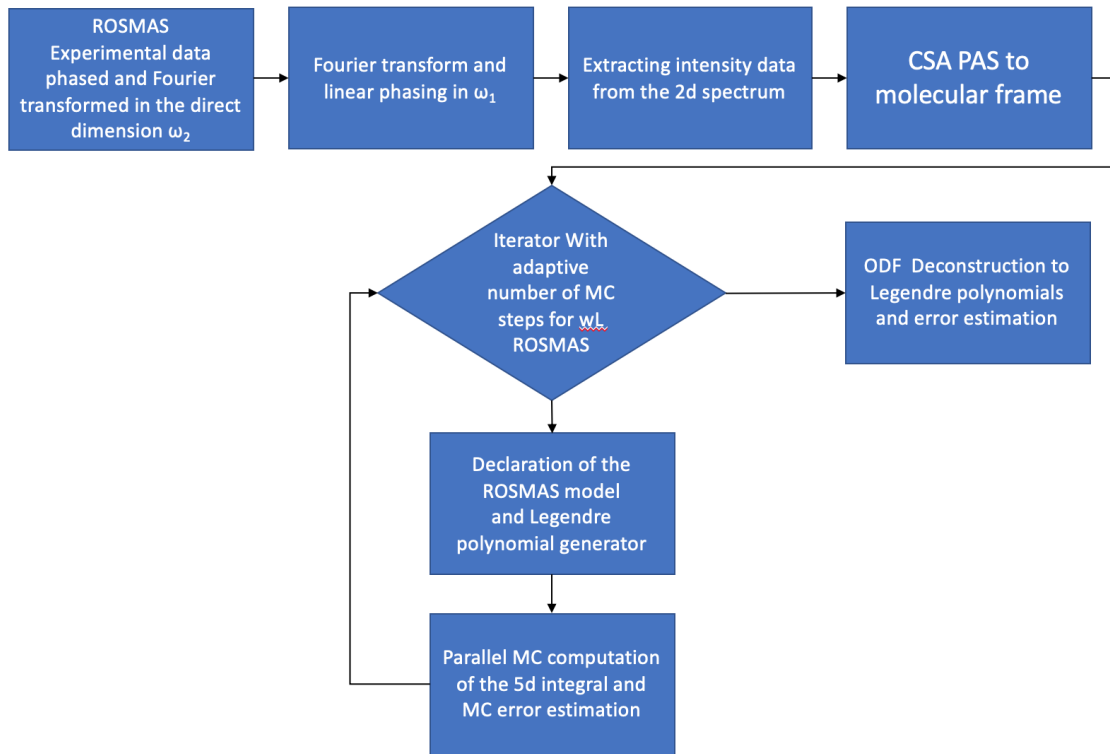


Figure A.2: Flowchart of data processing and computation of wL ROSMAS related equations

A.2 Computation of the Polarized Raman Experiment

The polarized Raman spectroscopy experiment is simply computed with an equation solver, in Matlab the appropriately named "solve" function is used. For the wL based experiment, two aspects are introduced. The first is the ODF dependent Euler angle θ , which does not have an analytical solution for the integration step in Equation (6.1). The second problem is the wL variable γ , which can not be separated from the rest of the equation. The four unknowns, γ and the PAS Raman tensor components a_1, a_2 and a_3 are solved through a square sum minimization scheme. While the other two Euler angles ψ and ϕ in Equation are solved analytically *a priori*, the set of equations from Equation (6.1) are integrated over θ during the minimization.

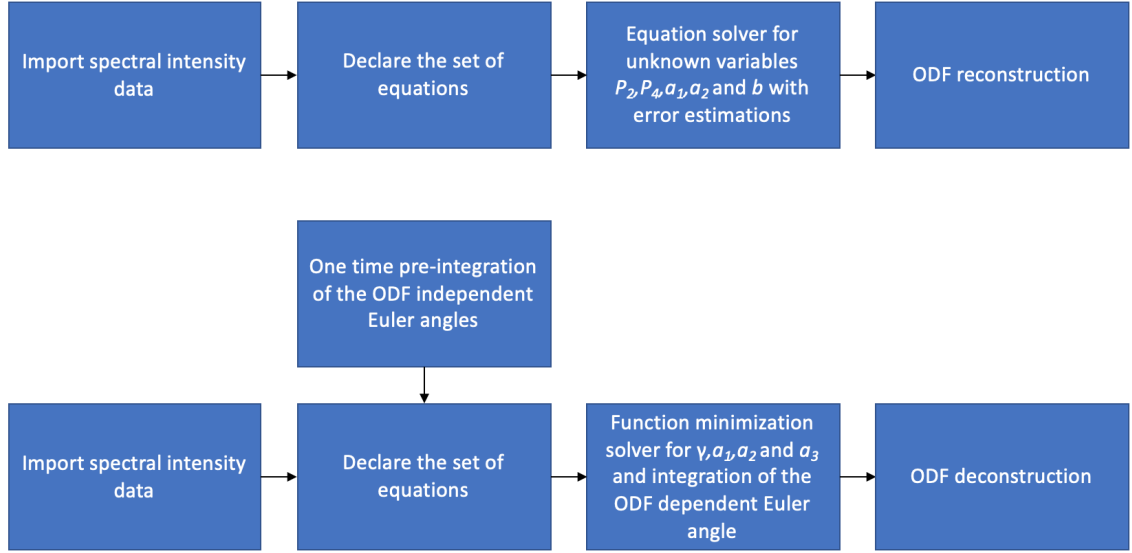


Figure A.3: Flowchart of the polarized Raman spectroscopy calculation (top) and the wrapped Lorentzian polarized Raman spectroscopy (bottom).

Appendix B

Derivation of Most Probable ODF

The information entropy, S , can be expressed as:

$$S = -k \int_0^\pi f(\theta) \ln(f(\theta)) \sin \theta \, d\theta \quad (\text{B.1})$$

with the uni-axial ODF as $f(\theta)$. The goal is to maximize S with the constraints that S has to fulfill the order parameter ODF relation with Equation (3.6). The solution is to add zero entropy with Lagrange multipliers and solving the problem with:

$$\frac{dS}{df(\theta)} = 0 \quad (\text{B.2})$$

$$\sum_\ell \lambda_\ell \left(\langle P_\ell \rangle - \int_0^\pi P_\ell(\cos \theta) f(\theta) \sin \theta \, d\theta \right) = 0 \quad (\text{B.3})$$

then:

$$S = -k \int_0^\pi f(\theta) \ln(f(\theta)) \sin \theta \, d\theta - \sum_\ell \lambda_\ell \left(\langle P_\ell \rangle - \int_0^\pi P_\ell(\cos \theta) f(\theta) \sin \theta \, d\theta \right) \quad (\text{B.4})$$

Setting λ_ℓ as $k \cdot \lambda_\ell$.

$$\frac{dS}{df(\theta)} = -k \int_0^\pi \left[1 + \ln(f(\theta)) - \sum_\ell \lambda_\ell P_\ell(\cos \theta) \right] \sin \theta \, d\theta = 0 \Rightarrow \quad (\text{B.5})$$

$$\left[1 + \ln(f(\theta)) - \sum_\ell \lambda_\ell P_\ell(\cos \theta) \right] = 0 \Rightarrow \quad (\text{B.6})$$

$$f(\theta) = \exp \left(-1 + \sum_\ell \lambda_\ell P_\ell(\cos \theta) \right) \quad (\text{B.7})$$

The final expression of the most probable ODF becomes:

$$f(\theta)_{\text{mp}} = A \cdot \exp\left(\sum_{\ell} \lambda_{\ell} P_{\ell}(\cos \theta)\right) \quad (\text{B.8})$$

where A is a normalization constant.

Appendix C

Links

ROSMAS matlab computation scripts:
github.com/LeoSvenningsson/ROSMAS

Polarized Raman spectroscopy matlab computation scripts:
github.com/LeoSvenningsson/Raman-ODF

Bibliography

- (1) Wolf, S. A.; Awschalom, D. D.; Buhrman, R. A.; Daughton, J. M.; von Molnár, S.; Roukes, M. L.; Chtchelkanova, A. Y.; Treger, D. M. *Science* **2001**, *294*, 1488–1495 (cit. on p. x).
- (2) *Magnetic Resonance Imaging: Physical Principles and Sequence Design*, second; Brown, R. W., Cheng, Y. N., Haacke, E. M., Thompson, M. R., Venkatesan, R., Eds.; John Wiley & Sons Ltd: 2014 (cit. on pp. x, 13).
- (3) *High-Resolution NMR Techniques in Organic Chemistry*, 2nd; Claridge, T. D. W., Ed.; Elsevier: Linacre House, Jordan Hill, Oxford OX2 8DP, UK, 2000 (cit. on p. x).
- (4) Mayer, M.; Meyer, B. *Angewandte Chemie International Edition* **1999**, *38*, 1784–1788 (cit. on p. x).
- (5) Mitchell, J.; Webber, J. B. W.; Strange, J. *Physics Reports* **2008**, *461*, 1–36 (cit. on p. x).
- (6) Petrov, O. V.; Furà, I. *Progress in Nuclear Magnetic Resonance Spectroscopy* **2009**, *54*, 97–122 (cit. on p. x).
- (7) Garcon, A. et al. *Quantum Science and Technology* **2017**, *3*, 014008 (cit. on p. x).
- (8) Garcon, A. et al. *Science Advances* **2019**, *5*, DOI: 10.1126/sciadv.aax4539 (cit. on p. x).
- (9) Odom, B.; Hanneke, D.; D’Urso, B.; Gabrielse, G. *Physical Review Letters* **2006**, *97*, 030801 (cit. on p. x).
- (10) Harbison, G. S.; Vogt, V.-D.; Spiess, H. W. *The Journal of Chemical Physics* **1986**, *86*, 1206–1218 (cit. on pp. 1, 7, 10, 12, 21, 24, 31, 36, 37).
- (11) Bower, D. I. *Journal of Polymer Science: Polymer Physics Edition* **1972**, *10*, 2135–2153 (cit. on pp. 1, 10, 11, 39, 41).
- (12) *Structure and Properties of Oriented Polymers*; Ward, I. M., Ed.; Springer-Science + Business Media, B.V.: 1997 (cit. on pp. 1, 10).
- (13) Chmelka, B. F.; Schmidt-Rohr, K.; Spiess, H. W. *Macromolecules* **1993**, *26*, 2282–2296 (cit. on pp. 1, 10, 21, 57).
- (14) Northolt, M.; Boerstoel, H.; Maatman, H.; Huisman, R.; Veurink, J.; Elzerman, H. *Polymer* **2001**, *42*, 8249–8264 (cit. on pp. 1, 10, 64).

-
- (15) Hongladarom, K.; Ugaz, V. M.; Cinader, D. K.; Burghardt, W. R.; Quintana, J. P.; Hsiao, B. S.; Dadmun, M. D.; Hamilton, W. A.; Butler, P. D. *Macromolecules* **1996**, *29*, 5346–5355 (cit. on pp. 1, 10).
- (16) Lafrance, C.-P.; Pézolet, M.; Prud'homme, R. E. *Macromolecules* **1991**, *24*, 4948–4956 (cit. on pp. 1, 5, 10).
- (17) Svenningsson, L.; Lin, Y.-C.; Karlsson, M.; Martinelli, A.; Nordstierna, L. *Macromolecules* **2019**, *52*, 3918–3924 (cit. on pp. 1, 56).
- (18) Svenningsson, L.; Sparrman, T.; Bialik, E.; Bernin, D.; Nordstierna, L. *Cellulose* **2019**, *26*, 4681–4692 (cit. on pp. 1, 4).
- (19) *Cellulose: structure, accessibility, and reactivity*, 1st ed.; Krässig, H. A., Ed.; Gordon and Breach Science Publishers: 1400 Yverdon, Switzerland, 1993 (cit. on pp. 3, 5, 47, 52).
- (20) *Nanocellulose, From Nature to High Performance Tailored Materials*, 2nd ed.; Dufresne, A., Ed.; Walter de Gruyter GmbH, Berlin/Boston, 2018: Germany, 2018 (cit. on pp. 3, 5, 52).
- (21) Credou, J.; Berthelot, T. *Journal of Materials Chemistry B* **2014**, *2*, 4767–4788 (cit. on pp. 3, 5).
- (22) Reyes, D. C. A.; Skoglund, N.; Svedberg, A.; Eliasson, B.; Sundman, O. *Cellulose* **2016**, *23*, 1061–1072 (cit. on p. 3).
- (23) Langan, P.; Nishiyama, Y.; Chanzy, H. *Biomacromolecules* **2001**, *2*, 410–416 (cit. on p. 4).
- (24) Langan, P.; Sukumar, N.; Nishiyama, Y.; Chanzy, H. *Cellulose* **2005**, *12*, 551–562 (cit. on p. 4).
- (25) Chen, P.; Ogawa, Y.; Nishiyama, Y.; Bergensträhle-Wohlert, M.; Mazeau, K. *Cellulose* **2015**, *22*, 1485–1493 (cit. on p. 4).
- (26) Eco label., <http://ec.europa.eu/ecat/product/en/37/textile-products-tencel-wei-#>, Accessed: 2018-08-08 (cit. on p. 4).
- (27) Lyocell market., <https://www.gminsights.com/industry-analysis/lyocell-fiber-market>, Accessed: 2018-08-02 (cit. on p. 5).
- (28) Sixta, H.; Michud, A.; Hauru, L.; Shirin Asaadi, Y. M.; King, A. W.; Kilpeläinen, I.; Hummel, M. *Nordic Pulp and Paper Research Journal* **2015**, *30*, 43–57 (cit. on pp. 5, 52).
- (29) Sun, L.; Chen, J. Y.; Jiang, W.; Lynch, V. *Carbohydrate Polymers* **2015**, *118*, 150–155 (cit. on pp. 5, 10).
- (30) Wanasekara, N. D.; Michud, A.; Zhu, C.; Rahatekar, S.; Sixta, H.; Eichhorn, S. J. *Polymer* **2016**, *99*, 222–230 (cit. on pp. 5, 48, 56).
- (31) *Regenerated cellulose fibres*; Woodings, C., Ed.; Woodhead Publishing Ltd, 2001: Abington Hall, Abington Cambridge CB1 6AH England, 2001 (cit. on p. 5).

- (32) Klemm, D.; Heublein, B.; Fink, H.-P.; Bohn, A. *Angewandte Chemie International Edition* **2005**, *44*, 3358–3393 (cit. on pp. 5, 52).
- (33) Park, S.; Baker, J. O.; Himmel, M. E.; Parilla, P. A.; Johnson, D. K. *Biotechnology for Biofuels* **2010**, *3*, DOI: 10.1186/1754-6834-3-10 (cit. on pp. 5, 51, 52, 60).
- (34) Kosan, B.; Michels, C.; Meister, F. *Cellulose* **2008**, *15*, 59–66 (cit. on p. 5).
- (35) Frank, E.; Steudle, L. M.; Ingildeev, D.; Spörl, J. M.; Buchmeiser, M. R. *Angewandte Chemie International Edition* **2014**, *53*, 5262–5298 (cit. on p. 5).
- (36) Mainka, H.; Täger, O.; Körner, E.; Hilfert, L.; Busse, S.; Edelmann, F. T.; Herrmann, A. S. *Journal of Materials Research and Technology* **2015**, *4*, 283–296 (cit. on p. 5).
- (37) *Carbon Fibers*, 2nd ed.; Park, S.-J., Ed.; Springer: Springer Nature Singapore Pte Ltd. 2018, 2015 (cit. on p. 5).
- (38) Byrne, N.; De Silva, R.; Ma, Y.; Sixta, H.; Hummel, M. *Cellulose* **2018**, *25*, 723–733 (cit. on p. 5).
- (39) Ma, Y. et al. *ChemSusChem* **2015**, *8*, 4030–4039 (cit. on p. 5).
- (40) Bengtsson, A.; Bengtsson, J.; Olsson, C.; Sedin, M.; Jedvert, K.; Theliander, H.; Sjöholm, E. *Holzforschung* **2018**, *72*, 1007–1016 (cit. on pp. 5, 62).
- (41) Bengtsson, A.; Bengtsson, J.; Sedin, M.; Sjöholm, E. *ACS Sustainable Chemistry & Engineering* **2019**, *7*, 8440–8448 (cit. on p. 5).
- (42) Das, S. *The International Journal of Life Cycle Assessment* **2011**, *16*, 268–282 (cit. on p. 5).
- (43) *Directional Statistics*; Marida, K. V., Jupp, P. E., Eds.; John Wiley & Sons Ltd: Baffins Lane, Chichester, West Sussex, PO19 1UD England, 2000 (cit. on pp. 7, 11, 12).
- (44) Hamilton, W. R. *Philosophical Magazine* **1844** (cit. on p. 7).
- (45) Harbison, G. S.; Spiess, H. W. *Chemical physics letters* **1985**, *124*, 128–134 (cit. on pp. 10, 21).
- (46) Henrichs, P. M. *Macromolecules* **1987**, *20*, 2099–2112 (cit. on pp. 10, 21).
- (47) Geen, C. C. N. H.; Titman, J. J. *Solid State Nuclear Magnetic Resonance* **2002**, *22*, 298–310 (cit. on pp. 10, 21).
- (48) Titman, J. J.; de Lacroix, S. F.; Spiess, H. W. *The Journal of Chemical Physics* **1993**, *98*, 3816–3826 (cit. on pp. 10, 21, 36).
- (49) Schreiber, R.; Veeman, W. S.; Gabriëlse, W.; Arnauts, J. *Macromolecules* **1999**, *32*, 4647–4657 (cit. on pp. 10, 21, 31).
- (50) Gabriëlse, W.; Gaur, H. A.; Veeman, W. S. *Macromolecules* **1996**, *29*, 4125–4133 (cit. on pp. 10, 21, 22, 31).
- (51) Gabriëlse, W.; van Well, H.; Veeman, W. S. *Solid State Nuclear Magnetic Resonance* **1995**, *6*, 231–240 (cit. on pp. 10, 21, 22, 31).

- (52) Wilhelm, M.; de Lacroix, S. F.; Titman, J.; Schmidt-Rohr, K.; Spies, H. *Acta Polymer* **1993**, *44*, 279–284 (cit. on pp. 10, 21).
- (53) Song, Z.; Antzutkin, O. N.; Lee, Y. K.; Shekar, S. C.; Rupprecht, A.; Levitt, M. H. *Biophysical Journal* **1997**, *73*, 1539–1552 (cit. on pp. 10, 21).
- (54) Tzou, D. L.; Desai, P.; Abhiraman, A. S.; Huang, T.-H. *Journal of Polymer Science: Part B: Polymer Physics* **1995**, *33*, 63–69 (cit. on pp. 10, 21).
- (55) Schmidt-Rohr, K.; Hehn, M.; Schaefer, D.; Spiess, H. W. *The Journal of Chemical Physics* **1992**, *97*, 2247–2262 (cit. on pp. 10, 21).
- (56) Kropewnicki, M. L.; Schaefer, D. J.; Hehn, M.; Dermaut, W.; Geise, H. J.; Chmelka, B. F. *Solid State Nuclear Magnetic Resonance* **2002**, *22*, 275–297 (cit. on pp. 10, 21).
- (57) Purvis, J.; Bower, D. I. *Society for Applied Spectroscopy* **2004**, *58*, 279–286 (cit. on p. 10).
- (58) Bower, D. I. *Journal of Polymer Science: Polymer Physics Edition* **1981**, *19*, 93–107 (cit. on pp. 10, 11, 45, 58).
- (59) Citra, M. J.; Chase, D. B.; Ikeda, R. M.; Gardner, K. H. *Macromolecules* **1995**, *28*, 4007–4012 (cit. on pp. 10, 39, 43, 45).
- (60) Yang, S.; Michielsen, S. *Macromolecules* **2002**, *35*, 10108–10113 (cit. on pp. 10, 39, 44, 45).
- (61) Yang, S.; Michielsen, S. *Macromolecules* **2003**, *36*, 6484–6492 (cit. on pp. 10, 39, 58).
- (62) Yang, S. *PhD. Thesis, Georgia Institute of Technology* **2002** (cit. on p. 10).
- (63) Richard-Lacroix, M.; Pellerin, C. *Macromolecules* **2013**, *46*, 5561–5569 (cit. on pp. 10, 39, 57).
- (64) Frisk, S.; Ikeda, R. M.; Chase, D. B.; Rabolt, J. F. *Society for Applied Spectroscopy* **2004**, *58*, 279–286 (cit. on pp. 10, 39).
- (65) J. J. Hermans P. H. Hermans, D. V.; Weidinger, A. *Recueil des Travaux Chimiques des Pays-Bas* **1946**, *24*, 427–447 (cit. on p. 10).
- (66) Frueh, D. P.; Goodrich, A. C.; Mishra, S. H.; Nichols, S. R. *Current Opinion in Structural Biology* **2013**, *23*, Protein-carbohydrate interactions / Biophysical methods, 734–739 (cit. on p. 13).
- (67) *Understanding NMR Spectroscopy*, 2nd ed.; Keeler, J., Ed.; John Wiley & Sons, Ltd: The Atrium, Southern Gate, Chichester, West Sussex, PO19 8SQ, United Kingdom, 2010 (cit. on p. 16).
- (68) *Introduction to Solid-State NMR Spectroscopy*, 1st ed.; Duer, M. J., Ed.; Blackwell Publishing Ltd: 9600 Garsington Road, Oxford OX4 2DQ, UK, 2004 (cit. on pp. 16, 21).
- (69) *Spin Dynamics—Basics of Nuclear Magnetic Resonance, Second Edition*, 2nd ed.; Levitt, M. H., Ed.; John Wiley & Sons Ltd: The Atrium, Southern Gate Chichester, West Sussex PO19 8SQ, England, 2008 (cit. on p. 16).

- (70) McBrierty, V. J.; McDonald, I. R.; Ward, I. M. *Journal of Physics D: Applied Physics* **1971**, *4*, 88–101 (cit. on p. 21).
- (71) Wang, T.; Salazar, A.; Zabolina, O. A.; Hong, M. *Biochemistry* **2014**, *53*, 2840–2854 (cit. on p. 21).
- (72) Tzou, D. L.; Spiess, H. W.; Curran, S. *Journal of Polymer Science Part B: Polymer Physics* **1994**, *32*, 1521–1529 (cit. on pp. 21, 22).
- (73) Tzou, D.; Schmidt-Rohr, K.; Spiess, H. *Polymer* **1994**, *35*, 4728–4733 (cit. on pp. 21, 22).
- (74) Herzfeld, J.; Berger, A. E. *The Journal of Chemical Physics* **1980**, *73*, 6021–6030 (cit. on pp. 28, 29, 31).
- (75) Mueller, L. J. *Concepts in Magnetic Resonance Part A* **2011**, *38A*, 221–235 (cit. on p. 30).
- (76) M. J. Frisch and G. W. Trucks and H. B. Schlegel and G. E. Scuseria and M. A. Robb and J. R. Cheeseman and G. Scalmani and V. Barone and G. A. Petersson and H. Nakatsuji and X. Li and M. Caricato and A. Marenich and J. Bloino and B. G. Janesko and R. Gomperts and B. Mennucci and H. P. Hratchian and J. V. Ortiz and A. F. Izmaylov and J. L. Sonnenberg and D. Williams-Young and F. Ding and F. Lipparini and F. Egidi and J. Goings and B. Peng and A. Petrone and T. Henderson and D. Ranasinghe and V. G. Zakrzewski and J. Gao and N. Rega and G. Zheng and W. Liang and M. Hada and M. Ehara and K. Toyota and R. Fukuda and J. Hasegawa and M. Ishida and T. Nakajima and Y. Honda and O. Kitao and H. Nakai and T. Vreven and K. Throssell and J. A. Montgomery and Jr. and J. E. Peralta and F. Ogliaro and M. Bearpark and J. J. Heyd and E. Brothers and K. N. Kudin and V. N. Staroverov and T. Keith and R. Kobayashi and J. Normand and K. Raghavachari and A. Rendell and J. C. Burant and S. S. Iyengar and J. Tomasi and M. Cossi and J. M. Millam and M. Klene and C. Adamo and R. Cammi and J. W. Ochterski and R. L. Martin and K. Morokuma and O. Farkas and J. B. Foresman and and D. J. Fox Gaussian 09, Revision B.01., Gaussian, Inc., Wallingford CT, 2016, 2016 (cit. on p. 31).
- (77) Hentschel, R.; Schlitter, J.; Sillescu, H.; Spiess, H. W. *The Journal of Chemical Physics* **1978**, *68*, 56–66 (cit. on p. 36).
- (78) *Infrared and Raman spectroscopy, Principles and Spectral Interpretation*; Larkin, P. J., Ed.; Elsevier: 225 Wyman Street, MA 02451, USA, 2011 (cit. on p. 39).
- (79) Tanaka, M.; Young, R. J. *Journal of Materials Science* **2006**, *41*, 963–991 (cit. on p. 39).
- (80) Tsuboi, M.; Benevides, J. M.; George J. Thomas, J. *Proceedings of the Japan Academy, Ser. B* **2009**, *85*, 83–97 (cit. on p. 44).
- (81) Labarthet, F. L.; Buffeteau, T.; Sourisseau, C. *Society for Applied Spectroscopy* **2000**, *54*, 699–705 (cit. on p. 45).

- (82) Schenzel, K.; Fischer, S. *Cellulose* **2000**, *8*, 49–57 (cit. on pp. 45, 56).
- (83) Nobel Prize 1962., https://www.nobelprize.org/nobel_prizes/medicine/laureates/1962/speedread.html, Accessed: 2018-08-02 (cit. on p. 47).
- (84) Kolpak, F. J.; Blackwell, J. *Macromolecules* **1975**, *9*, 273–278 (cit. on p. 47).
- (85) Larsson, P. T.; Hult, E.-L.; Wickholm, K.; Pettersson, E.; Iversen, T. *Solid State Nuclear Magnetic Resonance* **1999**, *15*, 31–40 (cit. on pp. 51, 52).
- (86) Park, S.; Johnson, D. K.; Ishizawa, C. I.; Parilla, P. A.; Davis, M. F. *Cellulose* **2009**, *16*, 641–647 (cit. on pp. 51, 52, 60).
- (87) Schenzel, K.; Fischer, S.; Brendler, E. *Cellulose* **2005**, *12*, 223–231 (cit. on p. 51).
- (88) Ahvenainen, P.; Kontro, I.; Svedström, K. *Cellulose* **2016**, *23*, 1073–1086 (cit. on pp. 51, 52).
- (89) Earl, W. L.; VanderHart, D. L. *Macromolecules* **1979**, *12*, 762–767 (cit. on p. 51).
- (90) Klemm, D.; Heublein, B.; Fink, H.-P.; Bohn, A. *Angewandte Chemie International Edition* **2011**, *50*, 5438–5466 (cit. on p. 52).
- (91) Idström, A.; Schantz, S.; Sundberg, J.; Chmelka, B. F.; Gatenholm, P.; Nordstierna, L. *Carbohydrate Polymers* **2016**, *151*, 480–487 (cit. on pp. 52, 55).
- (92) Kim, J.-W.; Park, S.; Harper, D. P.; Rials, T. G. *Journal of Applied Polymer Science* **2013**, DOI: 10.1002/app.38149 (cit. on p. 52).
- (93) Atalla, R. H.; Agarwal, U. P. *Science* **1985**, *227*, 636–638 (cit. on p. 62).
- (94) Kang, X.; Kirui, A.; Widanage, M. C. D.; Mentink-Vigier, F.; Cosgrove, D. J.; Wang, T. *Nature Communications* **2019**, *10*, 347 (cit. on p. 62).
- (95) Nieuwendaal, R. C.; Snyder, C. R.; DeLongchamp, D. M. *ACS Macro Letters* **2014**, *3*, 130–135 (cit. on p. 66).
- (96) Martini, F.; Borsacchi, S.; Spera, S.; Carbonera, C.; Cominetti, A.; Geppi, M. *The Journal of Physical Chemistry C* **2013**, *117*, 131–139 (cit. on p. 66).
- (97) Yazawa, K.; Inoue, Y.; Shimizu, T.; Tansho, M.; Asakawa, N. *The Journal of Physical Chemistry B* **2010**, *114*, PMID: 20050621, 1241–1248 (cit. on p. 66).
- (98) Snyder, C. R.; Nieuwendaal, R. C.; DeLongchamp, D. M.; Luscombe, C. K.; Sista, P.; Boyd, S. D. *Macromolecules* **2014**, *47*, 3942–3950 (cit. on p. 66).
- (99) Shen, X.; Hu, W.; Russell, T. P. *Macromolecules* **2016**, *49*, 4501–4509 (cit. on p. 66).